12-2011

Axisymmetric Finite Element Modeling of Adhesive Joint Between a Laminated Composite and Metal Cylinder

Casey A. Talbot
Utah State University

AXISYMMETRIC FINITE ELEMENT MODELING OF ADHESIVE JOINT BETWEEN A LAMINATED COMPOSITE AND METAL CYLINDER

by

Casey A. Talbot

A thesis submitted in partial fulfillment
of the requirements for the degree

of

MASTER OF SCIENCE

in

Mechanical Engineering

Approved:

_____	_____
Thomas Fronk Major Professor	Steven Folkman Committee Member
_____	_____
Barton Smith Committee Member	Mark R. McLellan Vice President for Research and Dean of the School of Graduate Studies

UTAH STATE UNIVERSITY
Logan, Utah

2011

ABSTRACT

Axisymmetric Finite Element Modeling of Adhesive Joint Between a Laminated Composite and Metal Cylinder

by

Casey A. Talbot, Master of Science

Utah State University, 2011

Major Professor: Dr. Thomas H. Fronk
Department: Mechanical and Aerospace Engineering

In order to incorporate fiber-reinforced composite materials in space structures, adhesive joining techniques are required. Because analytical models have a hard time capturing the complex stress state inherent to adhesively joining dissimilar materials, a different modeling technique was deemed necessary. A two-dimensional axisymmetric finite element model capable of capturing the three-dimensional stress state of cylindrical adhesive joints was developed. In order to rigorously validate the model, testing was undergone to ensure the model accurately predicted joint displacements.

Displacement data was acquired via an Epsilon axial extensometer. Load data was taken simultaneously via the load cell incorporated in the Tinius Olsen tensile test machine used. The measured force vs. displacement data was found to agree with the model's predicted displacement for a given load. Displacement data was also taken, again with the extensometer, as the joints were rapidly cooled to liquid nitrogen temperature. It was found that the joints behave much like laminated plates in that after the first several cycles they "settle down". The term "settle down", in this context, means that after the first several cycles the displacements of the joints when placed from a room temperature environment to a cryogenic environment become consistent and

smooth. This result allows for the joints to be modeled. The finite element model was shown to accurately predict the settled down displacement given the prescribed temperature change.

The joints were also shown to maintain structural integrity post thermal cycling. Transient temperature tensile tests were performed until sample failure. One result with major design implication coming from this test was that the material properties do not change significantly enough over the temperature range tested to affect the joint's behavior. The same properties used in the room temperature model were used to model the measured data of the transient temperature data and were found to match satisfactorily.

Having validated that the developed axisymmetric finite element model accurately predicts cylindrical joint displacement fields, the model becomes an invaluable tool in design. The model can now be used in confidence, in conjunction with design requirements for a specific joint, to reduce the maximum displacements below any specified operating requirements.

(127 pages)

PUBLIC ABSTRACT

Because lowering weight as much as possible is desirable in all applications designed to go to space, the use of composite materials is desirable. Composites are materials that are made up of two or more separate materials usually with significantly different characteristics which remain separate and distinct in their completed state. Fiber-reinforced epoxy composites, in general, are very strong and light. Because most space structures cannot solely be made of composites, a method to join them with metals is needed. Adhesive joining, or gluing, has been determined to be the most promising option.

For the joining technique to be used, engineers must be able to predict how the joined materials will behave when placed under load and/or temperature change. A widely used modeling technique used today is finite element analysis. Finite element analysis is a modeling method that can be run on computers to predict the displacement of specified points of the part or structure being modeled.

In order for the model to be trusted, physical measurements were taken and compared to the models predictions. The model was found to agree with the measured data under both traditional force loading and when the joined materials underwent a temperature change. This result allows the model to be used with confidence by engineers to build space structures.

ACKNOWLEDGMENTS

I would like to thank Dr. Thomas Fronk along with Space Dynamics Lab (SDL) for the opportunity to perform this research. This thesis would not have been possible without all of the teaching I have received to understand the engineering concepts and theories used within this research. I would also like to thank my fellow graduate students for their availability in talking through issues as they came up.

Special thanks to SDL for funding this research. I am hopeful that the contents of this thesis will be useful in moving forward in the design and implementation of cylindrical composites in their space structures. I would like to express special thanks to Dr. Barton Smith for extensive help with the instrumentation used in this research. Special thanks also to Dr. Steven Folkman for his guidance in both the finite element model development and verification as well as in instrument calibration. A thank you is also extended for the willingness to serve on my committee.

I would especially like to thank my family and friends for all of the support throughout the entire schooling process. Special thanks to my mom and dad for listening to all of the frustrations experienced along the way.

Casey A. Talbot

CONTENTS

Page

ABSTRACT iii

PUBLIC ABSTRACT v

ACKNOWLEDGMENTS vi

LIST OF TABLES x

LIST OF FIGURES xi

CHAPTER

1. INTRODUCTION 1

2. LITERATURE REVIEW 3

2.1 Introduction 3
2.2 Thermal Cycling 3
2.3 Models 6
2.4 Testing Methods 9
2.5 Conclusions and Final Thoughts 11

3. OBJECTIVES 13

4. FINITE ELEMENT METHOD DEVELOPMENT 14

4.1 Variational Derivation of 3D Equilibrium Equations 14
4.2 Axisymmetric Model Reduction 25
4.3 Axisymmetric Finite Element Model 26
4.4 Finite Element Program 31

4.4.1 Finite Element Program Capabilities 32
4.4.2 FORTRAN Meshing Programs 34
4.4.3 FORTRAN Finite Element Solver 36
4.4.4 Visual Basic GUI 37

4.5 Conclusions 41

5. MATERIAL AND EQUIPMENT SELECTION 42

5.1 Unidirectional Carbon Fiber 42

5.1.1 Composite Selection 42
5.1.2 Initial Material Property Estimates 42

5.2 Aluminum 43
5.3 Epoxies for Use at Cryogenic Temperatures 43

5.3.1 Ductility and Strength Considerations 44
5.3.2 Initial Thermal Shock Consideration 44
5.3.3 Out-gassing Consideration 44
5.3.4 Case Study of Commercially Available Adhesives 45
5.3.5 Final Selection and Material Properties 45

5.4 Extensometer 47
5.5 Analog Input Device 48

6. DATA ACQUISITION CONFIGURATION AND VERIFICATION 50

6.1 Extensometer and Load Data Acquisition System Introduction 50
6.2 Instrumentation Amplifier 52
6.3 Data Acquisition Software 55
6.4 Extensometer Calibration Procedure and Associated Uncertainty 56
6.5 Load Cell Calibration Procedure and Associated Uncertainty 59
6.6 Data Acquisition Setup Verification 60

7. SAMPLE PREPERATION 66

7.1 Aluminum Preparation 66
7.2 Composite Sleeve Manufacture 67
7.3 3M 2216 Gray Preparation 68
7.4 Joint Sample Assembly and Cleanup 68
7.5 Resulting Joint Geometry 70

8. JOINT STIFFNESS TESTING AT ROOM TEMPERATURE 72

8.1 Experimental Setup 72
8.2 Test Results 73

8.2.1 Test Repeatability 73
8.2.2 Room Temperature Measured Results Compared With FEA 75

9. JOINT RESPONSE TO CRYOGENIC ENVIRONMENT 80

9.1 Experimental Setup 80
9.2 CTE Estimates 82
9.3 Test Results 84

9.3.1 Joint Settling 85
9.3.2 Measure Results Compared with FEA 85

10. JOINT STIFFNESS TESTING AT LIQUID NITROGEN TEMPERATURE 91

10.1 Experimental Setup 91
10.2 Test Results 92

10.2.1 Joint Strength 93
10.2.2 Transient Temperature Measured Results Compared with FEA 99

11. CONCLUSIONS 104

11.1 Conclusions Drawn from Room Temperature Tensile Testing 104
11.2 Conclusions Drawn from Cryogenic Temperature Cycling 106
11.3 Conclusions Drawn from Transient Temperature Tensile Testing 107
11.4 Recommendations for Future Work 108

REFERENCES 109

APPENDIX 112

LIST OF TABLES

Table Page

1. Adhesive Case Study 46

2. Material Properties for 3M Scotchweld 2216 B/A Gray 47

3. Resulting Sample Geometry Measurements and Number of Elements Used 71

4. Room Temperature Material Properties 75

5. CTE Estimates 84

6. Sample Failure Modes and Total Test Times 94

LIST OF FIGURES

Figure Page

1. A typical cylindrical adhesive joint 14

2. General configurations the code can model along with dimension labels seen in the GUI Typical adhesive joint (Top), Adhesive insert joint (Bottom 34

3. Mesh Generator v-2 front panel 38

4. Mesh Generator v-2 Material Property Input popup window 39

5. Mesh Generator v-2 Edge boundary condition input 39

6. Generator v-2 Left: single point constraint and Right: point load input 40

7. Mesh Generator v-2 Composite Stacking Sequence Optimization input 40

8. NI USB-6210 multifunctional I/O device 50

9. Epsilon 3542-025M-010-LT Extensometer 51

10. Tinius Olsen 50KN (11240lbf) load cell 51

11. Instrumentation Amplifier 52

12. Instrumentation Amplifier Schematic hooked up to NI USB-6210 55

13. Schaevitz calibration stand 57

14. Axial extensometer with zero pin circled 58

15. Calibration data for three separate runs 59

16. Extensometer placement on sample, Left: front; Middle: side; Right: back 61

17. Force vs. Displacement results when changing the placement of the extensometer on the reference sample 61

18. Tensile grips side views, Left: Original reference specimen placement in tensile grips Right: Final placement with spacers 62

19. Load frame alignment, Left: Front view Right: Side view 63

20. Side view of the tensile grips originally 63

21. Side view of grip alignment after straightening 64

22. Force vs. Displacement results when changing the placement of the extensometer on the reference sample after spacing and straightening 65

23. Palm sander used to obtain a consistent abrasion pattern 66

24. Prepared samples being hung to allow removal of excess etchant as well as to avoid contamination due to contact with unclean surfaces 67

25. Layout of angle ply prepreg to be wound on mandrel 68

26. Joint samples directly after being removed from oven 69

27. Excess resin removed from the composite and allowed to escape through the perforated heat shrink tape 70

28. The completed joint samples 70

29. Room temperature test setup 73

30. repeatability results for the three composite layups 74

31. Room temperature force vs. displacement plots for the 15° samples along with FEA results 76

32. Deformed finite element u-displacements results for 15° composite layup with a 13345N (3000lbf) load 76

33. Room temperature force vs. displacement plots for the 45° samples along with FEA results 77

34. Deformed finite element u-displacements results for 45° composite layup with a 13345N (3000lbf) load 77

35. Room temperature force vs. displacement plots for the 60° samples along with FEA results 78

36. Deformed finite element u-displacements results for 60° composite layup with a 13345N (3000lbf) load 78

37. Validation of finite element analysis to predict joint displacement at room temperature 79

38. Cryogenic temperature test setup 81

39. Cryogenic temperature test setup with liquid nitrogen bath 81

40. Aluminum sample displacement response when placed in liquid nitrogen bath 83

41. Unidirectional composite tube displacement response when placed in liquid nitrogen bath 83

42. Sample cycling results showing joints settling at about the 5^{th} cycle 86

43. Measured displacement data of joints when submerged in liquid nitrogen bath. FEA result when joint reaches equilibrium at liquid nitrogen temperature. Data for Sample 2 was especially noisy and was thrown away 87

44. Deformed finite element u-displacements results for 15° composite layup with a -217°C (-390°F) temperature load 88

45. Measured displacement data of joints when submerged in liquid nitrogen bath. FEA result when joint reaches equilibrium at liquid nitrogen temperature 88

46. Deformed finite element u-displacements results for 45° composite layup with a -217°C (-390°F) temperature load 89

47. Measured displacement data of joints when submerged in liquid nitrogen bath. FEA result when joint reaches equilibrium at liquid nitrogen temperature 89

48. Deformed finite element u-displacements results for 60° composite layup with a -217°C (-390°F) temperature load 90

49. Transient temperature test setup 92

50. The load at which each of the joint samples failed after 5 thermal cycles 93

51. 15° Sample 1 adhesive layer brittle type failure 95

52. 15° Sample 2 aluminum began to yield before joint failure 95

53. 15° Sample 3 aluminum began to yield before joint failure 96

54. 45° Sample 1 interlaminar composite brittle type failure 96

55. 45° Sample 2 interlaminar composite brittle type failure 97

56. 45° Sample 3 mixed interlaminar composite/adhesive brittle type failure 97

57. 60° Sample 1 broke in the center due to not being kept perfectly straight during cure 98

58. 60° Sample 2 mixed interlaminar composite/adhesive brittle type failure 98

59. 60° Sample 3 interlaminar composite brittle type failure 99

60. Omega thermometer used to measure temperature at 10 second intervals during test 100

61. Placement of the thermocouple on the joint sample (placement is right at the center of the composite sleeve 100

62. Temperature response of center of joint to test configuration 101

63. Transient temperature force vs. displacement plots for the 15° samples along with FEA results 102

64. Transient temperature force vs. displacement plots for the 45° samples along with FEA Result 102

65. Transient temperature force vs. displacement plots for the 60° samples along with FEA results 103

66. Misalignment study results 105

67. Element aspect ratios 113

68. Element aspect ratios zoomed in to show mesh 113

CHAPTER 1

INTRODUCTION

Joining laminated composite materials and metals is problematic. Mechanical fasterners do not work well will composite materials. Tradionally the joint involves some form of an adhesive. For the preliminary design of cylindrical adhesive joints, axisymmetric finite element models have been developed. In the thesis submitted by Paul E. Lyon titled, "Axisymmetric Finite Element Modeling for the Design and Analysis of Cylindrical Adhesive Joints based on Dimensional Stability" [1], a two-dimensional axisymmetric finite element model was developed using energy techniques. A FORTRAN code was then implemented to solve the developed system of equations [K]{d}={R} for the unknown displacements {d}, where [K] is the global stiffness matrix and {R} is the global load vector. Using the model, cylindrical adhesive joint geometries were determined to optimize dimensional stability. The geometric parameters that were optimized were composite stacking sequence, bond length, and bond thickness.

Subsequent to the optimization of cylindrical adhesive joints for dimensional stability, it is important to be able to determine that the predicted geometry has sufficient strength. In the thesis submitted by Michael Lambert titled, "Investigation of the Design and Static Behavior of Cylindrical Tubular Composite Adhesive Joints Utilizing the Finite Element Method and Stress-Based Failure Theories" [2], failure criteria were implemented into the model and used to ensure that the optimized joints do not fail under the predicted loading specifications. In order to model all of the desired loading conditions, a 3D finite element model was developed and used to incorporate bending.

Up to this point, the models used have only been compared to the few analytical models available that pertain to cylindrical adhesive joints. These analytical models, due to the simplifying assumptions, do not fully capture the stress and displacement field of the joint. Because of this, it is desirable to verify the accuracy of the model through testing. In order to

correlate the finite element results with the test results accurate material properties must be procured. A series of tests are to be performed aimed at validating the trends seen in the model. Both thermal loading of the joints, as well as traditional mechanical loading type tests are to be performed to verify the model for accurate predictions of displacement trends.

Additional verification of the developed finite element model through testing is desirable to ensure the model is capturing the true stress and displacement field. The model was found to match the test data quantitatively. The prediction of trends, to enable the development of rules of thumb to be used in adhesive joint design was also achieved.

CHAPTER 2

LITERATURE REVIEW

2.1 Introduction

The literature review presented in this chapter covers thermal cycling and its effect on composite materials, previous numerical models applied to composites problems, as well as previous testing methods in the field of cryogenics. The goals in completing this literature review are as follows.

- To gain a general knowledge of composites and their behavior when subjected to thermal as well as mechanical loads
- To discover how composites are being modeled in cryogenic environments
- To explore ways people are gathering data at cryogenic temperatures and which worked well and what were the limitations
- And secondarily to ensure that the work that is proposed has not already been accomplished

With the knowledge gained from the literature review, development of a test regimen for validating an axisymmetric finite element model is within reason. The effect thermal cycling has on composite materials will be discussed first. Second, various models that have been developed to predict phenomena seen when composites are subject to thermal and mechanical loads is explored. Third, test methods for determining various parameters at cryogenic temperatures are discussed. A conclusion section summarizes why the gathered knowledge aides in obtaining the objectives of the current work.

2.2 Thermal Cycling

Understanding the effect of thermal cycling on composite materials is necessary to extend what has been learned to cylindrical adhesive joints. The study of these effects is recent when compared to other topics in structural mechanics. In 1998 N.L. Hancox [3] did a survey of work previously performed on this topic. Hancox states that for the past four decades that composites are ideal candidates for thermal cycling-damage. Because composites consist of at least two

different materials there inherently is a mismatch in CTE. To make the matter worse, many composites must be cured at high temperatures to allow for the matrix epoxy to crosslink properly. Thermal residual stresses are then introduced into the material directly after manufacture.

In an attempt to understand the effects of thermal cycling, Kim et al. [4] explored the tensile properties of a unidirectional composite which had been cycled with thermo-mechanical loads at cryogenic temperatures. They performed up to 10 cycles from room temperature to -150 °C (-238 °F). They conclude that low number cryogenic cycles with loads have little influence on the tensile stiffness despite existing micro-cracks in the matrix. They conclude that the reason for this is "because the residual compressive stresses induced during the cycles could allow the interface to have good bonding quality even though micro-cracks were formed by thermo mechanical cycles. Improved properties of the interface eventually result in an increase of strength for the laminate specimens after thermo-mechanical cycles [4: 88]." They also conclude that stiffness increases with decreasing temperature. It was found that the strength of the six-cycled specimen was almost equal at each temperature point. The CTEs of the laminates were also recorded over the temperature range. It was found that the longitudinal CTE varied linearly from a negative value to a positive one as temperature was lowered to cryogenic temperatures. The transverse CTE showed nonlinear behavior at low temperatures.

With similar objectives to Kim et al. [4], Cohen and Hyer [5], and Tompkins and Williams [6] performed extensive testing on composite tubes, which are of particular interest in the present work. The composite tubes were cycled between 93 and -156°C (199 and -249 °F). It was found that micro-crack accumulation leveled off between 10 and 50 thermal cycles. This work was later extended by Herakovich and Hyer [7] to include more temperature ranges, the new range was from -156 to 121°C (-249 to 250 °F). They also varied the cycling rate, one sixth times faster than the other, and found that more cracks developed when the slower cycle rate was used and concluded that creep may have been a factor. They also found the crack density was a

function of layer thickness and the number of 90° plies. It was also noted that cracking approached a limit after 500 cycles. Herakovich and Hyer also mention that the largest decrease in CTE occurred for specimen with the highest proportion of 90° plies although the main purpose of these studies was to investigate the damage induced by the thermal cycling.

Jones et al. [8] also studied carbon fiber tubes but with a different objective than the previously mentioned groups. Their concern was that the slight changes in dimension of the tubes would cause the surface coatings to fail. They cycled the thin walled [±30/±30/10/10/10] tubes up to 10,000 times from -101 to 93°C (-150 to 200 °F). The change in the CTE for the specimen either remained unchanged or showed an increased negative CTE. Kim et al. [9] studied the affect damage had on the CTEs of laminates. The range of temperature considered in the study was from -101°C to 121°C (-150 to 250 °F). The CTE was determined from a linear fit to the data over the entire test range. They found that the CTE of unidirectional laminates is unchanged after experiencing thermal cycling. The same was not found for cross ply laminates. The micro-cracking induced by the thermal cycling caused significant changes in the CTE. The CTE at 0 thermal cycles was found to be 2.6E-6/°C (1.44E-6/°F), a much different CTE was measured after 780 thermal cycles and was measured as 1.2E-6/°C (.666E-6/°F).

Ogihara et al. [10] took the investigation one step further. They explored not only the effect of just thermal cycling but explored the effect of thermal cycling on the matrix cracking behavior while under tensile loading. They found that the critical stress for matrix cracking is a decreasing function of the number of thermal cycles. Kim and Donaldson [11] also performed tests on laminates subject to thermal and mechanical loading. Unidirectional laminate panels were fabricated to determine the necessary thermoelastic properties, through testing, for calculation of the ply residual stresses. They found that while the residual stresses increase with decreasing test temperature, so do the composite transverse and shear strengths, and these two effects compete in their influence on the stress to initial micro-cracking.

Other tests relating to the affect temperature has on laminates, other than thermal cycling, were also investigated. Kumagai et al. [12] performed tensile and in-plane shear tests at room temperature as well as cryogenic temperatures. Tensile strength and modulus were evaluated for both directions of the composite. They found that these quantities are affected by temperature. Takeda et al. [13] and Shindo et al. [14] also performed tensile tests at cryogenic temperatures. They also found that the modulus increases with decreasing temperature. They also discuss the onset of a knee in the stress strain curve and conclude that this is due to the abrupt onset of micro-cracking at the strain corresponding to the knee.

Many other studies have been performed investigating what combinations of epoxy and fiber are resistant to various temperature effects. Timmerman et al. [15-16] explored the effect different combinations of epoxies and carbon fibers had on cryogenic micro-cracking. They found that matrix properties along with fiber tensile modulus had significant impact on the response of the composite to cryogenic cycling. Higher tensile moduli and linear coefficients of thermal expansion added to the micro-crack density. The addition of a rubber toughener prevented the formation of micro-cracks in all of the laminates studied. Studies have also been performed to investigate cure cycles that have positive effects on composite laminates to be used at cryogenic temperatures [17].

2.3 Models

The assumptions made in affective numerical models of composites are reviewed in this section. Many of the models were developed for differing reasons but parallels can be drawn to the current work in each.

A 2D finite element model was developed by Kumagai et al. [12]. The finite element analysis was used to study the stress distribution within the specimen and to help interpret the experimental measurements. They used the stress distributions predicted by the finite element analysis to investigate the experimentally induced error in determining the tensile strength. Plane-

stress conditions were assumed in the numerical analysis. They also assumed that the composite could be modeled by a homogeneous orthotropic material. They used the property data corresponding to the temperature of the test; room temperature, 77K, and 4K. The tensile test was simulated in the model by applying the uniformly distributed load as nodal forces. The gripping section of the test fixture was not included in the model because it was not the region of interest. Symmetry was taken advantage of and only one quarter of the test specimen needed to be modeled. 4 node quadrilateral elements were employed. They found that the stress strain curves for room temperature as well as liquid nitrogen temperature to be approximately linear.

Takeda et al. [13] also developed a finite element model. They to modeled the composite as a homogeneous material with orthotropic material properties. The elastic material properties were determined using a micromechanics model that utilized the unit cell approach. The properties input into the micromechanics model corresponded to the properties of the constituents, again at the corresponding temperatures of the tests. They noted that due to the fact that composites are manufacture at relatively high temperatures, and due to the mismatch in CTE of the fibers and matrix, residual thermal stresses exist in the material at cryogenic temperatures. But it was noted that the thermal stresses can relax during manufacturing because of the visco-elastic behavior of the epoxy resin and therefore the model was simplified by neglecting the residual thermal stresses. The dimensions in the finite element model matched that of the specimen (no scaling was performed) and they too went on the plane stress assumption. The gripped section was not included in the model once again due to the fact that it is not the region of interest. One quarter of the specimen was modeled taking advantage of symmetry. One major difference in this model was the use of a displacement boundary condition at the clamped end rather than the use of a uniform distributed load. Constant strain triangular elements were used.

Unlike the previous two, Shindo et al. [14] used micro mechanics to determine the effective elastic moduli under the assumption of uniform strain inside a representative volume element. After the moduli were determined plane stress elements were used in the finite element

model. Due to symmetry of the geometry and loading conditions only one quarter of the specimen was modeled. They concluded that the numerical prediction of the model was larger than the measured one. Therefore the model was determined to be conservative and could be used in design and in most cases the specifications would be met or exceeded.

Bartoszyk et al. [18] set out to develop a finite element model to aid in the design of the James Webb Space Telescope (JWST). The design required them to come up with composite truss tubes with high axial stiffness and low axial CTE. The structure needed to endure multiple thermal cycles without degrading more than the specified amount. One of the major challenges is the large thermal mismatch stresses between the metal fittings and the composite tubes at cryogenic temperatures. The moduli that were used were held constant and were given for 22K. The thermal expansion properties used were secant CTE from room temperature to 22K. Because the tubes used in the JWST were of square cross section, axisymmetric solid elements could not be used and therefore to keep the size of the model reasonable only one element was used through the thickness of the adhesive. They had assumed the failures would occur within the laminate and therefore the accuracy in the adhesive region was not as important, the assumption was to be verified by a test program. Because the work to be done is on cylindrical joints, axisymmetric elements are used and more elements can be used through the thickness of the adhesive.

Cofie et al. [19] also performed work on the JWST. They were faced with the challenge of designing to meet the very tight distortion requirements that were imposed on the ISIM structure. The major challenge was predicting the thermal distortion of the structure both from the bulk cooldown form ambient to cryogenic temperatures, and the smaller temperature changes within the cryogenic operating environment. They set out to determine the effective properties that needed to be employed to a bar element model to yield deformations within 5% of the actual deformation. Their approach was to generate a detailed solid element model of each joint along with a bar element model. They would then exercise both models under mechanical and thermal loads adjusting the bar element properties until the two models matched.

Nemes et al. [20] and Shi and Cheng [21] developed an analytical model for the stress analysis of cylindrical assembly of two tubes. Their method is a variational method applied on the potential energy of deformation. The method allows for the study of some geometrical or material parameters on the stress field. Other analytical models that were employed to try and predict stress fields included the Classical Lamination Plate Theory (CLT). Many other studies on the topic tried to employ complicated analytical models to predict failure [9,11,22-30]. It was found that the finite element method tended to yield more accurate results when compared to measured data.

Many of the same assumptions are found in all of the above models. Model reduction by the use of symmetry boundary conditions are seen throughout. Other attempts at model reduction were explored in the design of the JWST in finding effective properties to be used in a rod element formulation. Also the grip region is never included in the model do to the fact that it is not the region of interest. The plane stress element formulation is exclusively used throughout. Another interesting discovery is that the element of choice in the models is the lower order constant strain elements. The use of linear elastic material properties is justified in that it was shown through experiment that at room temperature as well as at liquid nitrogen temperature that the stress strain curve is approximately linear.

2.4 Testing Methods

In an effort to understand the different approaches to testing at cryogenic temperatures, the following articles were explored. It is desirable to determine which testing methods produced accurate results and how the accuracy of the results was verified. Again the following tests were performed to determine various different parameters but parallels can again be drawn to the current work.

Kim et al. [9] set out to investigate variations in the CTE of composite laminates with damage. The strains at different temperatures were gathered using strain gauges and allowed the

determination of the composites CTEs. Ultra-low-expansion titanium silicate was used for the reference material for the completion of the strain gauge bridge circuit. WK-series 350Ω strain gauges from Micro-Measurements, Inc., were chosen due to their ability to accurately measure strain into the cryogenic temperature domain. The DAQ systems reliability was verified by measuring the CTE of two known materials and comparing the measured value with corresponding published hand book values.

Similar to Kim et al. [9], Kim et al. [4] also used strain gauges to measure strain at cryogenic temperatures. They too chose to employ a Wheatstone half bridge completion circuit to compensate for induced thermal strain of the gauges. The dummy gauges were placed on titanium silicate blocks as is commonly used for a reference material due to its near zero CTE.

In order to determine material properties for use in their study Kumagai et al. [12] gathered strain measurements using 5mm strain gauges cemented directly to the specimen surfaces. They placed strain gauges in both the longitudinal and transverse directions so that Young's modulus as well as Poisson's ratio could be experimentally determined. They too achieved low temperatures by directly submersing the specimen in either a liquid helium or liquid nitrogen bath. Kim and Donaldson [11] specified that uni-directional (UD) composite specimen were used in a tensile test machine and loaded. The specimens were outfitted with strain gauges so that the properties of the material could be determined.

A different approach was taken by Takeda et al. [13]. They had found that failure of composites occurred at strains quite similar to the strain limit of strain gauges suitable for use at cryogenic temperatures. Therefore they employed an averaging extensometer system for measuring strain at liquid nitrogen temperatures. The gauge length of the extensometer was 25.4 mm. They also obtained low temperatures by immersing the specimen in liquid nitrogen.

A study to determine the time response of the composite samples was performed by Ogihara et al. prior to the work in [10]. They set out to study the affect thermal cycling had on the structural integrity of composites. They wanted to cycle the composites from -196 to 100 °C (-

321 to 212 °F). They determined the time schedule to reach these temperature values by measuring the temperature profile using thermocouples attached to the specimens. They found that one minute in liquid nitrogen was ample time to cool the specimen to a uniform -196 °C (-321 °F). Another study performed by Timmerman et al. [16] also placed specimen in liquid nitrogen baths but left the specimen in the bath of a much longer time period of 10 minutes.

Two options that resulted in accurate strain measurement at liquid nitrogen temperature are strain gauges cemented directly to the specimen or an averaging extensometer system. Both have advantages in differing situations. The use of titanium-silicate blocks as a reference material to place dummy strain gauges necessary for temperature induced strain compensation acquired by using the half Wheatstone bridge completion circuit. Varying time periods were used in ensuring the laminates had reached a state of uniform temperature from 1 to 10 minutes.

2.5 Conclusions and Final Thoughts

Thermal cycling of composites, due to the mismatch in CTEs of the fiber and composite, produces micro-cracking. It was found that for low cycle cryogenic cycling the strength of the composite is not affected. More extensive testing found that between 10 and 50 cycles the accumulation of micro-cracks leveled off and the micro-crack density leveled off permanently around 500 cycles. The behavior of composite laminates can be expanded and applied to that of cylindrical joints due to the fact that the joint ordinarily is composed of a composite, adhesive layer, and typically aluminum. The adhesive layer is of similar composition to the epoxy and can therefore be assumed to act similarly. Plane stress was assumed in the development of all of the finite element models. When the type of element was presented in all cases lower order constant strain elements were used. To minimize model size symmetry was taken advantage of by applying symmetry boundary conditions. The loading was either modeled as a distributed load along the edge of the grip or a displacement boundary condition. In all cases the grip portion of the specimen was not included because it was not the area of interest. With respect to testing the

cryogenic environment was obtained by immersing the specimen in a liquid nitrogen or liquid helium bath. The time in the bath to attain a constant temperature state varied from one to ten minutes. WK-series strain gauges were found to yield desirable results when care was taken to ensure proper application. Titanium-silicate was used as a reference material for thermal induced apparent strain compensation in the half Wheatstone bridge configuration. In one study a strain averaging extensometer system was used because it was found that composite failure at cryogenic temperatures was found to be near the strain limit of strain gauges. The extensometer set up also requires less preparation and in the current work can be used to average the strain over the joint area.

CHAPTER 3

OBJECTIVES

The purpose of the research is to obtain data that can be used to verify the validity of the finite element method as a tool to design cylindrical adhesive joint for dimensional stability. This purpose is accomplished by completing the following objectives.

- Selection of an adhesive that performs well at cryogenic temperatures and meets NASA's low out-gassing standards
- Selection of the proper testing equipment that is suited for use at cryogenic temperatures
- Selection of appropriate extensometer model to obtain accurate readings
- Verification of the test setup's ability to correctly record load and displacement data
- Verification of the model's ability to accurately predict trends seen in tensile testing of joints with varying composite layups at room temperature
- Verification of the model's ability to accurately predict trends seen in tensile testing of joints with varying composite layups at cryogenic temperatures
- Thermally cycling joints and simultaneously recording joint displacement to obtain CTEs for the joint as well as investigate joint behavior with thermal cycling
- Verification of the model's ability to accurately predict displacements associated with thermal loading
- Summarization of the results and provide insight into possible differences in the model's prediction and test data
- Recommendation of future work and possible improvements in testing procedure
- Adding to the finite element program the ability to model cylindrical insert joints.

CHAPTER 4

FINITE ELEMENT METHOD DEVELOPMENT

4.1 Variational Derivation of 3D Equilibrium Equations

The derivation of the equilibrium equations are shown using a variational approach to show that the integral form indeed contains the equilibrium equations along with the nonessential boundary conditions. The principle of minimum total potential energy states:

> Among all admissible configurations of a conservative system, those that satisfy the equations of equilibrium make the potential energy stationary with respect to small admissible variations of displacement.

In order to utilize the principle of minimum potential energy the strain energy density function must be defined. Because our problem is cylindrical in nature the problem will be presented using the cylindrical coordinate system. A typical cylindrical adhesive joint is shown in Figure 1.

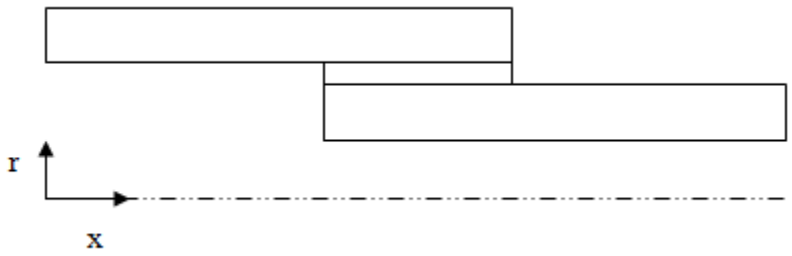

Figure 1. A typical cylindrical adhesive joint.

The strain energy density function is obtained using the following definition:

$$W = \int_V \frac{1}{2}\sigma\epsilon dV \tag{1}$$

A constitutive relationship must now be defined to express the stress in terms of the strains. The following constitutive relationship, transformed from the layer coordinate system 1-2-3 into the global coordinate system x-θ-r. Summing moments about the x and r axis symmetry of the stress

tensor field is defined as follows. With the relationship in Eq. (2) the constitutive relationship can be defined as in Eq. (3).

$$\begin{aligned} \tau_{rx} &= \tau_{xr} \\ \tau_{r\theta} &= \tau_{\theta r} \\ \tau_{\theta x} &= \tau_{x\theta} \end{aligned} \tag{2}$$

$$\begin{Bmatrix} \sigma_x \\ \sigma_\theta \\ \sigma_r \\ \tau_{\theta r} \\ \tau_{xr} \\ \tau_{x\theta} \end{Bmatrix} = \begin{bmatrix} \overline{C_{11}} & \overline{C_{12}} & \overline{C_{13}} & 0 & 0 & \overline{C_{16}} \\ \overline{C_{12}} & \overline{C_{22}} & \overline{C_{23}} & 0 & 0 & \overline{C_{26}} \\ \overline{C_{13}} & \overline{C_{23}} & \overline{C_{33}} & 0 & 0 & \overline{C_{36}} \\ 0 & 0 & 0 & \overline{C_{44}} & \overline{C_{45}} & 0 \\ 0 & 0 & 0 & \overline{C_{45}} & \overline{C_{55}} & 0 \\ \overline{C_{16}} & \overline{C_{26}} & \overline{C_{36}} & 0 & 0 & \overline{C_{66}} \end{bmatrix} \begin{Bmatrix} \epsilon_x \\ \epsilon_\theta \\ \epsilon_r \\ 2\epsilon_{\theta r} \\ 2\epsilon_{xr} \\ 2\epsilon_{x\theta} \end{Bmatrix} \tag{3}$$

The transformed stiffness values in Eq. (3) are defined in terms of the untransformed stiffness values as follows.

$$\overline{C_{11}} = C_{11}m^4 + 2\left(C_{12} + 2C_{66}\right)m^2n^2 + C_{22}n^4 \tag{4}$$

$$\overline{C_{12}} = \left(C_{11} + C_{12} - 4C_{66}\right)m^2n^2 + C_{12}\left(n^4 + m^4\right) \tag{5}$$

$$\overline{C_{13}} = C_{13}m^2 + C_{23}n^2 \tag{6}$$

$$\overline{C_{16}} = -mn^3C_{22} + m^3nC_{11} = mn\left(m^2 - n^2\right)\left(C_{12} + 2C_{66}\right) \tag{7}$$

$$\overline{C_{22}} = C_{11}n^4 + 2\left(C_{12} + 2C_{66}\right)m^2n^2 + C_{22}m^4 \tag{8}$$

$$\overline{C_{23}} = n^2C_{13} + m^2C_{23} \tag{9}$$

$$\overline{C_{26}} = -m^3nC_{22} + mn^3C_{11} + mn\left(m^2 - n^2\right)\left(C_{12} + 2C_{66}\right) \tag{10}$$

$$\overline{C_{33}} = C_{33} \tag{11}$$

$$\overline{C_{36}} = \left(C_{13} - C_{23}\right)mn \tag{12}$$

$$\overline{C_{44}} = C_{44}m^2 + C_{55}n^2 \tag{13}$$

$$\overline{C_{45}} = \left(C_{55} - C_{44}\right)mn \tag{14}$$

$$\overline{C_{55}} = C_{55}m^2 + C_{44}n^2 \tag{15}$$

$$\overline{C_{66}} = \left(C_{11} + C_{22} - 2C_{12}\right)m^2n^2 + C_{66}\left(m^2 - n^2\right)^2 \tag{16}$$

Now the strain energy density function can be defined in terms of the strains and stiffness.

$$\begin{aligned} W = \int_V \{ &\frac{1}{2}\overline{C_{11}}\epsilon_x^2 + \overline{C_{12}}\epsilon_x\epsilon_{x\theta} + \overline{C_{13}}\epsilon_x\epsilon_r + 2\overline{C_{16}}\epsilon_x\epsilon_{x\theta} + \frac{1}{2}\overline{C_{22}}\epsilon_\theta^2 + \overline{C_{23}}\epsilon_r\epsilon_\theta + 2\overline{C_{26}}\epsilon_\theta\epsilon_{x\theta} + \dots \\ &\frac{1}{2}\overline{C_{33}}\epsilon_r^2 + 2\overline{C_{36}}\epsilon_r\epsilon_{x\theta} + 2\overline{C_{44}}\epsilon_{\theta r}^2 + 4\overline{C_{45}}\epsilon_{xr}\epsilon_{\theta r} + 2\overline{C_{55}}\epsilon_{xr}^2 + 2\overline{C_{66}}\epsilon_{x\theta}^2 \} r dr d\theta dx \end{aligned} \tag{17}$$

Assuming small displacements and similarly small strains, the strain-displacement relations for cylindrical coordinates are defined as follows.

$$\epsilon_x = \frac{\partial u}{\partial x} \tag{18}$$

$$\epsilon_\theta = \frac{w}{r} + \frac{1}{r}\frac{\partial v}{\partial \theta} \tag{19}$$

$$\epsilon_r = \frac{\partial w}{\partial r} \tag{20}$$

$$2\epsilon_{\theta r} = \frac{\partial v}{\partial r} + \frac{1}{r}\frac{\partial w}{\partial \theta} - \frac{v}{r} \tag{21}$$

$$2\epsilon_{xr} = \frac{\partial w}{\partial x} + \frac{\partial u}{\partial r} \tag{22}$$

$$2\epsilon_{x\theta} = \frac{1}{r}\frac{\partial u}{\partial \theta} + \frac{\partial v}{\partial x} \tag{23}$$

The strain energy density function can now be expressed only as a function of the orthotropic stiffness terms and the three unknown displacements u, v, and w in the x, θ, and r-direction respectively.

$$\int_V \{\overline{C_{11}}\left[\frac{1}{2}r\frac{\partial u}{\partial x}^2\right]+\overline{C_{12}}\left[\frac{\partial u}{\partial x}\frac{\partial v}{\partial \theta}+\frac{\partial u}{\partial x}w\right]+\overline{C_{13}}\left[r\frac{\partial u}{\partial x}\frac{\partial w}{\partial r}\right]+\overline{C_{16}}\left[r\frac{\partial u}{\partial x}\frac{\partial v}{\partial x}+\frac{\partial u}{\partial x}\frac{\partial u}{\partial \theta}\right]+\ldots$$
$$\overline{C_{22}}\left[\frac{1}{2}\frac{1}{r}\frac{\partial v}{\partial \theta^2}+\frac{1}{2}\frac{1}{r}w^2+\frac{1}{r}\frac{\partial v}{\partial \theta}w\right]+\overline{C_{23}}\left[\frac{\partial v}{\partial \theta}\frac{\partial w}{\partial r}+w\frac{\partial w}{\partial r}\right]+\ldots$$
$$\overline{C_{26}}\left[\frac{1}{r}\frac{\partial u}{\partial \theta}\frac{\partial v}{\partial \theta}+\frac{1}{r}\frac{\partial u}{\partial \theta}w+\frac{\partial^2 v}{\partial x\partial \theta}+\frac{\partial v}{\partial x}w\right]+\overline{C_{33}}\left[\frac{1}{2}r\frac{\partial w}{\partial r}^2\right]+\overline{C_{36}}\left[\frac{\partial u}{\partial \theta}\frac{\partial w}{\partial r}+r\frac{\partial v}{\partial x}\frac{\partial w}{\partial r}\right]+\ldots \quad (24)$$
$$\overline{C_{44}}\left[\frac{1}{2}\frac{1}{r}v^2+\frac{1}{2}r\frac{\partial v}{\partial r}^2+\frac{\partial v}{\partial r}v+\frac{\partial v}{\partial r}\frac{\partial w}{\partial \theta}-\frac{1}{r}v\frac{\partial w}{\partial \theta}+\frac{1}{2}\frac{1}{r}\frac{\partial w}{\partial \theta^2}\right]+\ldots$$
$$\overline{C_{45}}\left[-\frac{\partial u}{\partial r}v+r\frac{\partial u}{\partial r}\frac{\partial v}{\partial r}+\frac{\partial u}{\partial r}\frac{\partial w}{\partial \theta}+r\frac{\partial v}{\partial r}\frac{\partial w}{\partial x}-v\frac{\partial w}{\partial x}+\frac{\partial^2 w}{\partial x\partial \theta}\right]+\ldots$$
$$\overline{C_{55}}\left[\frac{1}{2}r\frac{\partial u}{\partial r}^2+r\frac{\partial u}{\partial r}\frac{\partial w}{\partial x}+\frac{1}{2}r\frac{\partial w}{\partial x}^2\right]+\overline{C_{66}}\left[\frac{1}{2}\frac{1}{r}\frac{\partial u}{\partial \theta^2}+\frac{\partial u}{\partial \theta}\frac{\partial v}{\partial x}+\frac{1}{2}r\frac{\partial v}{\partial x}^2\right]\}drd\theta dx$$

Now that we have obtained the strain energy density function in terms of our unknown displacements the principle of minimum potential energy can be applied to find the stationary point of the functional and therefore the equilibrium equations and corresponding nonessential boundary conditions. The potential energy becomes stationary when the first variation of the strain energy density function is equal to zero.

$$\delta W = 0 \quad (25)$$

Because the strain energy density function represents the strain energy in three dimensions the functional must be varied in the three coordinate directions to obtain the three equilibrium equations. This process can be done independently and first u will be varied.

$$\int_V \{\overline{C_{11}}\left[r\frac{\partial u}{\partial x}\delta\left(\frac{\partial u}{\partial x}\right)\right]+\overline{C_{12}}\left[\frac{\partial v}{\partial \theta}\delta\left(\frac{\partial u}{\partial x}\right)+w\delta\left(\frac{\partial u}{\partial x}\right)\right]+\overline{C_{13}}\left[r\frac{\partial w}{\partial r}\delta\left(\frac{\partial u}{\partial x}\right)\right]+\ldots$$
$$\overline{C_{16}}\left[r\frac{\partial v}{\partial x}\delta\left(\frac{\partial u}{\partial x}\right)+\frac{\partial u}{\partial x}\delta\left(\frac{\partial u}{\partial \theta}\right)+\frac{\partial u}{\partial \theta}\delta\left(\frac{\partial u}{\partial x}\right)\right]+\overline{C_{26}}\left[\frac{1}{r}\frac{\partial v}{\partial \theta}\delta\left(\frac{\partial u}{\partial \theta}\right)+\frac{1}{r}w\delta\left(\frac{\partial u}{\partial \theta}\right)\right]+\ldots \quad (26)$$
$$\overline{C_{36}}\left[\frac{\partial w}{\partial r}\delta\left(\frac{\partial u}{\partial \theta}\right)\right]+\overline{C_{45}}\left[-v\delta\left(\frac{\partial u}{\partial r}\right)+r\frac{\partial v}{\partial r}\delta\left(\frac{\partial u}{\partial r}\right)+\frac{\partial w}{\partial \theta}\delta\left(\frac{\partial u}{\partial r}\right)\right]+\ldots$$
$$\overline{C_{55}}\left[r\frac{\partial u}{\partial r}\delta\left(\frac{\partial u}{\partial r}\right)+r\frac{\partial w}{\partial x}\delta\left(\frac{\partial u}{\partial r}\right)\right]+\overline{C_{66}}\left[\frac{1}{r}\frac{\partial u}{\partial \theta}\delta\left(\frac{\partial u}{\partial \theta}\right)+\frac{\partial v}{\partial x}\delta\left(\frac{\partial u}{\partial \theta}\right)\right]\}drd\theta dx$$

Integration by parts must now be performed to lower the order of the variations to a zeroth order derivative. The general form of integration by parts will be used and is placed here for reference.

$$\begin{aligned}\int_V g\frac{\partial f}{\partial x}dV &= -\int_V f\frac{\partial g}{\partial x}dV + \int_V \frac{\partial}{\partial x}(fg)dV \\ \int_V g\frac{\partial f}{\partial r}dV &= -\int_V f\frac{\partial g}{\partial r}dV + \int_V \frac{\partial}{\partial r}(fg)dV \\ \int_V g\frac{\partial f}{\partial \theta}dV &= -\int_V f\frac{\partial g}{\partial \theta}dV + \int_V \frac{\partial}{\partial \theta}(fg)dV\end{aligned} \tag{27}$$

The first term in the integration by parts yields the equilibrium equation while the second term becomes the boundary terms. Initially only the first term will be kept to come up with the equilibrium equations and the boundary terms will be considered afterwards.

$$\begin{aligned}&-\int_V \{\overline{C_{11}}\left[r\frac{\partial^2 u}{\partial x^2}\right] + \overline{C_{12}}\left[\frac{\partial^2 v}{\partial\theta\partial x} + \frac{\partial w}{\partial x}\right] + \overline{C_{13}}\left[r\frac{\partial^2 w}{\partial r\partial x}\right] + \dots \\ &\overline{C_{16}}\left[r\frac{\partial^2 v}{\partial x^2} + \frac{\partial^2 u}{\partial x\partial\theta} + \frac{\partial^2 u}{\partial x\partial\theta}\right] + \overline{C_{26}}\left[\frac{1}{r}\frac{\partial^2 v}{\partial\theta^2} + \frac{1}{r}\frac{\partial w}{\partial\theta}\right] + \dots \\ &\overline{C_{36}}\left[\frac{\partial^2 w}{\partial r\partial\theta}\right] + \overline{C_{45}}\left[-\frac{\partial v}{\partial r} + r\frac{\partial^2 v}{\partial r^2} + \frac{\partial v}{\partial r} + \frac{\partial^2 w}{\partial\theta\partial r}\right] + \dots \\ &\overline{C_{55}}\left[r\frac{\partial^2 u}{\partial r^2} + \frac{\partial u}{\partial r} + r\frac{\partial^2 w}{\partial x\partial r} + \frac{\partial w}{\partial x}\right] + \overline{C_{66}}\left[\frac{1}{r}\frac{\partial^2 u}{\partial\theta^2} + \frac{\partial^2 v}{\partial x\partial\theta}\right]\}\delta u dr d\theta dx\end{aligned} \tag{28}$$

Using the fundamental lemma of calculus of variations the terms inside the integration must go to zero for the functional to be stationary. This can be understood by reasoning that the variation of u is arbitrary so for the variation with respect to u to be equal to zero all of the other terms must sum to zero. Therefore by dividing by r and setting equal to zero the following expressing is obtained.

$$\begin{aligned}
&\overline{C_{11}}\left[\frac{\partial^2 u}{\partial x^2}\right]+\overline{C_{12}}\frac{1}{r}\left[\frac{\partial^2 v}{\partial\theta\partial x}+\frac{\partial w}{\partial x}\right]+\overline{C_{13}}\left[\frac{\partial^2 w}{\partial r\partial x}\right]+\overline{C_{16}}\left[\frac{\partial^2 v}{\partial x^2}+\frac{1}{r}\frac{\partial^2 u}{\partial x\partial\theta}+\frac{1}{r}\frac{\partial^2 u}{\partial x\partial\theta}\right]+\ldots\\
&\overline{C_{26}}\frac{1}{r}\left[\frac{1}{r}\frac{\partial^2 v}{\partial\theta^2}+\frac{1}{r}\frac{\partial w}{\partial\theta}\right]+\overline{C_{36}}\frac{1}{r}\left[\frac{\partial^2 w}{\partial r\partial\theta}\right]+\overline{C_{45}}\left[-\frac{1}{r}\frac{\partial v}{\partial r}+\frac{\partial^2 v}{\partial r^2}+\frac{1}{r}\frac{\partial v}{\partial r}+\frac{1}{r}\frac{\partial^2 w}{\partial\theta\partial r}\right]+\ldots\\
&\overline{C_{55}}\left[\frac{\partial^2 u}{\partial r^2}+\frac{1}{r}\frac{\partial u}{\partial r}+\frac{\partial^2 w}{\partial x\partial r}+\frac{1}{r}\frac{\partial w}{\partial x}\right]+\overline{C_{66}}\frac{1}{r}\left[\frac{1}{r}\frac{\partial^2 u}{\partial\theta^2}+\frac{\partial^2 v}{\partial x\partial\theta}\right]=0
\end{aligned}\tag{29}$$

Rearranging and grouping terms yields the equilibrium equation in the x-direction.

$$\begin{aligned}
&\frac{\partial}{\partial x}\left\{\overline{C_{11}}\left[\frac{\partial u}{\partial x}\right]+\overline{C_{12}}\frac{1}{r}\left[\frac{\partial v}{\partial\theta}+w\right]+\overline{C_{13}}\left[\frac{\partial w}{\partial r}\right]+\overline{C_{16}}\left[\frac{\partial v}{\partial x}+\frac{1}{r}\frac{\partial u}{\partial\theta}\right]\right\}+\ldots\\
&\frac{1}{r}\frac{\partial}{\partial\theta}\left\{\overline{C_{16}}\left[\frac{\partial u}{\partial x}\right]+\overline{C_{26}}\left[\frac{1}{r}\frac{\partial v}{\partial\theta}+\frac{1}{r}w\right]+\overline{C_{36}}\left[\frac{\partial w}{\partial r}\right]+\overline{C_{66}}\left[\frac{1}{r}\frac{\partial u}{\partial\theta}+\frac{\partial v}{\partial x}\right]\right\}+\ldots\\
&\left\{\overline{C_{45}}\left[-\frac{1}{r}\frac{\partial v}{\partial r}+\frac{\partial^2 v}{\partial r^2}+\frac{1}{r}\frac{\partial v}{\partial r}+\frac{1}{r}\frac{\partial^2 w}{\partial\theta\partial r}\right]+\overline{C_{55}}\left[\frac{\partial^2 u}{\partial r^2}+\frac{1}{r}\frac{\partial u}{\partial r}+\frac{\partial^2 w}{\partial x\partial r}+\frac{1}{r}\frac{\partial w}{\partial x}\right]\right\}=0
\end{aligned}\tag{30}$$

The bracketed terms in the equation above correspond to the terms in brackets below and the equilibrium equation in the x-direction is obtained.

$$\frac{\partial}{\partial x}\{\sigma_x\}+\frac{1}{r}\frac{\partial}{\partial\theta}\{\tau_{\theta x}\}+\left\{\frac{\partial\tau_{rx}}{\partial r}+\frac{\tau_{rx}}{r}\right\}=0\tag{31}$$

Now we must consider the boundary terms that were produced in the integration by parts. Using gauss's divergence theorem,

$$\begin{aligned}
\int_V\frac{\partial}{\partial x}(fg)\,dV&=\int_\Gamma(fg)n_x\,dS\\
\int_V\frac{\partial}{\partial\theta}(fg)\,dV&=\int_\Gamma(fg)n_\theta\,dS\\
\int_V\frac{\partial}{\partial r}(fg)\,dV&=\int_\Gamma(fg)n_r\,dS
\end{aligned}\tag{32}$$

The boundary terms are as follows: where the Γ is the corresponding surface and the hatted terms are unit vectors normal to the surface.

$$\begin{aligned}
&\int_\Gamma \{\overline{C_{11}}\left[\frac{\partial u}{\partial x}\right]+\overline{C_{12}}\frac{1}{r}\left[\frac{\partial v}{\partial \theta}+w\right]+\overline{C_{13}}\left[\frac{\partial w}{\partial r}\right]+\overline{C_{16}}\left[\frac{\partial v}{\partial x}+\frac{1}{r}\frac{\partial u}{\partial \theta}\right]\}n_x r dr d\theta(\delta u)|_\Gamma+\ldots\\
&\int_\Gamma \{\overline{C_{16}}\left[\frac{\partial u}{\partial x}\right]+\overline{C_{26}}\left[\frac{1}{r}\frac{\partial v}{\partial \theta}+\frac{1}{r}w\right]+\overline{C_{36}}\left[\frac{\partial w}{\partial r}\right]+\overline{C_{66}}\left[\frac{1}{r}\frac{\partial u}{\partial \theta}+\frac{\partial v}{\partial x}\right]\}n_\theta dr dx(\delta u)|_\Gamma+\ldots\\
&\int_\Gamma \{\overline{C_{45}}\left[\frac{-v}{r}+\frac{\partial v}{\partial r}+\frac{1}{r}\frac{\partial w}{\partial \theta}\right]+\overline{C_{55}}\left[\frac{\partial u}{\partial r}+\frac{\partial w}{\partial x}\right]\}\widehat{n_r r dx d\theta}(\delta u)|_\Gamma=0
\end{aligned} \tag{33}$$

Again the bracketed terms above correspond to the bracketed terms below and the boundary conditions corresponding to the x-direction equilibrium are obtained.

$$\int_\Gamma \{\sigma_x\}n_x r dr d\theta(\delta u)|_\Gamma+\int_\Gamma \{\tau_{x\theta}\}n_\theta dr dx(\delta u)|_\Gamma+\int_\Gamma \{\tau_{xr}\}n_r r dx d\theta(\delta u)|_\Gamma=0 \tag{34}$$

Following the same procedure as was done to obtain the equilibrium equation in the x-direction the equilibrium equation for the θ-direction will be obtained next by varying v.

$$\begin{aligned}
&\int_V \{\overline{C_{12}}\left[\frac{\partial u}{\partial x}\delta\left(\frac{\partial v}{\partial \theta}\right)\right]+\overline{C_{16}}\left[r\frac{\partial u}{\partial x}\delta\left(\frac{\partial v}{\partial x}\right)\right]+\overline{C_{22}}\left[\frac{1}{r}\frac{\partial v}{\partial \theta}\delta\left(\frac{\partial v}{\partial \theta}\right)+\frac{1}{r}w\delta\left(\frac{\partial v}{\partial \theta}\right)\right]+\ldots\\
&\overline{C_{23}}\left[\frac{\partial w}{\partial r}\delta\left(\frac{\partial v}{\partial \theta}\right)\right]+\left[\frac{1}{r}\frac{\partial u}{\partial \theta}\delta\left(\frac{\partial v}{\partial \theta}\right)+\frac{\partial v}{\partial x}\delta\left(\frac{\partial v}{\partial \theta}\right)+\frac{\partial v}{\partial \theta}\delta\left(\frac{\partial v}{\partial x}\right)+w\delta\left(\frac{\partial v}{\partial x}\right)\right]+\ldots\\
&\overline{C_{36}}\left[r\frac{\partial w}{\partial r}\delta\left(\frac{\partial v}{\partial x}\right)\right]+\ldots\\
&\overline{C_{44}}\left[\frac{1}{r}v\delta(v)+r\frac{\partial v}{\partial r}\delta\left(\frac{\partial v}{\partial r}\right)+\frac{\partial v}{\partial r}\delta(v)+v\delta\left(\frac{\partial v}{\partial r}\right)+\frac{\partial w}{\partial \theta}\delta\left(\frac{\partial v}{\partial r}\right)-\frac{1}{r}\frac{\partial w}{\partial \theta}\delta(v)\right]+\ldots\\
&\overline{C_{45}}\left[-\frac{\partial u}{\partial r}\delta(v)+r\frac{\partial u}{\partial r}\delta\left(\frac{\partial v}{\partial r}\right)+r\frac{\partial w}{\partial x}\delta\left(\frac{\partial v}{\partial r}\right)-\frac{\partial w}{\partial x}\delta(v)\right]+\ldots\\
&\overline{C_{66}}\left[\frac{\partial u}{\partial \theta}\delta\left(\frac{\partial v}{\partial x}\right)+r\frac{\partial v}{\partial x}\delta\left(\frac{\partial v}{\partial x}\right)\right]\}dr d\theta dx
\end{aligned} \tag{35}$$

Again using integration by parts to lower the order of the variation and temporarily only considering the first term yields:

$$
\begin{aligned}
&-\int_V \{\overline{C_{12}}\left[\frac{\partial^2 u}{\partial x \partial \theta}\right]+\overline{C_{16}}\left[r\frac{\partial^2 u}{\partial x^2}\right]+\overline{C_{22}}\left[\frac{1}{r}\frac{\partial^2 v}{\partial \theta^2}+\frac{1}{r}\frac{\partial w}{\partial \theta}\right]+\overline{C_{23}}\left[\frac{\partial^2 w}{\partial r \partial \theta}\right]+\ldots \\
&\overline{C_{26}}\left[\frac{1}{r}\frac{\partial^2 u}{\partial \theta^2}+\frac{\partial^2 v}{\partial x \partial \theta}+\frac{\partial^2 v}{\partial \theta \partial x}+\frac{\partial w}{\partial x}\right]+\overline{C_{36}}\left[r\frac{\partial^2 w}{\partial r \partial x}\right]+\ldots \\
&\overline{C_{44}}\left[-\frac{1}{r}v+r\frac{\partial^2 v}{\partial r^2}-\frac{\partial v}{\partial r}+\frac{\partial v}{\partial r}+\frac{\partial v}{\partial r}+\frac{\partial^2 w}{\partial \theta \partial r}+\frac{1}{r}\frac{\partial w}{\partial \theta}\right]+\ldots \\
&\overline{C_{45}}\left[\frac{\partial u}{\partial r}+r\frac{\partial^2 u}{\partial r^2}+\frac{\partial u}{\partial r}+r\frac{\partial^2 w}{\partial x \partial r}+\frac{\partial w}{\partial x}+\frac{\partial w}{\partial x}\right]+\overline{C_{66}}\left[\frac{\partial^2 u}{\partial \theta \partial x}+r\frac{\partial^2 v}{\partial x^2}\right]\}\delta v dr d\theta dx
\end{aligned}
\tag{36}
$$

Applying the fundamental lemma of variational calculus and dividing by r yields:

$$
\begin{aligned}
&\overline{C_{16}}\left[\frac{\partial^2 u}{\partial x^2}\right]+\overline{C_{36}}\left[\frac{\partial^2 w}{\partial r \partial x}\right]+\overline{C_{26}}\frac{1}{r}\left[\frac{\partial^2 v}{\partial \theta \partial x}+\frac{\partial w}{\partial x}\right]+\overline{C_{66}}\left[\frac{1}{r}\frac{\partial^2 u}{\partial \theta \partial x}+\frac{\partial^2 v}{\partial x^2}\right]+\ldots \\
&\overline{C_{12}}\left[\frac{1}{r}\frac{\partial^2 u}{\partial x \partial \theta}\right]+\overline{C_{22}}\frac{1}{r}\left[\frac{1}{r}\frac{\partial^2 v}{\partial \theta^2}+\frac{1}{r}\frac{\partial w}{\partial \theta}\right]+\overline{C_{23}}\left[\frac{1}{r}\frac{\partial^2 w}{\partial r \partial \theta}\right]+\overline{C_{26}}\frac{1}{r}\left[\frac{1}{r}\frac{\partial^2 u}{\partial \theta^2}+\frac{\partial^2 v}{\partial x \partial \theta}\right]+\ldots \\
&\overline{C_{45}}\left[\frac{1}{r}2\frac{\partial u}{\partial r}+\frac{\partial^2 u}{\partial r^2}+\frac{\partial^2 w}{\partial x \partial r}+\frac{1}{r}2\frac{\partial w}{\partial x}\right]+\overline{C_{44}}\left[-\frac{1}{r^2}v+\frac{\partial^2 v}{\partial r^2}+\frac{1}{r}\frac{\partial v}{\partial r}+\frac{1}{r}\frac{\partial^2 w}{\partial \theta \partial r}+\frac{1}{r^2}\frac{\partial w}{\partial \theta}\right]=0
\end{aligned}
\tag{37}
$$

Rearranging and grouping terms yields the equilibrium equation in the θ-direction.

$$
\begin{aligned}
&\frac{\partial}{\partial x}\left\{\overline{C_{16}}\left[\frac{\partial u}{\partial x}\right]+\overline{C_{36}}\left[\frac{\partial w}{\partial r}\right]+\overline{C_{26}}\frac{1}{r}\left[\frac{\partial v}{\partial \theta}+w\right]+\overline{C_{66}}\left[\frac{1}{r}\frac{\partial u}{\partial \theta}+\frac{\partial v}{\partial x}\right]\right\}+\ldots \\
&\frac{1}{r}\frac{\partial}{\partial \theta}\left\{\overline{C_{12}}\left[\frac{\partial u}{\partial x}\right]+\overline{C_{22}}\left[\frac{1}{r}\frac{\partial v}{\partial \theta}+\frac{1}{r}w\right]+\overline{C_{23}}\left[\frac{\partial w}{\partial r}\right]+\overline{C_{26}}\left[\frac{1}{r}\frac{\partial u}{\partial \theta}+\frac{\partial v}{\partial x}\right]\right\}+\ldots \\
&\left\{\overline{C_{45}}\left[\frac{1}{r}2\frac{\partial u}{\partial r}+\frac{\partial^2 u}{\partial r^2}+\frac{\partial^2 w}{\partial x \partial r}+\frac{1}{r}2\frac{\partial w}{\partial x}\right]+\overline{C_{44}}\left[-\frac{1}{r^2}v+\frac{\partial^2 v}{\partial r^2}+\frac{1}{r}\frac{\partial v}{\partial r}+\frac{1}{r}\frac{\partial^2 w}{\partial \theta \partial r}+\frac{1}{r^2}\frac{\partial w}{\partial \theta}\right]\right\}=0
\end{aligned}
\tag{38}
$$

The bracketed terms in the equation above correspond to the terms in brackets below and the equilibrium equation in the θ-direction is obtained.

$$
\frac{\partial}{\partial x}\{\tau_{\theta x}\}+\frac{1}{r}\frac{\partial}{\partial \theta}\{\sigma_\theta\}+\left\{\frac{\partial \tau_{r\theta}}{\partial r}+\frac{2\tau_{r\theta}}{r}\right\}=0 \tag{39}
$$

After again applying gauss's divergence theorem the boundary terms are as follows: where the Γ is the corresponding surface and the hatted terms are unit vectors normal to the surface.

$$\int_\Gamma \left\{ \overline{C_{16}}\left[\frac{\partial u}{\partial x}\right] + \overline{C_{26}}\frac{1}{r}\left[\frac{\partial v}{\partial \theta} + w\right] + \overline{C_{36}}\left[\frac{\partial w}{\partial r}\right] + \overline{C_{66}}\left[\frac{1}{r}\frac{\partial u}{\partial \theta} + \frac{\partial v}{\partial x}\right] \right\} n_x r dr d\theta (\delta v)|_\Gamma + \dots$$

$$\int_\Gamma \left\{ \overline{C_{12}}\left[\frac{\partial u}{\partial x}\right] + \overline{C_{22}}\frac{1}{r}\left[\frac{\partial v}{\partial \theta} + w\right] + \overline{C_{23}}\left[\frac{\partial w}{\partial r}\right] + \overline{C_{26}}\left[\frac{1}{r}\frac{\partial u}{\partial \theta} + \frac{\partial v}{\partial x}\right] \right\} n_\theta dr dx (\delta v)|_\Gamma + \dots \quad (40)$$

$$\int_\Gamma \left\{ \overline{C_{44}}\left[\frac{\partial v}{\partial r} + \frac{1}{r}v + \frac{1}{r}\frac{\partial w}{\partial \theta}\right] + \overline{C_{45}}\left[\frac{\partial u}{\partial r} + \frac{\partial w}{\partial x}\right] \right\} \widehat{n_r r dx d\theta} (\delta v)|_\Gamma = 0$$

Again the bracketed terms above correspond to the bracketed terms below and the boundary conditions corresponding the θ-direction equilibrium are obtained.

$$\int_\Gamma \{\tau_{x\theta}\} n_x r dr d\theta (\delta v)|_\Gamma + \int_\Gamma \{\sigma_\theta\} n_\theta dr dx (\delta v)|_\Gamma + \int_\Gamma \{\tau_{\theta r}\} n_r r dx d\theta (\delta v)|_\Gamma = 0 \quad (41)$$

Lastly the equilibrium equation in the r-direction can be obtained by varying w.

$$\int_V \{ \overline{C_{12}}\left[\frac{\partial u}{\partial x}\delta(w)\right] + \overline{C_{13}}\left[r\frac{\partial u}{\partial x}\delta\left(\frac{\partial w}{\partial r}\right)\right] + \overline{C_{22}}\left[\frac{1}{r}w\delta(w) + \frac{1}{r}\frac{\partial v}{\partial \theta}\delta(w)\right] + \dots$$

$$\overline{C_{23}}\left[\frac{\partial v}{\partial \theta}\delta\left(\frac{\partial w}{\partial r}\right) + w\delta\left(\frac{\partial w}{\partial r}\right) + \frac{\partial w}{\partial r}\delta(w)\right] + \overline{C_{26}}\left[\frac{1}{r}\frac{\partial u}{\partial \theta}\delta(w) + \frac{\partial v}{\partial x}\delta(w)\right] + \dots$$

$$\overline{C_{33}}\left[r\frac{\partial w}{\partial r}\delta\left(\frac{\partial w}{\partial r}\right)\right] + \overline{C_{36}}\left[\frac{\partial u}{\partial \theta}\delta\left(\frac{\partial w}{\partial r}\right) + r\frac{\partial v}{\partial x}\delta\left(\frac{\partial w}{\partial r}\right)\right] + \dots$$

$$\overline{C_{44}}\left[\frac{\partial v}{\partial r}\delta\left(\frac{\partial w}{\partial \theta}\right) - \frac{1}{r}v\delta\left(\frac{\partial w}{\partial \theta}\right) + \frac{1}{r}\frac{\partial w}{\partial \theta}\delta\left(\frac{\partial w}{\partial \theta}\right)\right] + \dots$$

$$\overline{C_{45}}\left[\frac{\partial u}{\partial r}\delta\left(\frac{\partial w}{\partial \theta}\right) + r\frac{\partial v}{\partial r}\delta\left(\frac{\partial w}{\partial x}\right) - v\delta\left(\frac{\partial w}{\partial x}\right) + \frac{\partial w}{\partial x}\delta\left(\frac{\partial w}{\partial \theta}\right) + \frac{\partial w}{\partial \theta}\delta\left(\frac{\partial w}{\partial x}\right)\right] + \dots$$

$$\overline{C_{55}}\left[r\frac{\partial u}{\partial r}\delta\left(\frac{\partial w}{\partial x}\right) + r\frac{\partial w}{\partial x}\delta\left(\frac{\partial w}{\partial x}\right)\right] \} dr d\theta dx$$

(42)

Again using integration by parts to lower the order of the variation and temporarily only considering the first term yields:

$$
\begin{aligned}
&-\int_V \{\overline{C_{12}}\left[-\frac{\partial u}{\partial x}\right]+\overline{C_{13}}\left[r\frac{\partial^2 u}{\partial x\partial r}+\frac{\partial u}{\partial x}\right]+\overline{C_{22}}\left[-\frac{1}{r}w-\frac{1}{r}\frac{\partial v}{\partial \theta}\right]+\dots \\
&\overline{C_{23}}\left[\frac{\partial^2 v}{\partial\theta\partial r}+\frac{\partial w}{\partial r}-\frac{\partial w}{\partial r}\right]+\overline{C_{26}}\left[-\frac{1}{r}\frac{\partial u}{\partial\theta}-\frac{\partial v}{\partial x}\right]+\overline{C_{33}}\left[r\frac{\partial^2 w}{\partial r^2}\right]+\dots \\
&\overline{C_{36}}\left[\frac{\partial^2 u}{\partial\theta\partial r}+r\frac{\partial^2 v}{\partial x\partial r}+\frac{\partial v}{\partial x}\right]+\overline{C_{44}}\left[\frac{\partial^2 v}{\partial r\partial\theta}-\frac{1}{r}\frac{\partial v}{\partial\theta}+\frac{1}{r}\frac{\partial^2 w}{\partial\theta^2}\right]+\dots \\
&\overline{C_{45}}\left[\frac{\partial^2 u}{\partial r\partial\theta}+r\frac{\partial^2 v}{\partial r\partial x}-\frac{\partial v}{\partial x}+\frac{\partial^2 w}{\partial x\partial\theta}+\frac{\partial^2 w}{\partial\theta\partial x}\right]+\dots \\
&\overline{C_{55}}\left[r\frac{\partial^2 u}{\partial r\partial x}+r\frac{\partial^2 w}{\partial x^2}\right]\}\delta w dr d\theta dx
\end{aligned}
\tag{43}
$$

Applying the fundamental lemma of variational calculus and dividing by r:

$$
\begin{aligned}
&\left\{\overline{C_{45}}\left[\frac{\partial^2 v}{\partial r\partial x}-\frac{1}{r}\frac{\partial v}{\partial x}+\frac{1}{r}\frac{\partial^2 w}{\partial\theta\partial x}\right]+\overline{C_{55}}\left[\frac{\partial^2 u}{\partial r\partial x}+\frac{\partial^2 w}{\partial x^2}\right]\right\}+\dots \\
&\left\{\overline{C_{44}}\frac{1}{r}\left[\frac{\partial^2 v}{\partial r\partial\theta}-\frac{1}{r}\frac{\partial v}{\partial\theta}+\frac{1}{r}\frac{\partial^2 w}{\partial\theta^2}\right]+\overline{C_{45}}\frac{1}{r}\left[\frac{\partial^2 w}{\partial x\partial\theta}+\frac{\partial^2 u}{\partial r\partial\theta}\right]\right\}+\dots \\
&-\left\{\overline{C_{12}}\frac{1}{r}\left[\frac{\partial u}{\partial x}\right]+\overline{C_{22}}\frac{1}{r}\left[\frac{1}{r}w+\frac{1}{r}\frac{\partial v}{\partial\theta}\right]+\overline{C_{23}}\frac{1}{r}\left[\frac{\partial w}{\partial r}\right]+\overline{C_{26}}\frac{1}{r}\left[\frac{1}{r}\frac{\partial u}{\partial\theta}+\frac{\partial v}{\partial x}\right]\right\}+\dots \\
&\left\{\overline{C_{13}}\left[\frac{\partial^2 u}{\partial x\partial r}+\frac{1}{r}\frac{\partial u}{\partial x}\right]+\overline{C_{23}}\frac{1}{r}\left[\frac{\partial^2 v}{\partial\theta\partial r}+\frac{\partial w}{\partial r}\right]+\overline{C_{33}}\left[\frac{\partial^2 w}{\partial r^2}\right]+\overline{C_{36}}\left[\frac{1}{r}\frac{\partial^2 u}{\partial\theta\partial r}+\frac{\partial^2 v}{\partial x\partial r}+\frac{1}{r}\frac{\partial v}{\partial x}\right]\right\}=0
\end{aligned}
\tag{44}
$$

Rearranging and grouping terms yields the equilibrium equation in the θ-direction.

$$\begin{aligned}
&\frac{\partial}{\partial x}\left\{\overline{C_{45}}\left[\frac{\partial v}{\partial r}-\frac{1}{r}v+\frac{1}{r}\frac{\partial w}{\partial \theta}\right]+\overline{C_{55}}\left[\frac{\partial u}{\partial r}+\frac{\partial w}{\partial x}\right]\right\}+\ldots\\
&\frac{1}{r}\frac{\partial}{\partial \theta}\left\{\overline{C_{44}}\left[\frac{\partial v}{\partial r}-\frac{1}{r}v+\frac{1}{r}\frac{\partial w}{\partial \theta}\right]+\overline{C_{45}}\left[\frac{\partial w}{\partial x}+\frac{\partial u}{\partial r}\right]\right\}+\ldots\\
&\left\{\overline{C_{13}}\left[\frac{\partial^2 u}{\partial x\partial r}+\frac{1}{r}\frac{\partial u}{\partial x}\right]+\overline{C_{23}}\frac{1}{r}\left[\frac{\partial^2 v}{\partial\theta\partial r}+\frac{\partial w}{\partial r}\right]+\overline{C_{33}}\left[\frac{\partial^2 w}{\partial r^2}\right]+\overline{C_{36}}\left[\frac{1}{r}\frac{\partial^2 u}{\partial\theta\partial r}+\frac{\partial^2 v}{\partial x\partial r}+\frac{1}{r}\frac{\partial v}{\partial x}\right]\right\}+\ldots\\
&-\frac{1}{r}\left\{\overline{C_{12}}\left[\frac{\partial u}{\partial x}\right]+\overline{C_{22}}\left[\frac{1}{r}w+\frac{1}{r}\frac{\partial v}{\partial\theta}\right]+\overline{C_{23}}\left[\frac{\partial w}{\partial r}\right]+\overline{C_{26}}\left[\frac{1}{r}\frac{\partial u}{\partial\theta}+\frac{\partial v}{\partial x}\right]\right\}=0
\end{aligned} \tag{45}$$

The bracketed terms in the equation above correspond to the terms in brackets below and the equilibrium equation in the r-direction is obtained.

$$\frac{\partial}{\partial x}\{\tau_{rx}\}+\frac{1}{r}\frac{\partial}{\partial\theta}\{\tau_{r\theta}\}+\left\{\frac{\partial\sigma_r}{\partial r}+\frac{\sigma_r}{r}\right\}-\frac{1}{r}\{\sigma_\theta\}=0 \tag{46}$$

After again applying gauss's divergence theorem the boundary terms are as follows. Where the Γ is the corresponding surface and the hatted terms are unit vectors normal to the surface.

$$\begin{aligned}
&\int_\Gamma\left\{\overline{C_{45}}\left[\frac{\partial v}{\partial r}-\frac{1}{r}v+\frac{1}{r}\frac{\partial w}{\partial\theta}\right]+\overline{C_{55}}\left[\frac{\partial u}{\partial r}+\frac{\partial w}{\partial x}\right]\right\}n_x r dr d\theta(\delta w)|_\Gamma+\ldots\\
&\int_\Gamma\left\{\overline{C_{44}}\left[\frac{\partial v}{\partial r}-\frac{1}{r}v+\frac{1}{r}\frac{\partial w}{\partial\theta}\right]+\overline{C_{45}}\left[\frac{\partial u}{\partial r}+\frac{\partial w}{\partial x}\right]\right\}n_\theta dr dx(\delta w)|_\Gamma+\ldots\\
&\int_\Gamma\left\{\overline{C_{13}}\left[\frac{\partial u}{\partial x}\right]+\overline{C_{23}}\left[\frac{1}{r}\frac{\partial v}{\partial\theta}+\frac{1}{r}w\right]+\overline{C_{33}}\left[\frac{\partial w}{\partial r}\right]+\overline{C_{36}}\left[\frac{1}{r}\frac{\partial u}{\partial\theta}+\frac{\partial v}{\partial x}\right]\right\}\widehat{n_r r dx d\theta}(\delta w)|_\Gamma=0
\end{aligned} \tag{47}$$

Again the bracketed terms above correspond to the bracketed terms below and the boundary conditions corresponding to the r-direction equilibrium are obtained.

$$\int_\Gamma\{\tau_{xr}\}n_x r dr d\theta(\delta w)|_\Gamma+\int_\Gamma\{\tau_{\theta r}\}n_\theta dr dx(\delta w)|_\Gamma+\int_\Gamma\{\sigma_r\}n_r r dx d\theta(\delta w)|_\Gamma=0 \tag{48}$$

This formulation of the equilibrium equations demonstrates a very mathematically rigorous but systematic approach to develop governing differential equations.

4.2 Axisymmetric Model Reduction

Because the joint geometry is inherently axisymmetric, if the loading is axisymmetric the model size can greatly be reduced. Because typical loading for the joint is in fact axisymmetric the problem will be solved as an axisymmetric case. This constraint of load types reduces the equilibrium equations by eliminating all terms that are derivatives with respect to theta. This reduces the equilibrium equations from the 3D cases to the following set.

$$\frac{\partial \sigma_x}{\partial x} + \frac{\partial \tau_{rx}}{\partial r} + \frac{\tau_{rx}}{r} = 0 \tag{49}$$

$$\frac{\partial \tau_{\theta x}}{\partial x} + \frac{\partial \tau_{r\theta}}{\partial r} + \frac{2\tau_{r\theta}}{r} = 0 \tag{50}$$

$$\frac{\partial \tau_{rx}}{\partial x} + \frac{\partial \sigma_r}{\partial r} + \frac{\sigma_r - \sigma_\theta}{r} = 0 \tag{51}$$

The strain displacement relations are also reduced due to the axisymmetry loading constraint. Like the equilibrium equations the terms in the strain displacement relations that contain derivatives with respect to theta are eliminated. The reduced set of strain displacement relations are defined as follows.

$$\epsilon_x = \frac{\partial u}{\partial x} \tag{52}$$

$$\epsilon_\theta = \frac{w}{r} \tag{53}$$

$$\epsilon_r = \frac{\partial w}{\partial r} \tag{54}$$

$$2\epsilon_{\theta r} = \frac{\partial v}{\partial r} - \frac{v}{r} \tag{55}$$

$$2\epsilon_{xr} = \frac{\partial w}{\partial x} + \frac{\partial u}{\partial r} \tag{56}$$

$$2\epsilon_{x\theta} = \frac{\partial v}{\partial x} \tag{57}$$

Now that the equations to be solved and the corresponding boundary conditions have been found that allow for the application of different loading conditions, a solution method must be defined. Due to the number of equations to be solved simultaneously it is not realistic to obtain an analytical solution. Instead the problem will be cast into a finite element form and a displacement field will be determined by solving the resulting linear set of equations.

4.3 Axisymmetric Finite Element Model

Now knowing that the strain energy density functional contains the equilibrium equations in all three directions with the corresponding boundary conditions, using the finite element form of the Rayleigh-Ritz Method the problem can be solved. Going back to the constitutive relation in Eq. (3) the strain energy density function can be written in the following form. The summation is done over the number of elements.

$$W = \sum_{k=1}^{Nels} 2\pi \int_A \left[\frac{1}{2} \{\epsilon\}^T \left[\bar{C}\right] \{\epsilon\} - \{\epsilon\}^T \left[\bar{C}\right] \{\epsilon_0\} \right] r dx dr \tag{58}$$

The second term that is now present is to include thermal strains. The thermal strains are defined as follows.

$$\epsilon_0 = \begin{Bmatrix} \alpha_x \\ \alpha_\theta \\ \alpha_r \\ 0 \\ 0 \\ \alpha_{x\theta} \end{Bmatrix} \Delta T \tag{59}$$

In order for the displacement field to be defined over the entire domain the displacements at the nodes must be interpolated to get values between the nodes. The unknown displacements are approximated by the following definitions.

$$u = \sum_{j=1}^{npe} u_j N_j$$
$$v = \sum_{j=1}^{npe} v_j N_j \tag{60}$$
$$w = \sum_{j=1}^{npe} w_j N_j$$

In order to define the strain displacement relations in matrix form the following operator is introduced.

$$[\partial] = \begin{bmatrix} \frac{\partial}{\partial x} & 0 & 0 \\ 0 & 0 & \frac{1}{r} \\ 0 & 0 & \frac{\partial}{\partial r} \\ 0 & \frac{\partial}{\partial r} - \frac{1}{r} & 0 \\ \frac{\partial}{\partial r} & 0 & \frac{\partial}{\partial x} \\ 0 & \frac{\partial}{\partial x} & 0 \end{bmatrix} \tag{61}$$

Also placing the interpolation functions in matrix form,

$$[N] = \sum_{i=1}^{npe} \begin{bmatrix} [N_i] & [0] & [0] \\ [0] & [N_i] & [0] \\ [0] & [0] & [N_i] \end{bmatrix} \tag{62}$$

where the degrees of freedom are organized in the following way.

$$\{d\} = \sum_{i=1}^{npe} \begin{Bmatrix} u_i \\ v_i \\ w_i \end{Bmatrix} \tag{63}$$

Using the defined operator and the shape function matrix the strain displacement relationship can be expressed as follows:

$$\{\epsilon\} = [\partial][N]\{d\} = [B]\{d\} \tag{64}$$

Substituting the above definition into the strain energy density expression the following form is obtained.

$$W = \sum_{k=1}^{Nels} 2\pi \int_A \left[\frac{1}{2} \{d\}_j^T [B]^T \left[\bar{C}\right][B]\{d\}_j - \{d\}_j^T [B]^T \left[\bar{C}\right]\{\epsilon_0\} \right] r dx dr \tag{65}$$

Because the displacement vector only contains nodal values the integration can be moved inside. Inserting the following definitions:

$$[k]_j = 2\pi \int_A [B]^T \left[\bar{C}\right][B] r dx dr \tag{66}$$

$$\{r_T\}_j = 2\pi \int_A [B]^T \left[\bar{C}\right]\{\epsilon_0\} r dx dr \tag{67}$$

The strain energy density function becomes:

$$W = \sum_{k=1}^{Nels} \left[\frac{1}{2} \{d\}_j^T [k]_j \{d\}_j - \{d\}_j^T \{r_T\}_j \right] \tag{68}$$

Now to solve the problem the strain energy density function must be made stationary across every element. Therefore:

$$\frac{dW}{d\{d\}} = 0 \tag{69}$$

resulting in the familiar finite element form shown below with the right had side currently only containing the thermal loading terms.

$$\sum_{k=1}^{Nels} [k]_j \{d\}_j = \sum_{k=1}^{Nels} \{r_T\}_j \tag{70}$$

In order to apply the boundary terms that are seen in Eq. (34), Eq. (41), and Eq. (48) another load vector must be introduced into the finite element formulation. Because the finite element model discretizes the problem the loads also need to be discretized. The boundary terms developed in

the variational formulation can all be described as surface tractions and point loads. Therefore given the following equations for the finite element model the problem can be solved with the corresponding boundary terms included.

$$\{r_B\}_j = \int_\Gamma [N]^T \{\Phi\}\, dS \tag{71}$$

The integration is over the surface of the configuration and dS are the infinitesimal surface area along the boundary. Adding these loading terms to Eq. (70) the finite element formulation is complete.

$$\sum_{k=1}^{Nels} [k]_j \{d\}_j = \sum_{k=1}^{Nels} \{r_T\}_j + \sum_{k=1}^{Nels} \{r_B\}_j \tag{72}$$

The shape functions are repeated here for convenience and are the same as used by Cook et al. [31]. The standard node numbering scheme is used for both the 4-node linear elements and the 8-node quadratic elements. The natural coordinates are in terms of ξ and η for each element. For the 4-node linear element the shape functions are defined as follows.

$$N_1 = \frac{1}{4}(1-\xi)(1-\eta) \tag{73}$$

$$N_2 = \frac{1}{4}(1+\xi)(1-\eta) \tag{74}$$

$$N_3 = \frac{1}{4}(1+\xi)(1+\eta) \tag{75}$$

$$N_4 = \frac{1}{4}(1-\xi)(1+\eta) \tag{76}$$

For the 8-node quadratic element, the shape functions are expanded and are as follows.

$$N_1 = \frac{1}{4}(1-\xi)(1-\eta) - \frac{1}{2}(N_8 + N_5) \tag{77}$$

$$N_2 = \frac{1}{4}(1+\xi)(1-\eta) - \frac{1}{2}(N_5 + N_6) \tag{78}$$

$$N_3 = \frac{1}{4}(1+\xi)(1+\eta) - \frac{1}{2}(N_6 + N_7) \tag{79}$$

$$N_4 = \frac{1}{4}(1-\xi)(1+\eta) - \frac{1}{2}(N_7 + N_8) \tag{80}$$

$$N_5 = \frac{1}{2}(1-\xi^2)(1-\eta) \tag{81}$$

$$N_6 = \frac{1}{2}(1-\eta^2)(1+\xi) \tag{82}$$

$$N_7 = \frac{1}{2}(1-\xi^2)(1+\eta) \tag{83}$$

$$N_8 = \frac{1}{2}(1-\eta^2)(1-\xi) \tag{84}$$

Within the thermal loading terms and the stiffness terms there are derivatives of the shape functions with respect to the global coordinates x, and r. These derivatives are found using the chain rule and can be expressed in the following form relating the derivatives with respect to the natural coordinates to the global coordinates.

$$\begin{Bmatrix} \frac{\partial N_i}{\partial \xi} \\ \frac{\partial N_i}{\partial \eta} \end{Bmatrix} = \begin{bmatrix} \frac{\partial x}{\partial \xi} & \frac{\partial r}{\partial \xi} \\ \frac{\partial x}{\partial \eta} & \frac{\partial r}{\partial \eta} \end{bmatrix} \begin{Bmatrix} \frac{\partial N_i}{\partial x} \\ \frac{\partial N_i}{\partial r} \end{Bmatrix} \tag{85}$$

The matrix is known as the Jacobian matrix. Using shape functions to approximate the global coordinates within elements the Jacobian can be expressed as follows.

$$x = \sum_{i=1}^{npe} x_i N_i \tag{86}$$

$$r = \sum_{i=1}^{npe} r_i N_i \tag{87}$$

$$[J]=\begin{bmatrix}\sum_{i=1}^{n} x_i \frac{\partial N_i}{\partial \xi} & \sum_{i=1}^{n} r_i \frac{\partial N_i}{\partial \xi} \\ \sum_{i=1}^{n} x_i \frac{\partial N_i}{\partial \eta} & \sum_{i=1}^{n} r_i \frac{\partial N_i}{\partial \eta}\end{bmatrix} \tag{88}$$

In order to get the derivatives we are looking to determine in the thermal loading and stiffness terms, we need the inverse relationship of Eq. (85). Therefore, the determinate of the Jacobian matrix is what is used. The area integrals in the stiffness terms and load terms can now be written in the following form.

$$[k]_j = 2\pi \int\int_{-1}^{1} f(\xi,\eta) J d\xi d\eta \tag{89}$$

$$[r_T]_j = 2\pi \int\int_{-1}^{1} f(\xi,\eta) J d\xi d\eta \tag{90}$$

where the determinate of the Jacobian matrix is J .

In order to compute these integrals a numerical approach must be chosen to accommodate generality. Gauss quadrature has been proven as an efficient and accurate method of numerical integration and will be used here. Gauss quadrature is a weighted sum approach. The function is sampled at various locations with corresponding weights and summed together to approximate the integral. The integrals can then be written in the following form.

$$[k]_j = 2\pi \int\int_{-1}^{1} f(\xi,\eta) J d\xi\eta = 2\pi \sum_{m=1}^{ngp}\sum_{n=1}^{ngp} W_m W_n f(\xi,\eta) J \tag{91}$$

$$[r_T]_j = 2\pi \iint_{-1}^{1} f(\xi,\eta) J d\xi\eta = 2\pi \sum_{m=1}^{ngp}\sum_{n=1}^{ngp} W_m W_n f(\xi,\eta) J \tag{92}$$

where ngp is the order of the quadrature being used, W_m and W_n are the weights, and J again is the determinate of the Jacobian.

4.4 Finite Element Program

In order to use the finite element method to solve an axisymmetric joint problem a computer program was developed originally by Paul Lyon [1] and Michael Lambert [2]. Aid in

debugging as well as making the computer programs more user friendly was included in the current work. Also the ability to model an insert joint configuration was added to the programs capability in the current work. Two main tasks must be completed in order to apply the finite element model developed in the previous sections of this chapter to the analysis of cylindrical adhesive joints. First the geometry must be input and meshed. Second the stiffness matrix must be formed along with the application of the specified loads in order to solve for the unknown displacements. For an axisymmetric case these two tasks are completed via two programs, "Axisymmetric Mesh program.exe" and "fecode.exe". These two codes apply the finite element algorithm and do all of the actual computation. "Mesh Generator v-2.exe" serves as the graphical user interface (GUI) and allows the user to specify the input and call the two before mentioned programs.

4.4.1 Finite Element Program Capabilities

The program was written to analyze cylindrical adhesive joints. Because most of the common load cases are axisymmetric the program can mesh and solve axisymmetric as well as 3D cases. The program has the capability of simulating three different general geometries as well as several different load cases all of which can be ran separately or combined and ran in an assortment of different combinations.

The three general geometries are the typical cylindrical adhesive joint, a cylindrical adhesive insert joint, and a single cylinder. The two joint type geometries are pictured in Figure 2. along with dimensions and the dimension labels used in the GUI. The insert joint configuration can only be modeled as an axisymmetric case. Dimensions for the three cases can all be specified using the GUI. The option to include and internal taper is available in the axisymmetric case.

The program allows for several different mechanical load types. The most basic is the application of a point load. The user can specify the node the load acts, the magnitude, and the direction of the load. The program also has the capability to handle distributed loads. The

consistent nodal load approach is used to determine the loads necessary at the nodes to approximate the distributed load. The program will find the right and left edge of the geometry and allow a distributed load to be applied perpendicular to the joints edge. This load can either be a compressive load or a tensile load by making the magnitude negative or positive respectively. In much the same way a torque load can also be applied to either edge of the joint. The consistent nodal loading technique is also used to model an internal and external pressure. Again the program will locate the inner or outer surface of the joint and apply the appropriate loads to mimic the acting pressure. The program can also incorporate a uniform temperature load by computing equivalent thermal loads using Eq. (67). Bending loads can also be applied but only if a 3D case is being ran due to the fact that bending is not an axisymmetric load case. Bending can either be applied via a line load across the top of the joint or a distributed load.

In order to remove rigid body motion from the solution constraints must be applied. The program allows constraints to be added in two ways. A single point constraint can be added by specifying the node and the degree of freedom to be constrained. The program also allows for the entire left or right edge of the joint to be constrained in any of the three degrees of freedom and any possible combination of the three.

The model also has the capability to model composite laminates. The option is easily selected using the GUI. There are also several different analysis options. Cases can either be run with constant material properties or material properties as a function of temperature. The ability to run several different composite layups in order to produce plots to aid in the optimization of a given quantity through composite layups is also available. Adaptive mesh refinement can also be applied in order to refine the mesh in order to ensure the displacements have been resolved. For more information concerning the algorithm used for mesh refinement refer to Paul Lyon’s thesis [1].

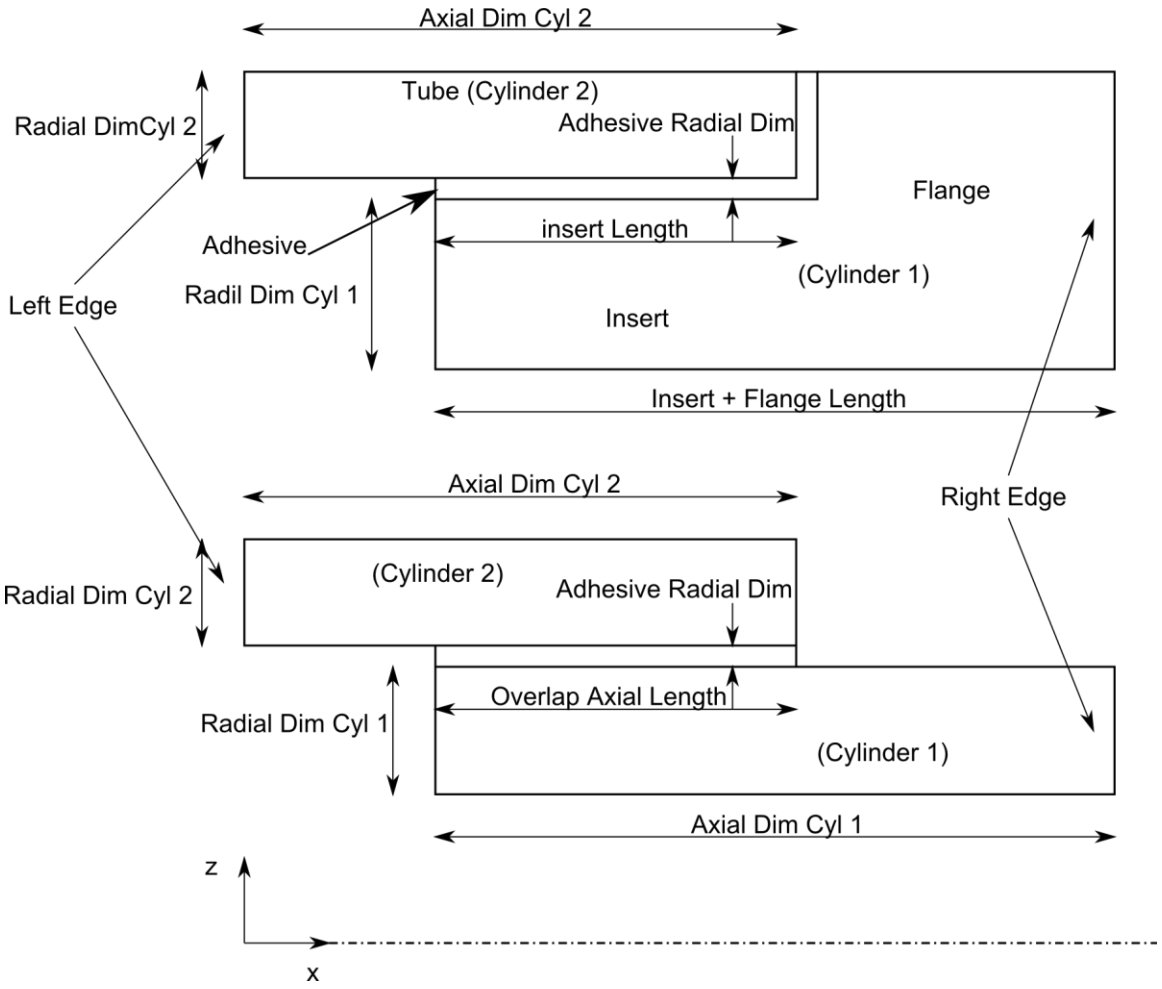

Figure 2. General configurations the code can model along with dimension labels seen in the GUI. Typical adhesive joint (Top), Adhesive insert joint (Bottom).

4.4.2 FORTRAN Meshing Programs

There are two separate FORTRAN programs to mesh axisymmetric and 3D models. "Axisymmetric Mesh program.exe" builds a mesh for an axisymmetric model of either a regular joint or an insert joint. For this program to run, a text file titled "2D Mesh input.txt" containing user specified element type, geometry, and several load cases must be present within the same directory. Files containing boundary condition data, both force and displacement must also be present within the directory, these files are titled "Right BC data.txt" and "Left BC data.txt". The option to include single point constraints and point loads is also available in the program. These

inputs are stored in files titled “Point Loads.txt” and “Single Point Constraints.txt”. All of the input files described above are automatically generated by the GUI program “Mesh Generator v-2.exe”. Explanation of the input files are discussed here only to allow the user more knowledge in checking input to ensure correctness.

After the input is successfully read in the program assembles the connectivity matrix. This matrix stores the global node number as well as the global coordinate for each node. The displacement and forced boundary conditions are then applied. Forces that are applied over an area are applied using the consistent nodal loading approach. If an internal taper of the inner cylinder is desired it is applied in this program.

Just before termination of the program three output files are written for the user to review while the fourth will be used by “fecode.exe” to import the generated mesh data. The text file titled “2D Boundary Condition data.txt” contains the global nodes with either displacement constraints or loads. The degrees of freedom that the constraints act, along with the prescribed value are presented. The text file titled “2D Mesh Results.txt” contains the connectivity matrix, the global coordinates of each node and the material region that each element belongs to. The final file output for review is a .vtk file titled “Visualized mesh.vtk”. This file is viewed in VisIt and provides a visualization of the produced mesh. This file is particularly useful in quickly being able to ensure the mesh that has been created is what was expected. The text file titled “Stiff Input.txt” is not organized for the user to review and is for the finite element solver program “fecode.exe” to import the mesh data produced by the meshing program.

The program titled “3D Mesh Generator.exe” follows the same basic procedure that is covered above for the axisymmetric case but a third dimension is assigned. For this reason it is not covered in detail here. For a more in depth coverage of both of these programs refer to reference [1] and [2].

4.4.3 FORTRAN Finite Element Solver

Only one FORTRAN code is needed to solve both axisymmetric and 3D cases. The program titled “fecode.exe” imports the data generated by the meshing programs using the “Stiff Input.txt” file. The program solves for the unknown displacements at the nodes and also performs post processing. The independent material properties for the different material zones specified in the mesh data are input via the file titled “Material Properties.txt”. Both isotropic and anisotropic materials are compatible with the program. For isotropic materials many of the constants do not apply and are left blank in the file.

After the independent material properties are read in Stiffness and compliance matrices are calculated along with off-axis coefficients of thermal expansion (CTEs). Stiffness values can then be computed for each element. Element stiffness values are computed in the manner which is described in Section 4.3 Eq. (66). Gauss quadrature is used to perform the integration numerically. The individual element stiffness values are then compiled in one matrix, known as the global stiffness matrix. The individual element load vector is also computed in the manner which is described in Section 4.3 Eq. (67). Gauss quadrature again is used to perform the integration numerically. Again these individual element loads are compiled in a vector, known as the global load vector.

From the various input files created by the GUI and meshing programs the boundary conditions are applied. The point loads and distributed loads now turned into nodal load values using the consistent nodal load approach by the meshing programs are added to the global load vector.

In order to speed up the solution process the fact that the global stiffness matrix is sparse, banded, and symmetric is taken advantage of. The skyline storage technique used also minimizes the amount of zeros stored in the global stiffness matrix. The unknown displacements are then solved for using a modified Choleski decomposition algorithm. The developed algorithms were

based on the algorithms developed by Smith and Griffiths [32-34]. The result is a vector containing the unknown nodal displacements.

After determining the displacements the stresses and strains can be calculated. The strains and stresses are calculated at the gauss points and extrapolated out to the nodes. The gauss points have been shown to be the super accurate locations for stress and strain within the element. The nodal values are then averaged within material regions. Stresses are not averaged across dissimilar material interfaces. These values are then written to their respective output files at each node.

Visualization is done using the freeware VisIt. Files with the extension .vtk are written containing the global coordinates of each node, the connectivity matrix, type of element, and the value of the displacement at each node. A mesh of the configuration as well as contour and criteria plots can be generated and viewed.

4.4.4 Visual Basic GUI

In order to make running the FORTRAN programs easier, a visual basic GUI was created. The GUI is titled “Mesh Generator v-2.exe” and the main program window is shown in Figure 3 The program allows the user to input the geometry and meshing specifications as well as input boundary conditions, single point constraints, load cases, material properties, and analysis options. All of the required input files talked about in the two previous sections are generated automatically and placed in the correct directory. To call the mesh generator programs hit the “Generate Mesh” button. To analyze the created mesh the FE code is called by pressing the “Analyze” button.

When the “Input Material Properties” button is hit the window in Figure 4 will appear. Input the independent properties for each material region starting from the inside most region of the joint to the outside leaving columns blank if the property doesn’t apply to the material region.

When the “Input Material Properties” button is hit in the popup window the window will be dismissed and the properties will be written to the correct .txt input file.

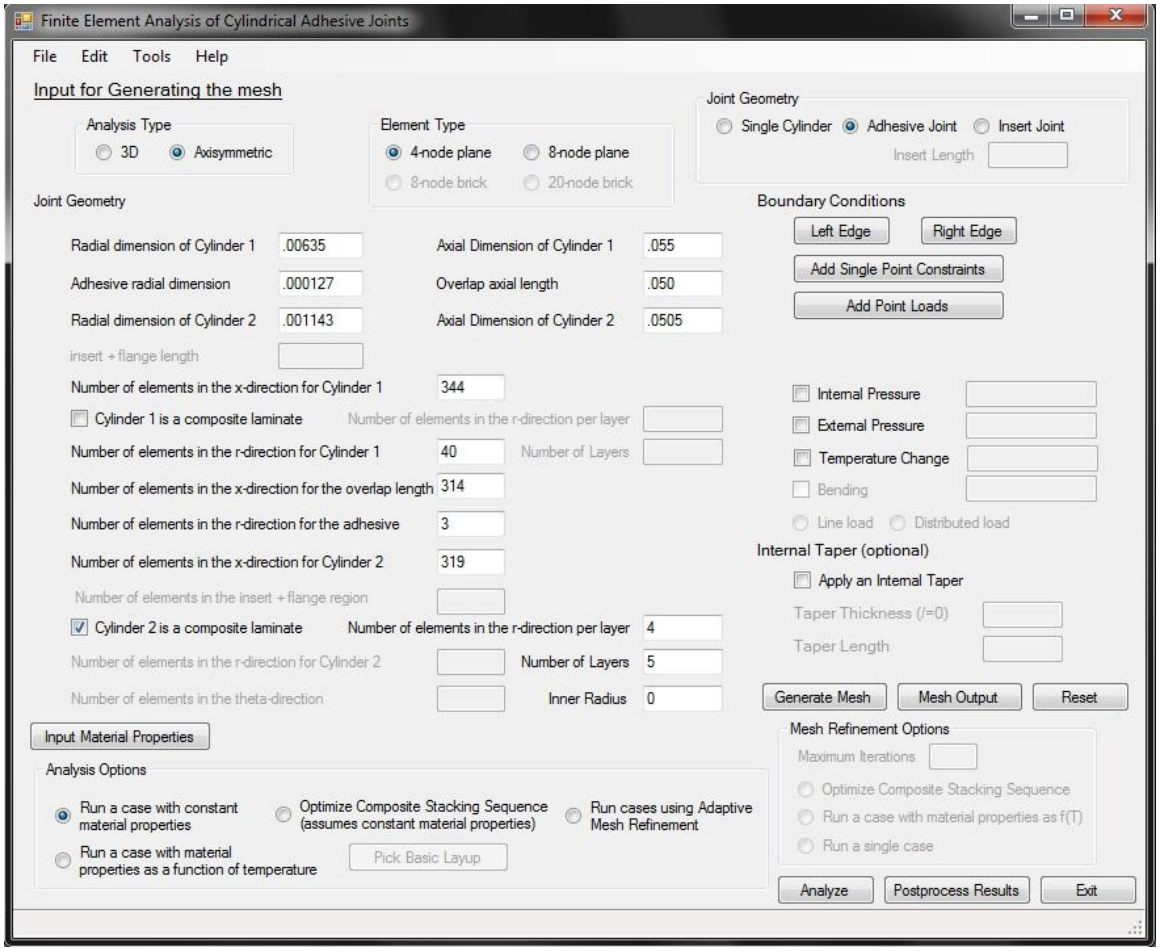

Figure 3. Mesh Generator v-2 front panel.

When the “Left Edge” or “Right Edge” button is hit the respective window shown in Figure 5 will appear. To fix a degree of freedom along the respective edge just check the box under the corresponding direction. To apply a uniform load or torque to the edge check the box and the text box will become active allowing a magnitude to be input. The direction of the load is perpendicular to the surface. When the “Apply BC’s” button is pressed the window will be dismissed and the corresponding .txt file will be generated.

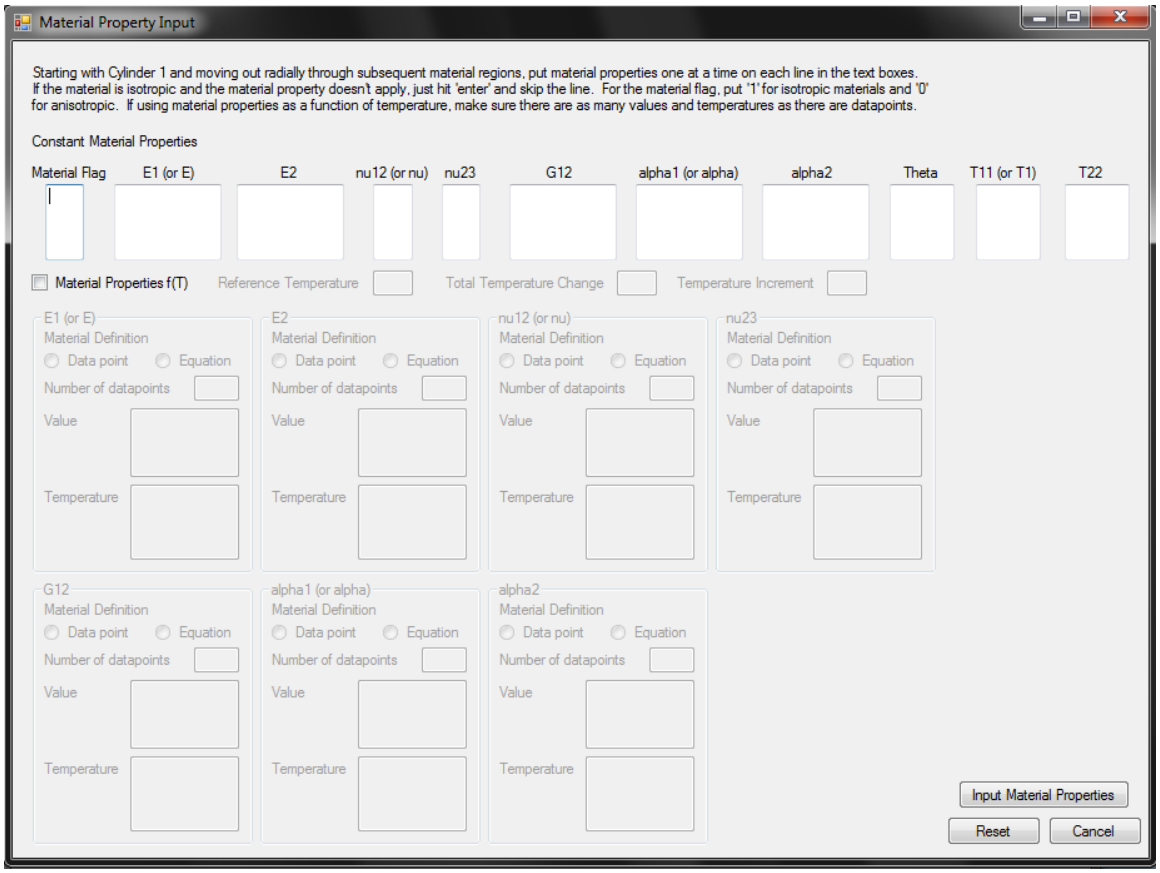

Figure 4. Mesh Generator v-2 Material Property Input popup window.

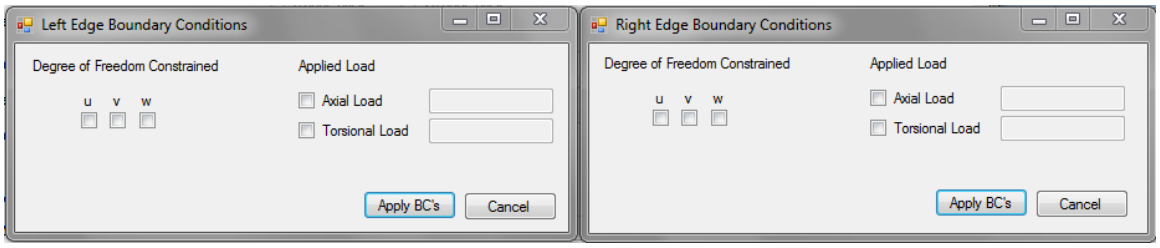

Figure 5. Mesh Generator v-2 Edge boundary condition input.

The process to specify single point constraints and point loads is the same. When the "Add Single Point Constraints" or "Add Point Load" button is pressed the corresponding window will appear, and are shown in Figure 6 The number of constraints or load must be specified as well as the Node ID, Degree of Freedom for the constraint or load to act in, and the Constrained

or load value. When the “Apply Constraint” or “Apply Load” button is pressed the window will be dismissed and the corresponding .txt file will be written.

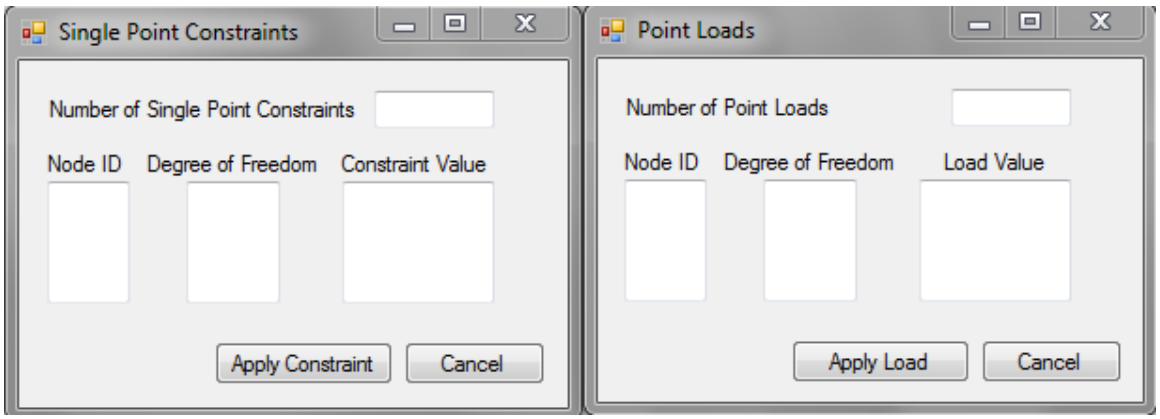

Figure 6. Mesh Generator v-2 Left: single point constraint and Right: point load input.

In order to run a case to optimize composite stacking sequence another input window is encountered. The user must specify the amount of 0° and 90° layers and their location. The + and – terms are varied from 0° to 90° in order to determine the best layup for a given criteria. It is critical to ensure that the number of layers in the specified layup matches with the mesh and material property input.

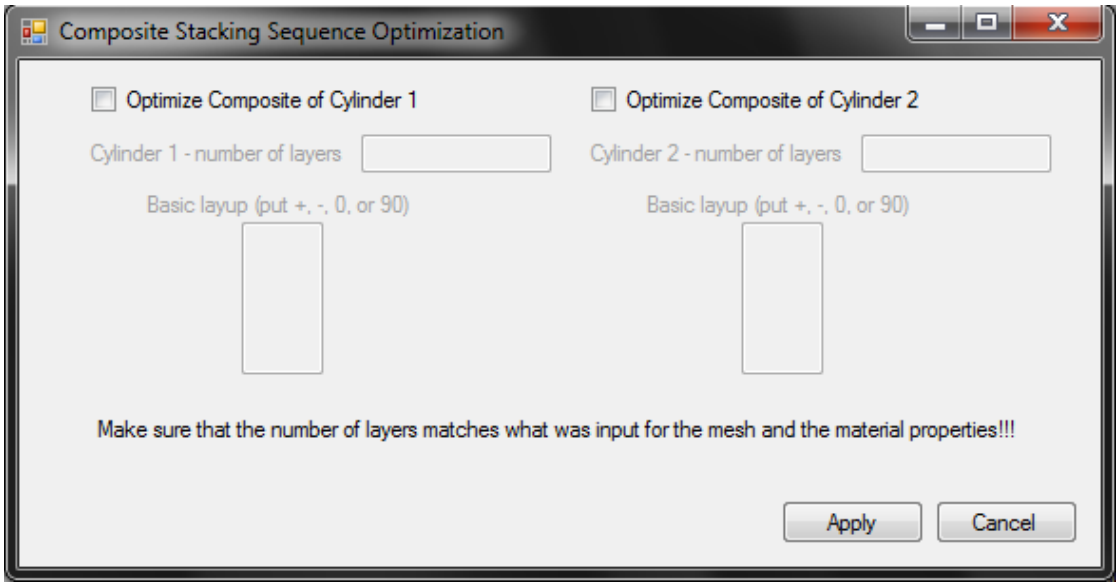

Figure 7. Mesh Generator v-2 Composite Stacking Sequence Optimization input.

4.5 Conclusions

In conclusion the solution to an axisymmetric problem is obtained. The equilibrium equations and corresponding natural boundary conditions are derived using a variational approach. Verifying that the equilibrium equations match those that are derived using a Newtonian method shows that the correct variational statement was used. The problem is then cast into finite element form using the finite element form of Raleigh-Ritz to obtain the corresponding displacement field. One interesting thing that was noted when verifying the model is that due to the orthotropic nature of the laminate there are deflections in the r and θ-direction even if all of the loading occurs in the x-direction. An axisymmetric assumption does not imply that all θ-displacements are zero. This is the case for isotropic materials but not for orthotropic laminates.

CHAPTER 5

MATERIAL AND EQUIPMENT SELECTION

5.1 Unidirectional Carbon Fiber

Carbon fiber composite has been used extensively in the aerospace field due to its light weight and high strength. As was presented in Chapter 2 much of the research that has been performed on composites is for space application and consequently how the composite behaves at cryogenic temperatures. It has been found to have the capability to withstand the harsh environment as long as cracking effects are taken into account in the design of the structure. These characteristics have driven the desire to research bonding carbon fiber composite members to other commonly used materials in aerospace structures.

5.1.1 Composite Selection

Due to the high cost of carbon fiber composite materials the selection of the carbon fiber to be used was driven by what was already available at the University. Alliant Aerospace Company was generous enough to donate large amounts of Unidirectional Prepreg Carbon Fiber rolls. The materials were manufactured by Hexcel and are a Graphite Fiber/Epoxy material, Type III, IM7G/1915.

5.1.2 Initial Material Property Estimates

In order to have an initial estimate of the material properties to be input into the finite element program Hexcel was kind enough to provide the certification test results performed at the time of manufacture. The prepreg physical and mechanical properties are all normalized to 50% fiber volume in the report and may need to be scaled for the actual volume fraction achieved in the curing process. Properties are only given for the fiber direction because matrix properties are dependent on the cure cycle used. For an initial estimate of the matrix properties, data was taken

from Chapter 2 of Stress Analysis of Fiber-Reinforced Composite Materials Table 2.1 for graphite-polymer composite [35].

5.2 Aluminum

As with carbon fiber, aluminum is a common material used in aerospace structures. A common aluminum alloy was chosen due to its availability and low cost. 6061 aluminum rod is a material that has undergone extensive material research due to its widespread use and therefore material properties were easily attained. In order to verify the measurement systems used, an aluminum sample was tested to ensure that the calculated Young's modulus was similar to published results. The Poisson ratio was taken as given but the Young's modulus was determined via the measured data. A detailed explanation of the process followed is presented in Chapter 6 Section 6.

5.3 Epoxies for Use at Cryogenic Temperatures

When designing adhesive joints for use a cryogenic temperature, one of the major components is the adhesive to be used to join the aluminum and composite sleeve. Unlike many other applications, there are several issues with your typical adhesive that must be considered when purchasing an adhesive for this type of application. The main ones that have been determined and were considered when coming up with the following adhesives to be compared and verified here were as follows; ability to remain ductile at cryogenic temperatures, as well as r strength retention in an extremely cold environment, the ability to withstand the initial thermal shock, and the adhesive must meet the low out-gassing standard set by NASA, because these joints are to be used in space. These unique issues are discussed and the candidates for use in the testing phase are presented and compared.

5.3.1 Ductility and Strength considerations

Not unlike other engineering grade materials adhesives in general tend to become brittle, and as a consequence, significantly less strong at low temperatures. When a material becomes brittle, failure occurs abruptly and without warning, especially when an impact or dynamic loading condition is experienced. Also brittle materials tend to be less strong under tensile loading then under compressive loading. Because these joints are to be used as truss/structure members, both tensile and compressive forces are to be experienced. Therefore, strength is necessary under both loading conditions.

5.3.2 Initial Thermal Shock Consideration

One of the toughest tests that the adhesive has to endure is the initial thermal shock that will be experienced when first entering the cryogenic environment. When joining two dissimilar materials, as is the case in our aluminum composite sleeve joint design, mismatches in coefficients of thermal expansion becomes a major issue. Because the aluminum and graphite reinforced composite want to shrink or grow different amounts due to the change in temperature the adhesive may be sheared. If careful consideration is not taken, the mismatch in CTE will cause the adhesive to fail simply due to the thermal loading and the structure will lose all integrity. While the adhesive cannot handle a huge mismatch in CTE an exact match in CTE is unrealistic and therefore the adhesive must be able to withstand a shearing load. Design of the graphite reinforced composite takes into account the need to match as closely as possible the CTE of the aluminum while meeting other requirements.

5.3.3 Out-gassing Consideration

Out-gassing is a phenomenon that occurs in many manufactured materials but becomes much more prevalent in the vacuum of space. Out-gassing is the release of a gas, from in this specific case, the adhesive. This can either be gas that was trapped or absorbed, and escapes through cracks, or sublimation of the adhesive itself. This is an issue because these gasses can

interfere with other components of the structure and can prevent them from performing their task. Worst case scenario, out-gassing can completely render certain components useless. The parameters used to quantify how well an adhesive performs in retaining its mass in a vacuum is Maximum Total Mass Lost (%TML) and Collected Volatile Condensable Materials (%CVCM). In order for the adhesive to be a candidate for use in space %TML must be less than one percent and %CVCM must be less than one tenth of a percent. A few examples of where out-gassing can become a problem is when the gas condenses on optical lenses, thermal radiators, solar cells, etc. causing them to not perform up to their specification.

5.3.4 Case Study of Commercially Available Adhesives

To make an informed decision a case study was performed. The case study aimed at objectively comparing the three chosen adhesives. The most important characteristics that the adhesive must illustrate were given a rating, allowing for an informed decision to be made.

As is seen within the case study the 3M and Masterbond adhesive have been researched more extensively by the manufacturers for cryogenic applications. The Franklin Urethane repair kit was considered due previous research indicating it may be an inexpensive candidate for applications such as ours.

5.3.5 Final Selection and Material Properties

After careful consideration of the case study presented the most cost effective choice without sacrificing performance was the 3M 2216 gray. Additional confidence in the selected adhesive has been realized as further research was performed and it was found that the adhesive has performed in the field as it is used by Lockheed Martin Space Systems. Also extensive testing has been performed to determine the material properties of 3M 2216 gray at Lockheed Martin Space Systems Advanced Technology Center. The results are presented in a paper titled *Optomechanical Epoxy Adhesive* by Mark T. Sullivan and are presented in Table 2.

Table 1. Adhesive Case Study

KEY	Acceptable	Questionable/untested	Not known

Distributor	Product	Shear Strength (psi)	Published material properties	Thermal Shock Resistance	Outgassing Specification	Cost
3M	3M 2216 GRAY	2740 @ -196°C	Yes	Yes, tested	%TML = .77 %CVCM = .04 Meets NASA standard	Approx. $200 per quart
Franklin Adhesives and Polymers	Urethane Repair Kit	Data Not Available	NO	Claims to resist freezing temps	Data Not Available	
Masterbond	EP29LPSP	>2200 at 24°C	Yes	Yes, Claimed in TDS	%TML = ? %CVCM = ? TDS – meets NASA Standard	

Table 2. Material Properties for 3M Scotchweld 2216 B/A Gray

Property	Symbol	Units	Epoxy, 3M Scotch-Weld 2216 B/A Gray
Density	ρ	Kg/m^3	1550
Thermal conductivity	k	W/m-°C	0.4
Coefficient of thermal expansion	α	10^{-6}/°C	102
Specific heat	c	KJ/Kg-°C	1.884
Resistivity	ρ_{res}	μohm-m	1.9E+16
Dielectric Strength		Volts/mil	408
Modulus of elasticity	E	GPa	0.7
Modulus of rigidity	G	GPa	0.2
Poisson's ratio	ν		0.43
Ultimate Tensile Strength	S_{ut}	MPa	34.5
Shear Strength (125 μm bond line)	S_s	MPa	22.0
Mix Ratio (weight)			5:7
Working Time	t_w	Minutes	90
Time to Handling Strength	t_h	Hours	12
Full Cure Time (@24 °C)	t_{FC}	Days	7
Hardness		Shore D	50 - 65
Outgassing	TML	%	0.77
	CVCM	%	0.04
Shelf Life		Years	2

5.4 Extensometer

In order to measure the displacement of the joint, an averaging extensometer was needed to bridge the joint area. Strain gauges are to measure strain at a specific location but not to measure a displacement at a given gauge length. Averaging extensometers enable the measurement of a displacement between two points at a distance apart depending on the gauge

length of the device. Extensometers are an application of strain gauges arranged in a Wheatstone bridge. They allow displacement to be measured, not only between to specific points, but also without the extra time that comes with strain gauge application on each of the test samples.

Two major companies were found that offered axial extensometers, Epsilon Technology Corp. and Instron. Both offered configurations that would work well in measuring displacement of the joint region. The designs were similar in that they both included knife edges to allow easy mounting and removal, making testing of multiple samples quick and easy.

Differences came in that the Instron model incorporated two axial sensors that are averaged to provide a single output of strain. This configuration minimizes the errors due to specimen bending. Epsilon offered a setup that was specifically rated as a low temperature configuration and is fully temperature compensated. Instron didn't advertise a temperature compensated model but most high end sensors incorporate a full bridge which in turn are temperature compensated.

Because Instron manufactures a wide range of testing equipment, the extensometers were built to interface with Instron's own data acquisition equipment. Epsilon Technology Corp. allows their sensors to be interfaced with any electronics designed for strain gauge transducers. Because it is desirable to have all of the data acquisition done with on device simultaneously the Epsilon gauge was chosen, allowing for the use of pre-existing data acquisition boards.

Model 3542-025M-010-LT option was chosen. The model has a 25 millimeter (0.984252 in) gauge length with ±2.5 millimeters (0.098425 in) of travel (±10% of gauge length). The low temperature option was also chosen to allow testing to be performed at cryogenic temperatures. The tolerated temperature range is from -265°C to 100°C (-450°F to 210°F).

5.5 Analog Input Device

The NI analog input device used in the configuration presented in Chapter 6 was already available at the university and was deemed to be sufficient. It interfaces with a computer via

USB. The Ni USB-6210 Bus-Powered M Series Device was used to interface with both the extensometer and load cell simultaneously.

CHAPTER 6

DATA ACQUISITION CONFIGURATION AND VERIFICATION

6.1 Extensometer and Load Data Acquisition System Introduction

Because both the load and extensometer bridges are supplied voltage from an outside source, the DAQ needs to have a differential setting, something not offered by an all-in-one system like the NI 9237 bridge completion device. The NI 9237 is designed to supply the excitation voltage as well as complete the bridge if needed. A data acquisition system capable of recording both the output of the load cell on the tensile test machine and the output of the extensometer was needed. The hardware used in the setup consisted of a NI USB-6210 16bit multifunctional I/O device, an Epsilon Extensometer, the load cell on the Tinius Olsen tensile test machine, and an instrumentation amplifier. Also Included were instrumentation wiring and a laptop computer with National Instruments LabVIEW Version 10 (64 bit) software.

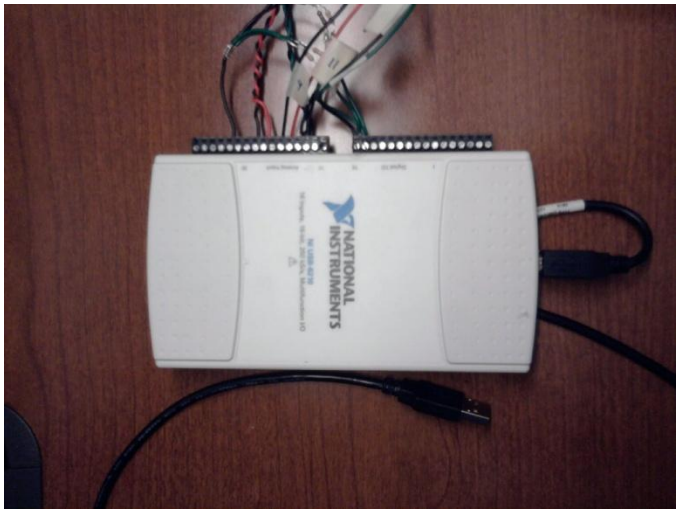

Figure 8. NI USB-6210 multifunctional I/O device

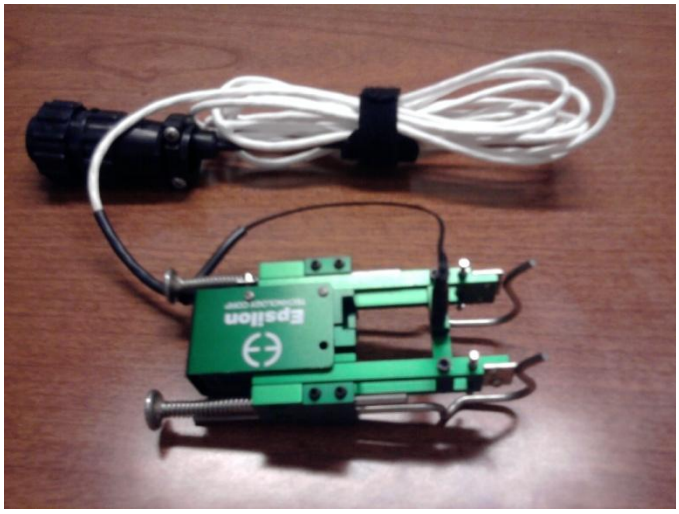

Figure 9. Epsilon 3542-025M-010-LT Extensometer

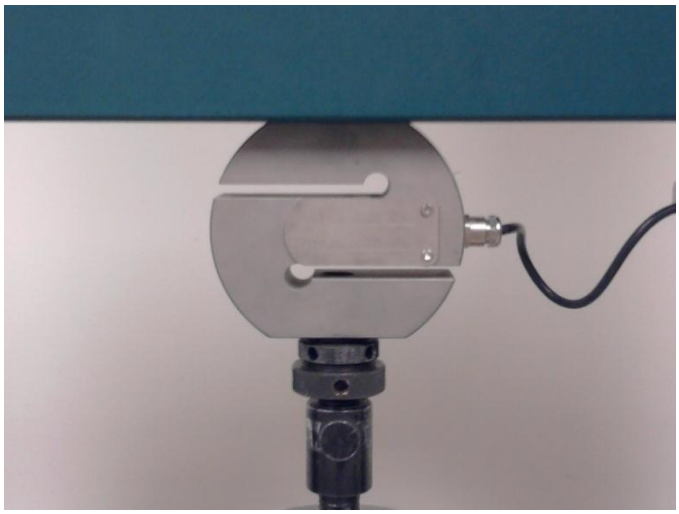

Figure 10. Tinius Olsen 50KN (11240lbf) load cell

Figure 11. Instrumentation Amplifier

6.2 Instrumentation Amplifier

Although the Wheatstone bridge built into the extensometer amplifies the output of the strain gauges within the extensometer, the noise level of the NI USB-6210 was on the same level as the output of the extensometer at the beginning of the test. Only a fraction of the 2.5 mm (0.098425 in) travel is used in a tensile test meaning only a fraction of the output is signal range is used. For this reason an instrumentation amplifier was built.

When considering building an instrumentation amplifier it is important that the amplifier itself does not introduce more noise into the signal. First thing to consider was the amplifier itself. There are many different instrumentation amplifiers on the market, and in order to ensure the amplifier that was chosen had been proven, other labs at Utah State University were checked to see what configurations had worked well in the past. Dr. Smith had a proven setup that was used in the Experimental Fluid Dynamics Laboratory for pressure sensors. Pressure sensors are also based on a full Wheatstone bridge and therefore the setup was used as a reference.

There are three main components in an instrumentation amplifier, an amplifier chip, a power supply, and a voltage regulator. A low drift, low power instrumentation amplifier (AD621) made by Analog Devices was chosen due to its simplicity and performance. The package

purchased is in an 8-pin Plastic DIP configuration. A temperature range of -40°C to +85°C (-40°F to 185°F) is acceptable. The chip has two set gains either 10 or 100. The gain is set through pin strapping. The noise specification for the amp was found to be much lower than that seen on the output of most Wheatstone bridge devices and was therefore acceptable.

The AD621 power supply range is wide and can be anywhere from ±2.3V to ±18V. A power supply could now be chosen to power the amp. The main specification that is desirable when looking for a power supply for use in an instrumentation amplifier set up is it must produce stable, flat (low ripple) DC voltage. Unregulated power supplies output vary depending on load as well as changes in the AC input. Linear power supplies are preferred for sensitive electronic applications such as this because they set the output voltage to a precise value, independent of the load and input changes. Linear power supplies are also much cleaner in that the ripple and noise is much less when compared with unregulated supplies. A SOLA/HEVI-DUTY power supply was chosen. The exact model used is a SLD-12-1010-12T. These power supplies are specifically designed for use in noise sensitive applications. The Ripple specification on the output is 3.0 nV maximum peak-to-peak. The input power to the supply is a standard 120V 60Hz AC. The ±12V voltage level was chosen to make the amplifier usable for signals of larger amplitude in the future as this input power acts as an upper and lower limit to the amplification.

One characteristic of every power supply is that the voltage level must be measured relative to a specific location and this location can change. This is commonly referred to as a floating supply, implying that the negative and positive pin will always be in this case 24V apart but the actual voltage levels could be 10V and 34V. For this reason the bridge must also be supplied voltage by the same supply that supplies the power to the amplifier. This led to a change in the DAQ board used to acquire the displacement data. Originally a 24 bit NI 9237 DAQ was chosen for the application due to the higher bit resolution but because it was designed to power the bridge, the 16 bit USB-6210 DAQ had to be used. The NI 9237 is a bridge completion device designed to supply the bridge excitation voltage, as well as sense the output, and therefore does

not allow the use of different reference locations, or a pin to share reference. An effort was made to allow for the use of the NI 9237 but the introduction of two separate reference levels (grounds) allowed for ground loops causing the output to oscillate between the two grounds and wiping out the output signal. The USB-6210 allows the use of a differential setting allowing the device to read the output of the bridge without knowing the supply reference level. The loss in resolution going from the 24 bit DAQ to the 16bit DAQ is no problem now that the output can be amplified to ensure the least significant bit (LSB) is not an issue.

In order to ensure that the supplied excitation to the bridge device was stable an extra precaution was taken and an LM7808c positive voltage regulator was installed to regulate the power to approximately 8V. This voltage regulator ensures that if the power supply wandered within the .05% for 50% load regulation specification the bridge would still be supplied with an ultra stable excitation voltage, guarding against changes in calibration slope of the output over a long test due to changing excitation voltage.

The components described above come together to make an instrumentation amplifier as shown in Figure 12. Also shown in the figure is a connection scheme to reduce noise. If the bias resistors were not present the noise that couples electro-statically onto the positive line would not couple with the negative line because the negative line would be directly connected to ground. Having the bias resistors balances the signal paths making the noise appear as common mode noise, which is rejected by the PGIA instead of showing up as a differential mode noise. The disadvantage of this configuration is it loads down the source producing a slight gain error. This gain error does not matter because the calibration will also be taken with this configuration removing the error.

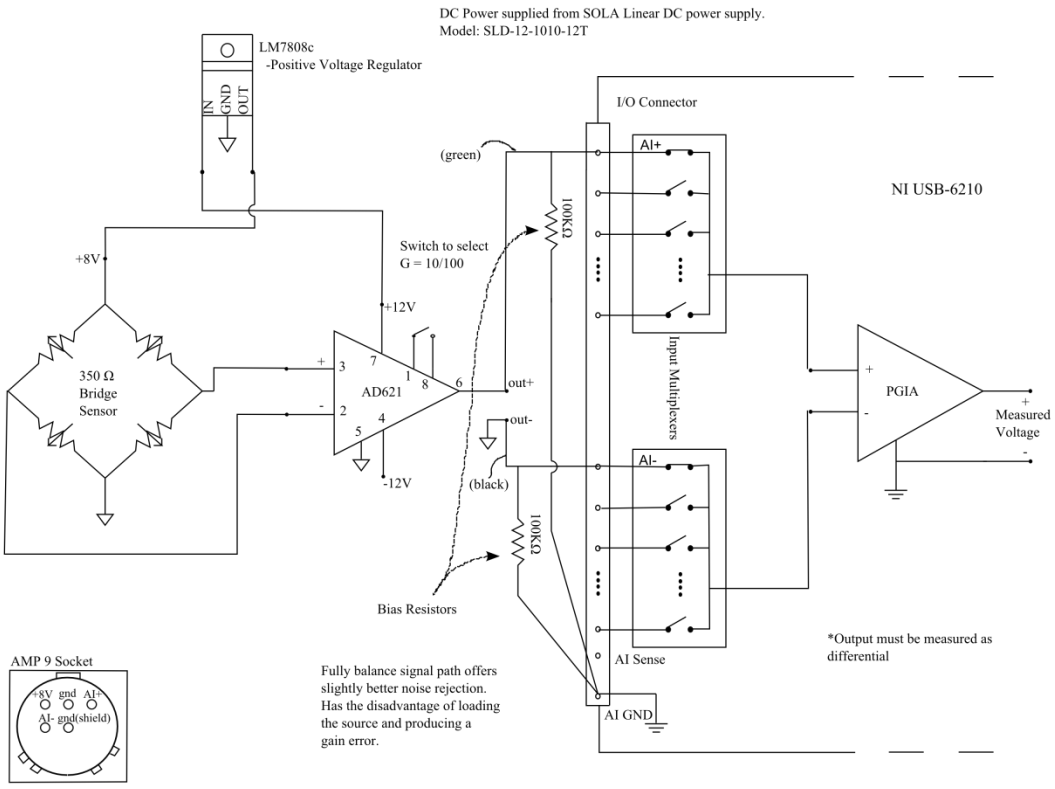

Figure 12. Instrumentation Amplifier Schematic hooked up to NI USB-6210.

6.3 Data Acquisition Software

Again the National Instrument software LabVIEW 10.0 was used to interface with the NI USB-6210. The VI records and displays the output of the load cell, load cell excitation, the extensometer output signal, as well as the extensometer excitation. The scanning order is ordered from small signals to large signals as is recommended in the NI USB-6210 user manual. This minimizes the chances of ghosting of the larger signals onto the more sensitive output signals. The averages of the last 100 samples are then displayed in the indicators on the right hand side of the VI. The terminal configuration for all four of the monitored samples was differential, meaning the difference between the positive and negative terminal is reported. The VI also allows for the location that the output files will be written to as well as the filename. The data written to the

output files is raw voltage data presented in columns in the same order the channels are scanned. The first column is the time in seconds that the test was run.

The raw data written to the output file is then imported into MATLAB. The MATLAB script allows for raw calibration data to be read in and a calibration slope is then calculated for both the load cell and extensometer. A plot is created with the data points and the resulting line fit for the user to review. Next the load and displacement data are read in from the file output from LabVIEW. In order to eliminate the white noise associated with the signal being read in, some basic filtering is performed. Every 100 points are averaged yielding a data point every fifth of a second. After the data has been filtered the output is nondimensionalized by dividing the output signal by the excitation voltage of the respective bridge. This is another safeguard against changing excitation voltages over a long test. The calibration obtained previously is then used to convert the raw voltage data to displacement, and load data. Knowing the gauge length of the extensometer, strain is then easily calculated. Stress can also be calculated in the aluminum by dividing the load by the aluminum area. The area used to calculate the stress value is of the cross section of the half inch aluminum rod and was used in the verification process in the next section. The program then fits a line to the force vs. displacement plot to determine a stiffness value. A lower and upper value is set to specify what portion of the curve is taken into account in the line fit. A line is also fit to the stress versus strain data in the same way allowing a Young's modulus to be calculated.

6.4 Extensometer Calibration Procedure and Associated Uncertainty

In order to ensure the test environment and calibration environment were identical calibration was pursued. The set up that was used to perform the calibration was a Schaevitz calibrating stand. The stand consists of a vernier micrometer mounted on a fixture that allows the axial extensometer to be attached and exercised. The stand with the extensometer in the calibrating position is shown in Figure 13.

Figure 13. Schaevitz calibration stand.

Because some of the errors that contribute uncertainty to the slope of the calibration curve are non-obvious, the direct approach was used in determining the uncertainty of the calibration slope. It was also found that because of play in the zero pin of the axial extensometer, initially a measurement must be taken to determine the position of the extensometer when no strain is induced. The displacement is then the difference between the initial and final value multiplied by the calibration slope. The axial extensometer is pictured in Figure 14. The zero pin is the pin seen holding the arms of the extensometer in a set position and is removed when readings are taken. This has implication in the uncertainty analysis because now the intercept uncertainty does not play into the overall uncertainty of the displacement measurement due to the correlation effect. In order to characterize the uncertainty the standard deviation of the slope, b, is found for the independent calibrations.

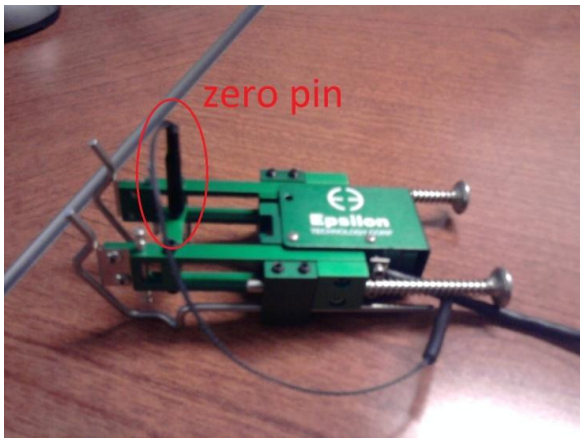

Figure 14. Axial extensometer with zero pin circled.

$$\left(s_b\right)_{direct} = \left[\frac{1}{M-1}\sum_{i=1}^{M}(b_i - \bar{b})^2\right]^{\frac{1}{2}} \tag{93}$$

where there are M independent determinations of the result and:

$$\bar{b} = \frac{1}{M}\sum_{i=1}^{M} b_i \,. \tag{94}$$

The sample standard deviation of the mean can then be calculated using the result of Eq. (93) as:

$$\left(s_{\bar{b}}\right)_{direct} = \frac{\left(s_b\right)_{direct}}{\sqrt{M}} \,. \tag{95}$$

Now to perform the uncertainty analysis directly the calibration was run three times independent of one another on different days to ensure all effects were taken into account. The results are shown below in Figure 15.

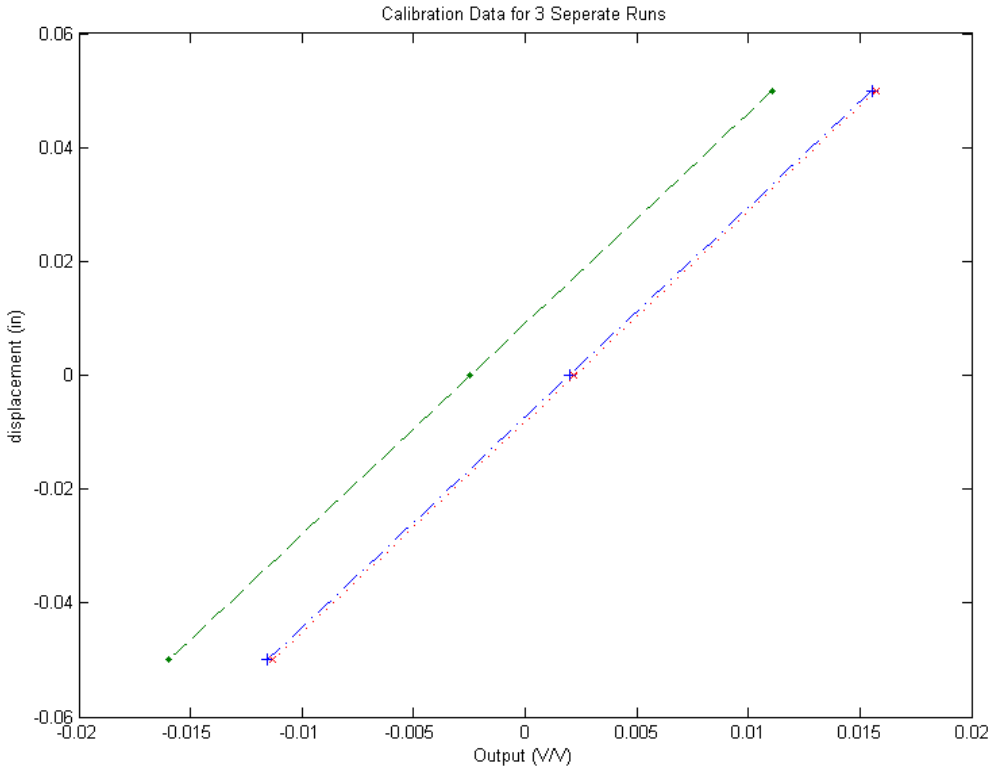

Figure 15. Calibration data for three separate runs.

The line fits for the three runs are also displayed in Figure 15. The play in the zero pin of the extensometer can really be seen in the figure showing up in the bias term of the linear fits. The slope terms found in the curve fits in Figure 15 were ran through Eq. (93-95) and the uncertainty on the slope was determined.

$$\bar{b} = 3.695497558221190 \text{ in.} \tag{96}$$

$$u_{\bar{b}} = 4.303\left(s_{\bar{b}}\right)_{direct} = 0.0058725 \text{ in.} \tag{97}$$

6.5 Load Cell Calibration Procedure and Associated Uncertainty

Although the load cell output voltage was read directly from the cell, the only means to calibrate the load cell was using the readout on the machine which used the previous Tinius Olson

calibration. For this reason the uncertainty published for the Tinius Olson calibration must be used. Due to this all of the random uncertainties are now considered as systematic uncertainties because they are now fossilized. The term fossilized means that uncertainties that were originally random, now have to be considered systematic because more samples cannot be taken. The values that are provided in the documentation are a resolution of 1/32000 of the nominal value and an accuracy of ±1%. The nominal value of the load cell is 50KN which equates to 11240.5lbf. Therefore, the standard systematic uncertainties for the load measurement are as follows.

$$2b_{res} = \frac{1}{2}\frac{1}{32000}11240.5\text{lbf} \rightarrow b_{res} = .08782\text{lbf} \tag{98}$$

$$2b_{acc} = .01P\text{lbf} \rightarrow b_{acc} = .005P\text{lbf} \tag{99}$$

Using the Taylor Series Method (TSM) the standard uncertainty of the load measurement , P, becomes:

$$u_P = \sqrt{b_{res}^2 + b_{acc}^2} = \sqrt{(.08782)^2 + (.005P)^2}\,lbf \tag{100}$$

6.6 Data Acquisition Setup Verification

In order to verify that the displacement and load measurements taken were repeatable and reasonable, a tensile test was performed. A 12.7 mm (.5 in.) diameter aluminum rod sample was used as the reference material in the tensile test. Because aluminum is used so often in structural application the Young's modulus is well known and published data is used as a reference. A reasonable Young's modulus should be around 68.9 GPa (10 Msi). The measured data will be used to compute a measured Young's modulus and compared to the expected value. To ensure repeatability, the sample will not be tested to failure but to a value much lower, well within the elastic region, so that the same sample can be tested several times and compared.

Initial test runs showed that there were problems somewhere in the setup causing the test to not repeat when performed seconds apart. After combing over the data acquisition setup and

software for errors, the tests were ran again only to yield the results shown in Figure 17. The different extensometer placements referenced in the legend of Figure 17 are shown in Figure 16.

Figure 16. Extensometer placement on sample, Left: front; Middle: side; Right: back.

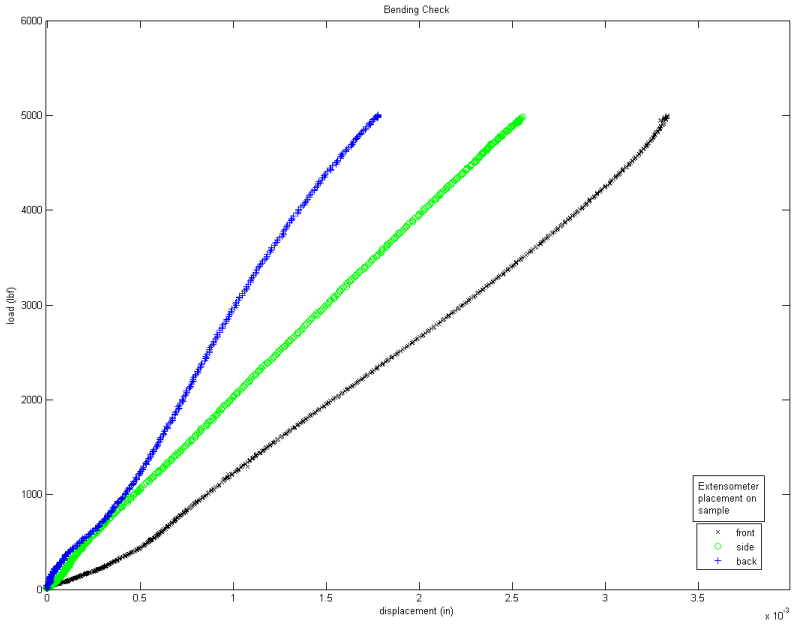

Figure 17. Force vs. Displacement results when changing the placement of the extensometer on the reference sample.

This made it evident that the reference sample was not experiencing a uniform state of tensile stress. Knowing this, the tensile test machine setup was checked for any introduction of eccentricities in the loading. Two problems were found. The first issue was that the sample was being pushed to the back of the grip to ensure alignment. Because the grip is 30mm(1.181102 in.)

wide the specimen was not centered on the grip face. The load path of the machine goes through the center of the grip face and as is evident in Figure 18 a large eccentricity was present.

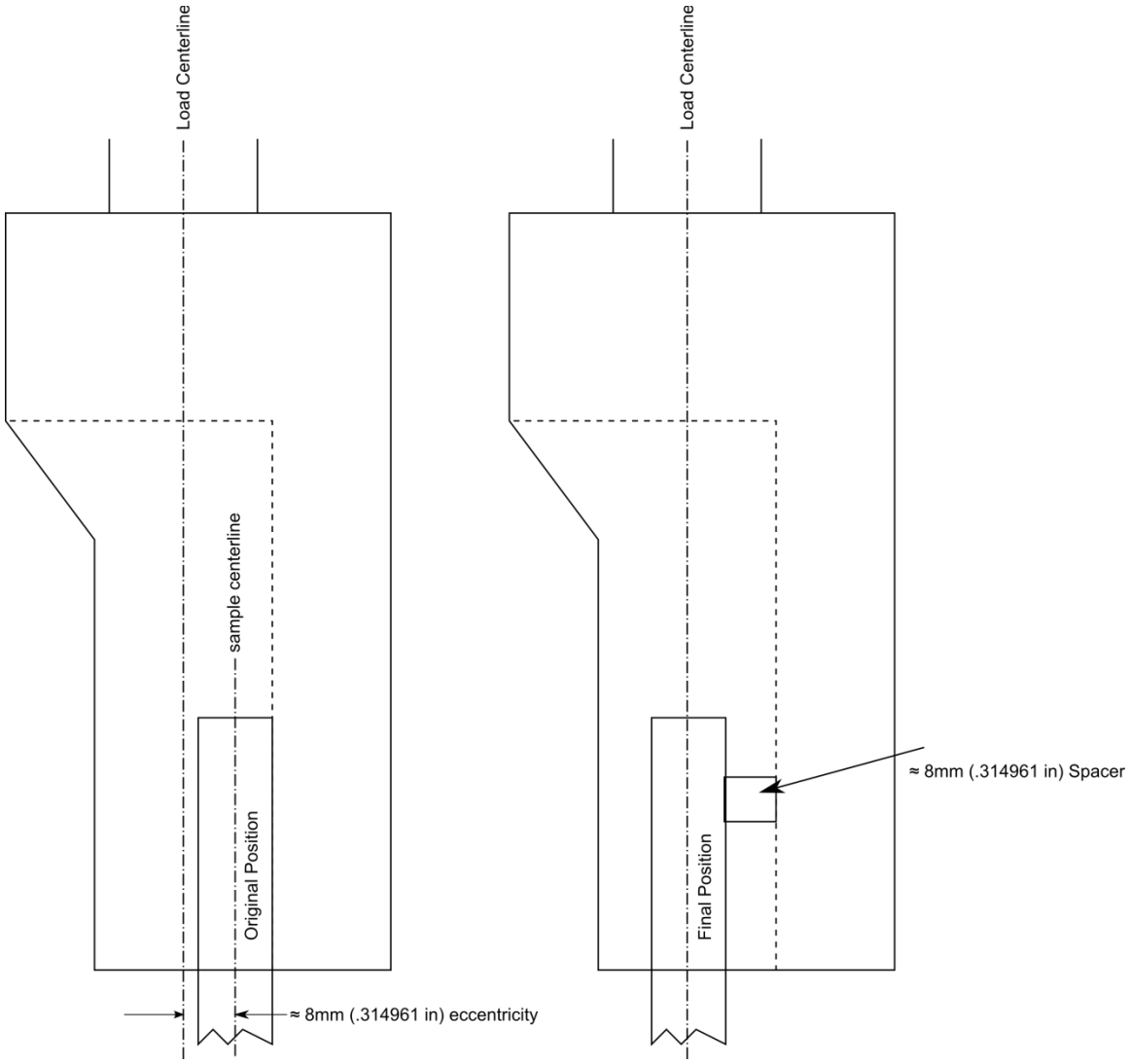

Figure 18. Tensile grips side views, Left: Original reference specimen placement in tensile grips Right: Final placement with spacers.

With the addition of the spacers, the centerline of the specimen is in line with the center line of the load.

The second issue was made evident after the introduction of the spacers. When the reference specimen was pressed all the way against the spacer in the top and bottom grip, it was not vertical. This meant that either the entire tensile tester load frame was bent or the grips

themselves were bent. To check the load frame the grips were removed and the mounting points for the grips were brought together to check alignment. The alignment is shown in Figure 19.

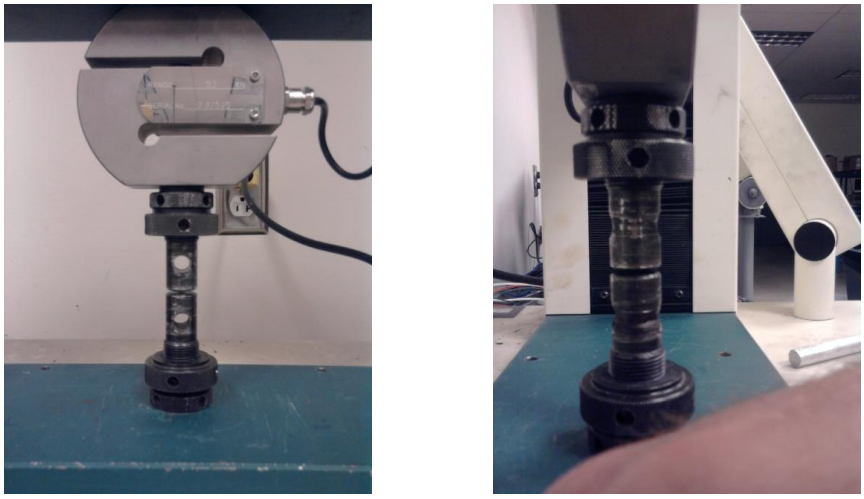

Figure 19. Load frame alignment, Left: Front view Right: Side view.

The load frame was found to be in alignment and that left the grips to be checked. The grips were reinstalled and brought together to check alignment. The alignment is shown in Figure 20.

Figure 20. Side view of the tensile grips originally.

This check made it obvious that one or both of the grips were bent. There was about a 4mm eccentricity being introduced, again causing the test to not repeat. The grips were again removed

and brought to Terry Zollinger, the department machinist, and he was able to straighten them. The new alignment is shown in Figure 21.

Figure 21. Side view of grip alignment after straightening.

Now having fixed a few setup problems the reference sample was tested again at several different placements to ensure the bending had been removed. The test results now only show slight variations in the measured displacements as the extensometer is moved from the neutral axis, confirming that the eccentricities have nearly been removed. The variations will be less in actual test runs as the extensometer will be placed at the neutral axis to ensure the most accurate result, minimizing the effect the small amount of bending present will play. The results after the spacing and straightening are shown in Figure 22.

After it was ensured that the test was repeatable, the test was ran ten times back to back. The data was compiled and using the calibrations a Stress vs. Strain curve was produced. A linear fit was performed on the data in order to determine the measured Young's modulus of the

aluminum reference sample. The measured Young's modulus (the slope of the linear fit) was found to be 67 GPa (9.7Msi). The percent difference from the measured data and the published data was calculated as 3% well within typical material variability from sample to sample. Therefore the testing setup was deemed verified.

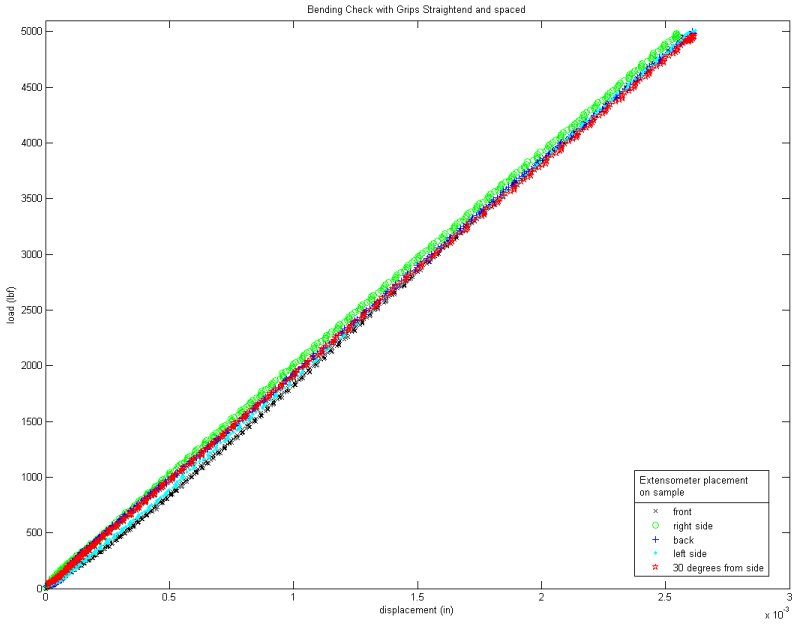

Figure 22. Force vs. Displacement results when changing the placement of the extensometer on the reference sample after spacing and straightening.

CHAPTER 7

SAMPLE PREPARATION

In order to verify the finite element model, samples with precise, consistent, geometry needed to be manufactured. Several different attempts were made to create joint samples with controlled consistent geometry. Each repetition of the process something was learned, and the final method at creating consistent joints to obtain test data is presented here.

7.1 Aluminum Preparation

In order to ensure the removal of any foreign material on the bonding surface of the aluminum rods to be joined with the composite sleeve, first the surface was scored with a fine 220 grit sand paper. In order to ensure a consistent abrasion pattern, the palm sander shown in Figure 23 was used.

Figure 23. Palm sander used to obtain a consistent abrasion pattern.

The sand paper was changed frequently to ensure each of the samples was subjected to the same amount of abrasion. This not only promotes superior bonding due to the increased surface area, but also removes oxidation and ensures a clean aluminum surface. Directly after the sanding process, the samples were wiped clean using a clean cloth and isopropyl alcohol. The samples were then submerged in AC 130, a surface etchant manufactured by Advanced Chemistry

Technology (AC Tech), for the time allotted in the supplied instructions. This product was recommended by NASA Marshal Space Flight Center and is a high performance surface preparation, designed to promote enhanced adhesion for bonding of aluminum alloys. The samples were then hung in order for excess etchant to drip away, as well as to avoid contaminating the prepared surface by coming in contact with unclean surfaces. The process was done in subsequent steps for each sample to avoid any oxidation build up to occur after the initial removal. The aluminum was then bonded shortly after the allotted time needed to allow the surface prep to cure to minimize chance for contamination.

Figure 24. Prepared samples being hung to allow removal of excess etchant as well as to avoid contamination due to contact with unclean surfaces.

7.2 Composite Sleeve Manufacture

In order to layup the composite sleeve, a mandrel is needed to wrap the unidirectional prepreg on. A highly straight 12.7 mm (.5 in.) steel rod was purchased to use as a mandrel. To ensure that the prepreg did not bond to the mandrel a .127 mm (.005 in.) thick piece of mylar was applied to the mandrel. The prepreg is then ready to be wrapped on the mandrel to produce a composite sleeve. In order to wrap angled plies that have continuous fibers, the approach pictured in Figure 25 was used.

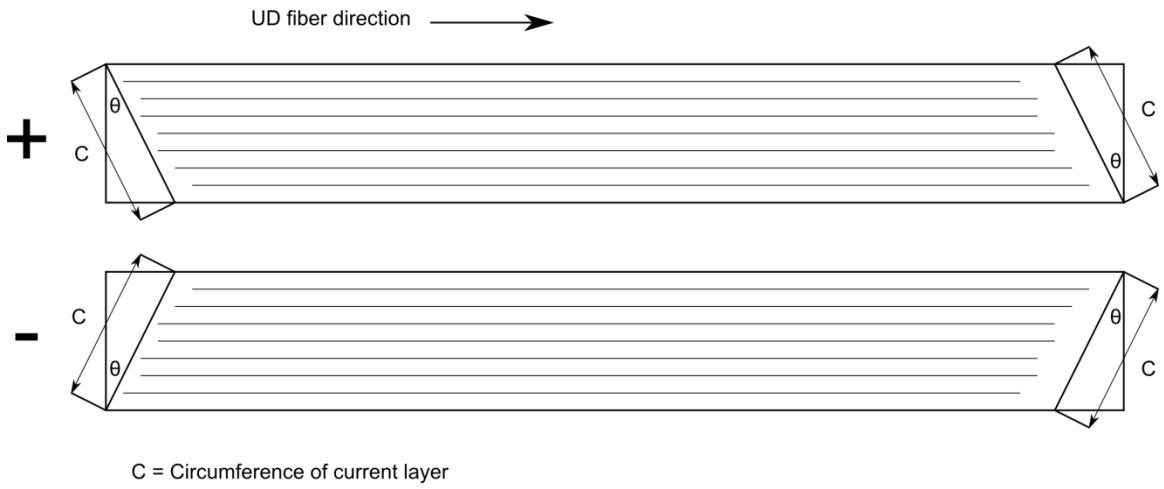

Figure 25. Layout of angle ply prepreg to be wound on mandrel.

The ply was then spiraled around the mandrel and an angled ply with continuous fibers is achieved. After each layer, the circumference of the sleeve was measured and needs to match the dimension labeled, C, in Figure 25. The process is repeated until the desired composite layup is completed. After the last ply has been applied, the sleeve is wrapped in heat shrink tape that has been perforated. This puts pressure on the sleeve in the cure cycle to promote a good fiber volume fraction by squeezing out excess resin.

7.3 3M 2216 Gray Preparation

The adhesive was mixed by weight as per instruction on the can. All other preparations were complete upon the final mixing to ensure the adhesive was applied well within the prescribed pot life. Before each application the adhesive was stirred to ensure a good working life.

7.4 Joint Sample Assembly and Cleanup

The uncured composite is first cut to the desired length. After cutting the composite it was placed back into the freezer to ensure the resin in the composite returns to the non-sticky A stage. This also aids in allowing the composite sleeve to slide easily onto the aluminum rods to be joined. While the sleeves are being chilled the adhesive is mixed. The adhesive is then applied

liberally to the inside of the composite sleeve as well as the aluminum rods. The aluminum rod is then inserted at one end slowly twisting and plunging the rod in and out to ensure adequate adhesive coating of all surfaces. Once both of the rods are inserted slight pressure was applied to both ends causing the excess adhesive to flow out from between the end of the two rods and out the ends. To ensure the rods have been completely inserted measurements were taken before and after to assure no gap is left between the two. Excess adhesive is then wiped from the edges, leaving enough around the edge of the composite to ensure no voids are created at the edges. The joints are then placed in the oven at 90°C (194°F) for an hour to allow the adhesive to become partially cured. This prevents the adhesive from being completely squeezed out by the pressure put on the composite by the heat shrink tape. After the first hour the composite cure cycle was initiated. When removed from the oven the joints look like Figure 26. The gripping length of the samples differs from joint to joint but the overlap length remains the same. Figure 27 shows the excess resin that was removed from the composite and allowed to escape through the perforated heat shrink tape.

Figure 26. Joint samples directly after being removed from oven.

Figure 27. Excess resin removed from the composite and allowed to escape through the perforated heat shrink tape.

The shrink tape is then peeled off, and the excess adhesive around the edge of the composite sleeve is removed. The final joint samples for testing are shown in Figure 28.

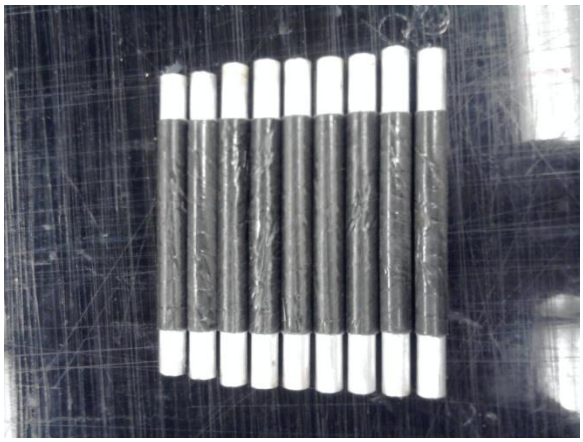

Figure 28. The completed joint samples.

7.5 Resulting Joint Geometry

The resulting joint geometry after the joints had been cured and cleaned up was measured. This geometry was used in the finite element model. The top geometry in Figure 2 gives explanation of the nomenclature. The measurements are presented in Table 3.

Table 3. Resulting Sample Geometry Measurements and Number of Elements Used

	Meters (m)	Inches (in)	# of elements
Radial dim CYL 1	0.00635	0.25	40
Adhesive radial dim	0.000127	0.005	3
Radial dim CYL 2	0.001143	0.045	20
Axial dim CYL 1	0.0550	2.16535	344
Overlap axial dim	0.0500	1.968504	314
Axial dim CYL 2	0.0505	1.988189	319

CHAPTER 8

JOINT STIFFNESS TESTING AT ROOM TEMPERATURE

Room temperature tensile testing was done first to show that the finite element method could capture effects of tensile loading on the joint geometry. The initial material property estimates discussed in Chapter 5 were for room temperature, making the initial verification simpler if done at room temperature. An in depth uncertainty analysis of the measured stiffness was done. After running the test, it was found that the uncertainty introduced by the test setup was insignificant when compared to the sample to sample variations.

8.1 Experimental Setup

In order to check the displacements solved for using the finite element model, force and displacement data was taken. This data was acquired using the setup outlined and verified in Chapter 6. The joints presented in Chapter 7 were placed into the tensile testing machine. Dimensions of the joints constituent parts were taken before the joints were made to allow for the center of the joint to be located. Marks were then made 25 mm (0.984252 in.) apart, which is the gauge length of the extensometer, straddling the center. The knife blade of the extensometer was then placed on the marks. The samples were then loaded at a constant rate of 2.54 mm (.1 in.) per minute, a common rate used in composites testing. The samples were loaded up to 13345 N (3000 lbf), well within the joints elastic limit. This allowed each joint to be tested more than once, again to ensure the measurement could be repeated. This repeatability ensures that the loading of the joint is within the elastic limit, therefore not causing local failure, which in turn would alter the joints stiffness. Displacement and load data were taken simultaneously allowing for a force vs. displacement plot to be created. The joint in the tensile testing machine with extensometer placed can be seen in Figure 29.

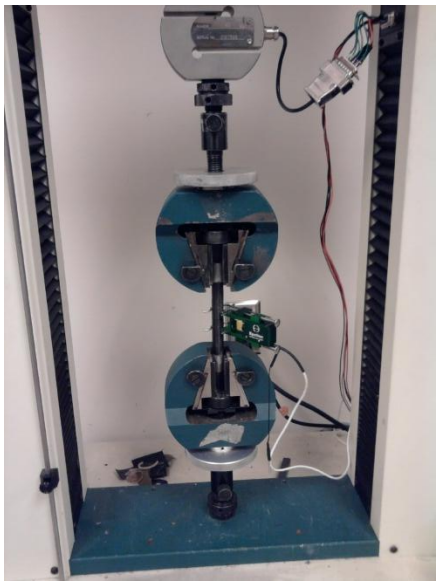

Figure 29. Room temperature test setup.

This test setup was used to ensure that the finite element model could predict the stiffness of joints with varying composite layups. Therefore three different composite layups were tested. For each composite layup three separate joint samples were manufactured. The composite layups that were tested were a [+θ,-θ,0,-θ,+θ]. The θ values tested were 15°, 45°, and 60°.

8.2 Test Results

In the test results it was found that the stiffness of the joint samples was extremely sensitive to the manufacturing process. Several iterations on the joint sample manufacturing process were undertaken and the results presented were the most consistent in all of the trials. Still, due to the sensitivity, significant difference is still seen from sample to sample. But the expected trend is present in that the stiffness increases with fiber angle. This is also proof that the bond is doing its job in transferring the load to the composite sleeve without failing.

8.2.1 Test Repeatability

First, the results for the individual sample are presented to show that the test was repeatable. Only one of each layup configuration being load cycled is presented.

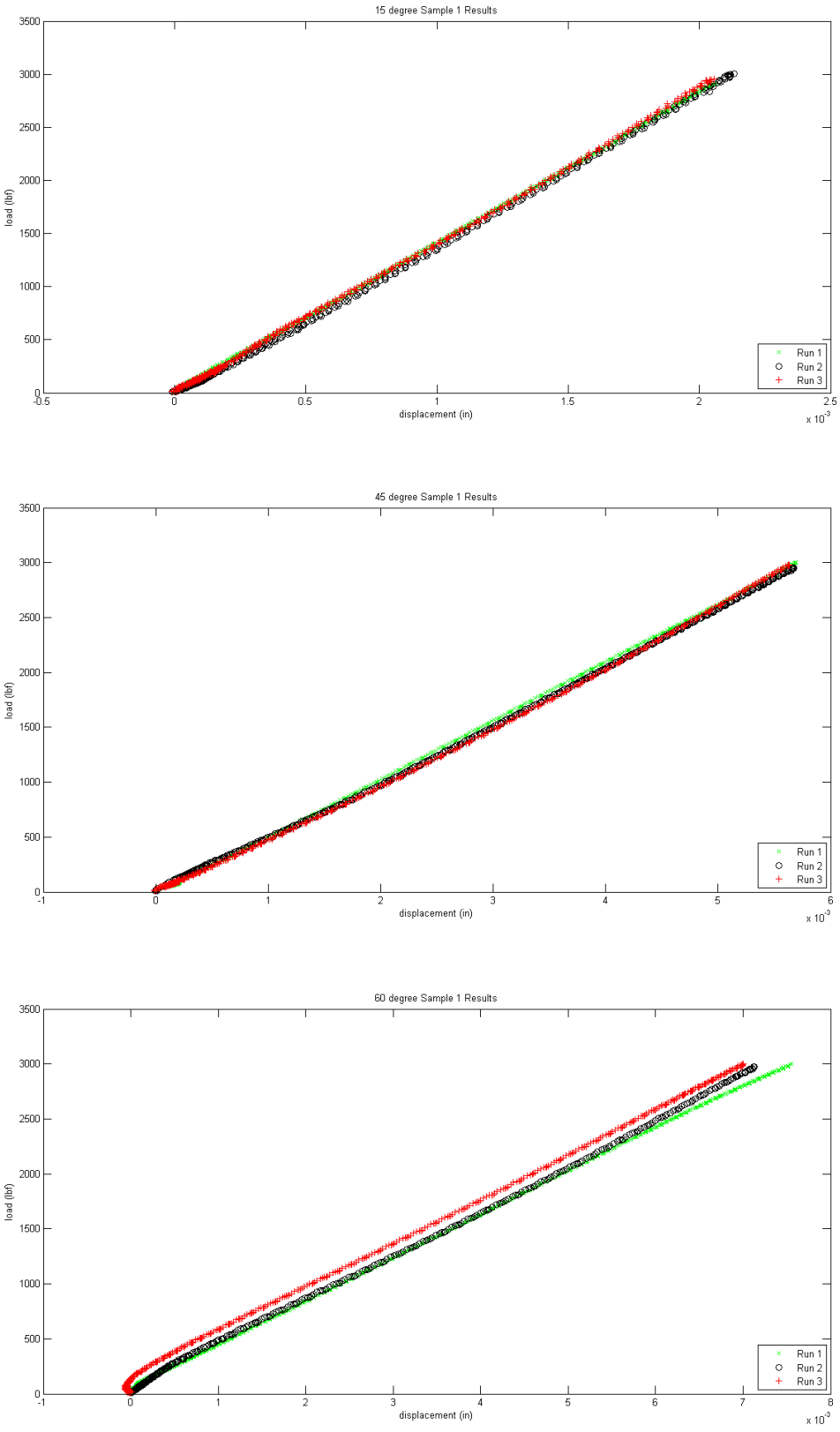

Figure 30. Sample repeatability results for the three composite layups.

Figure 30 shows that the experimental setup is able to repeat the measurement. Therefore it is verified that the test was within the elastic limit of the joint.

8.2.2 Room Temperature Measured Results Compared with FEA

Next the results for the three independent samples of the same composite layup are presented. Along with the measured data is the finite element models prediction of the joints force vs. displacement plot. A case study was performed using the finite element code to determine which material properties had the most profound effect on the stiffness of the joints. Using the acquired knowledge, the material properties were adjusted until the model was able to match the measured data. The same material properties were used to run each of the composite layup configurations. The determined material properties are presented in Table 4. It was expected that the material properties would need to be adjusted due to the fact that the properties are dependent on the fiber volume fraction obtained in each sample. Also the matrix properties are highly dependent of the manufacturing process and are expected to change from sample to sample.

Table 4. Room Temperature Material Properties

	$E_1(GPa)$	$E_2(MPa)$	ν_{12}	ν_{23}	$G_{12}(MPa)$
Aluminum	67GPa (9.72Msi)	-	.3	-	-
Adhesive	.7GPa (101.5Ksi)	-	.43	-	-
Composite	110GPa (15.95Msi)	230MPa (33.36Ksi)	.248	.458	83MPa (12.04Ksi)

The joint samples were modeled taking advantage of symmetry both in the axisymmetric case as well as longitudinally. Therefore, at the left edge the u displacements were set to zero, the

appropriate symmetry constraint. On the right side a uniform load was applied across the aluminum, equivalent to the load put on the sample by the tensile machine. The left and right edges are labeled in Figure 2. Presented along with the force vs. displacement plots are the finite element results in the deformed state. Like commercial codes the displacements are greatly exaggerated to allow them to be seen.

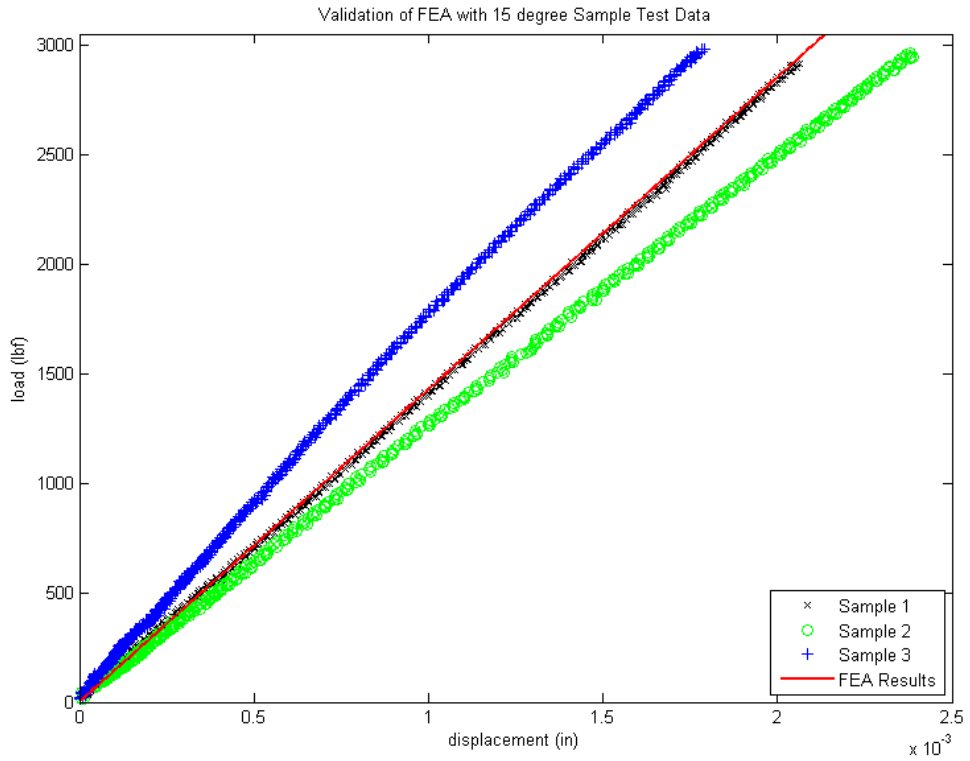

Figure 31. Room temperature force vs. displacement plots for the 15° samples along with FEA results.

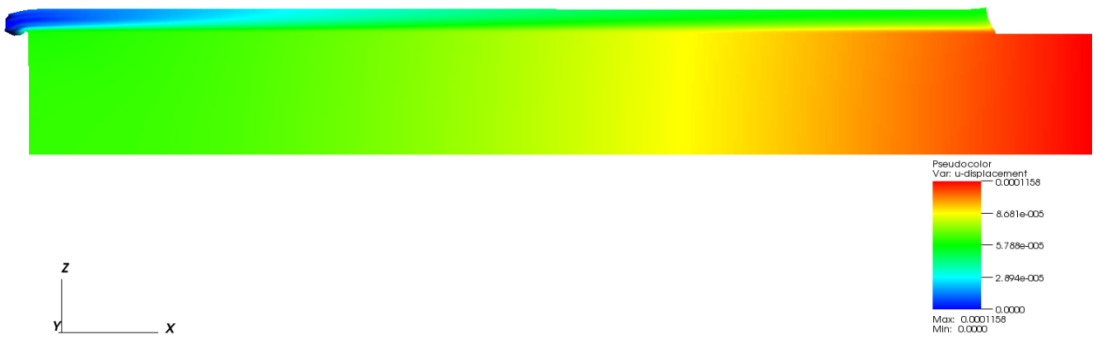

Figure 32. Deformed finite element u-displacements results for 15° composite layup with a 13345N (3000lbf) load.

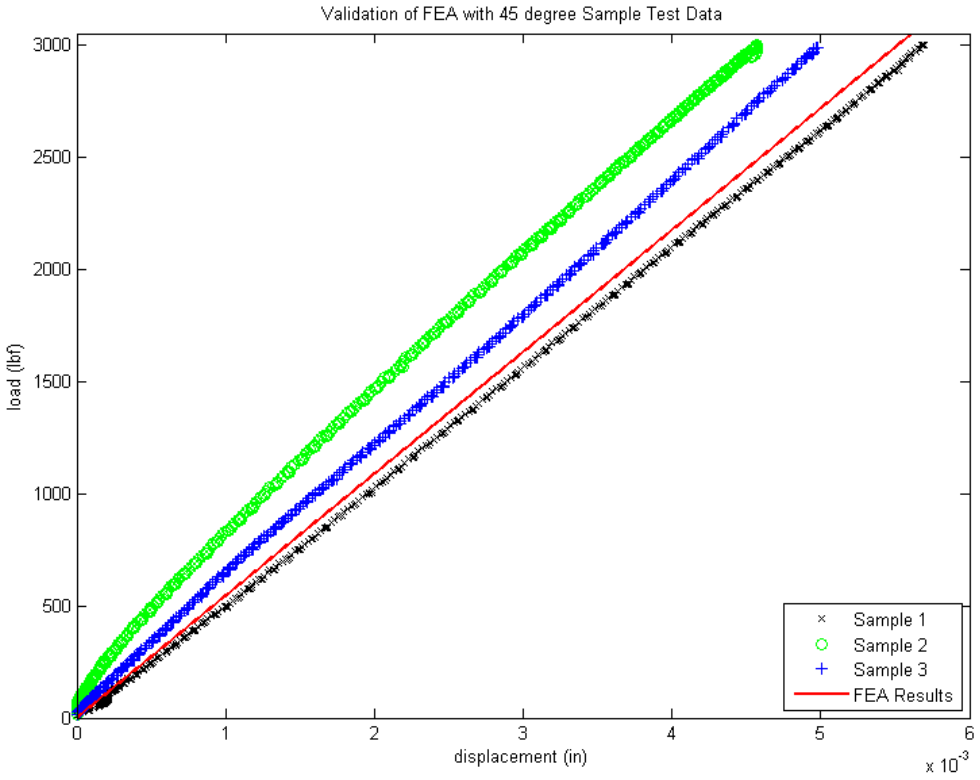

Figure 33. Room temperature force vs. displacement plots for the 45° samples along with FEA results.

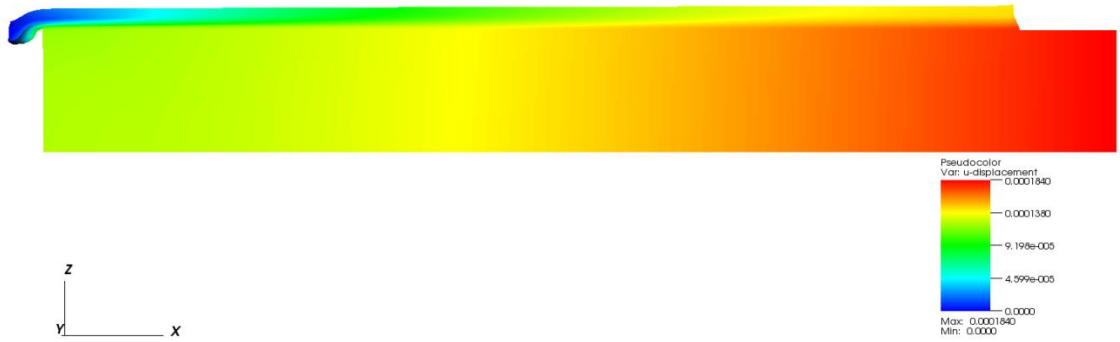

Figure 34. Deformed finite element u-displacements results for 45° composite layup with a 13345N (3000lbf) load.

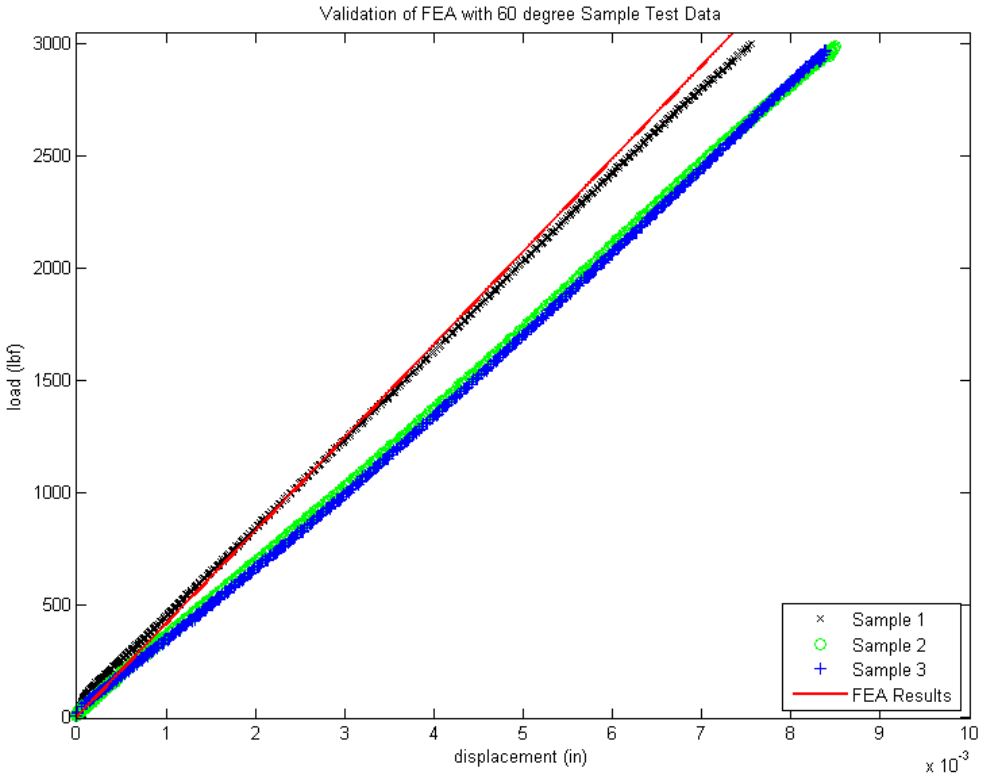

Figure 35. Room temperature force vs. displacement plots for the 60° samples along with FEA results.

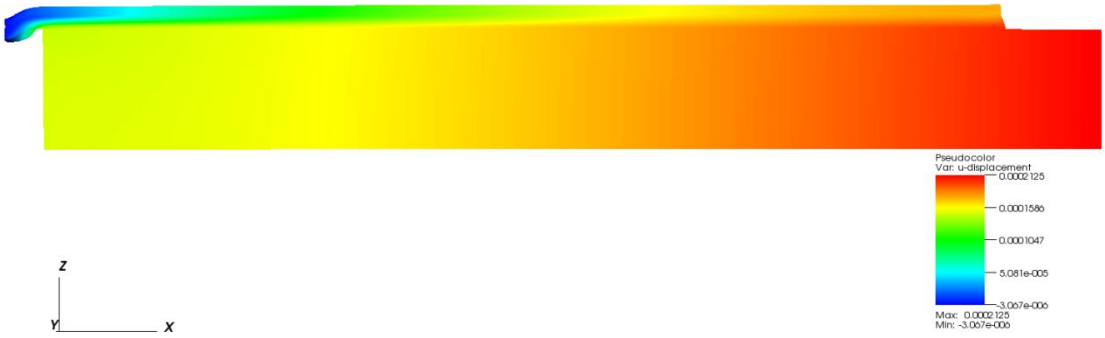

Figure 36. Deformed finite element u-displacements results for 60° composite layup with a 13345N (3000lbf) load.

As is evident in the above plots the FEA is able to predict the trends seen at room temperature for tensile loading. If a more automated process was available to manufacture the

joints, less spread could be obtained. All of the results combined on one plot to show the overall trend and how the FEA matches is shown in Figure 37.

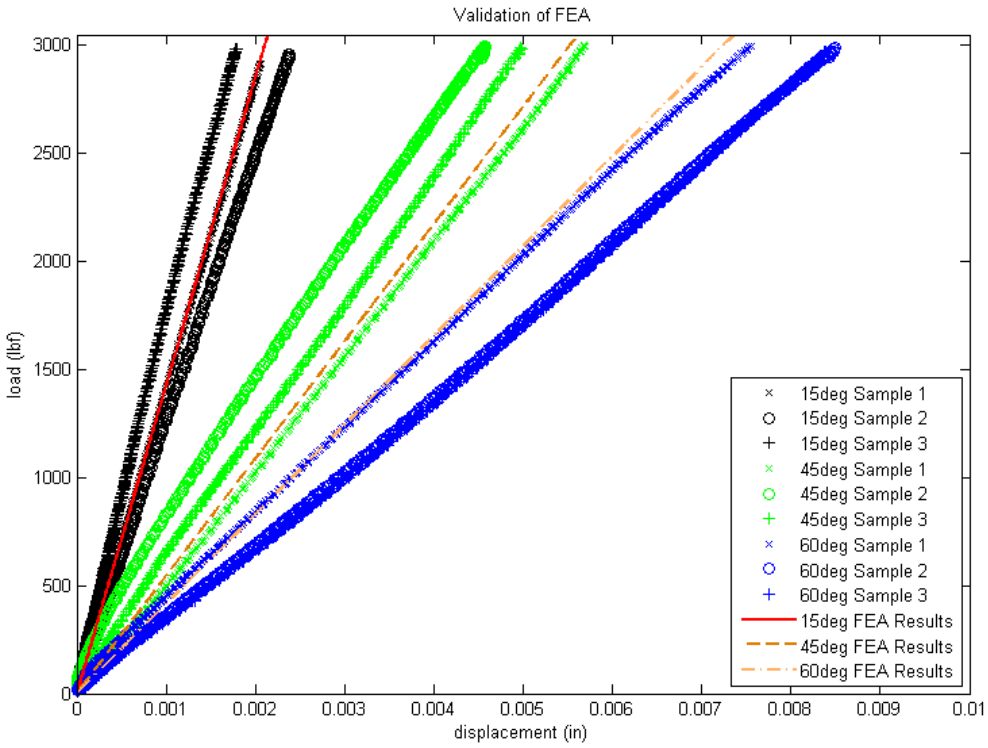

Figure 37. Validation of finite element analysis to predict joint displacement at room temperature.

CHAPTER 9

JOINT RESPONSE TO CRYOGENIC ENVIRONMENT

The reason for performing cryogenic testing is two-fold. First it is requisite that the joints are able to withstand the initial thermal shock experienced when entering space. The second objective was to ensure that the joints "settle down," and behave consistently after the first several thermal cycles. Like the testing done in Chapter 8, in depth uncertainty analysis is omitted because the sample to sample variation is the only significant contributor. Material CTE property estimates were obtained for the aluminum and the composite fiber direction. The perpendicular direction CTE estimates were not pursued due to high sensitivity to manufacture inputs.

9.1 Experimental Setup

In order to verify that the joints "settle down," displacement data was taken. "Settled down" meant that after the first several cycles the joints displacement when placed from a room temperature environment to a cryogenic environment become consistent and smooth. This data was acquired using the displacement portion of the setup outlined and verified in Chapter 6. The joints presented in Chapter 7 were placed directly into a liquid nitrogen bath with no effort taken to gradually bring the joints to liquid nitrogen temperature. Dimensions of the joints constituent parts were taken before the joints were made to allow for the center of the joint to be located. Marks were then made 25 mm (0.984252 in.) apart which is the gauge length of the extensometer, straddling the center. The knife blade of the extensometer was then placed on the marks. The extensometer was then gripped and suspended over the liquid nitrogen bath to ensure the joint was held still and not bumped. The samples were left in the liquid nitrogen bath until the amount of boiling around the joint diminished significantly which was observed to correspond well with the displacement measurement becoming constant. One minute 30 seconds was the determined time needed for the joint to reach equilibrium conditions. A joint gripped by the extensometer and suspended in the container is shown in Figure 38. The setup with the joint suspended in liquid

nitrogen is shown in Figure 39, the joint is at equilibrium and is evident because boiling has subsided.

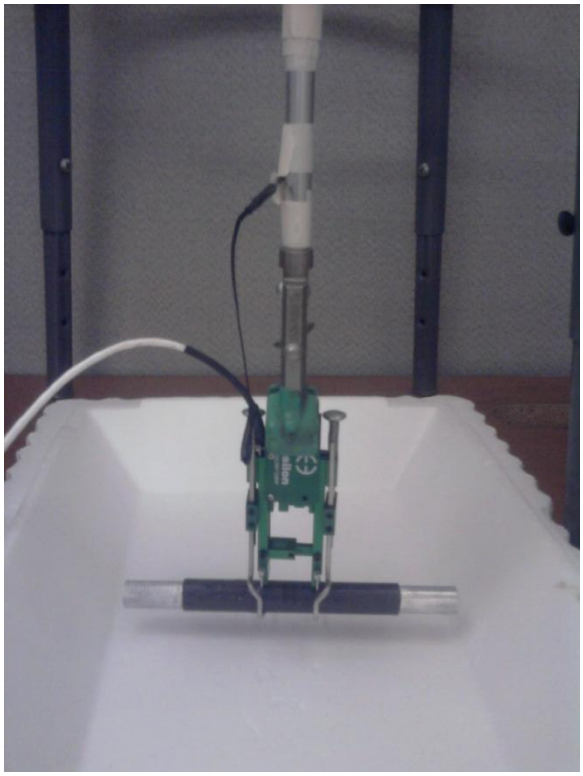

Figure 38. Cryogenic temperature test setup.

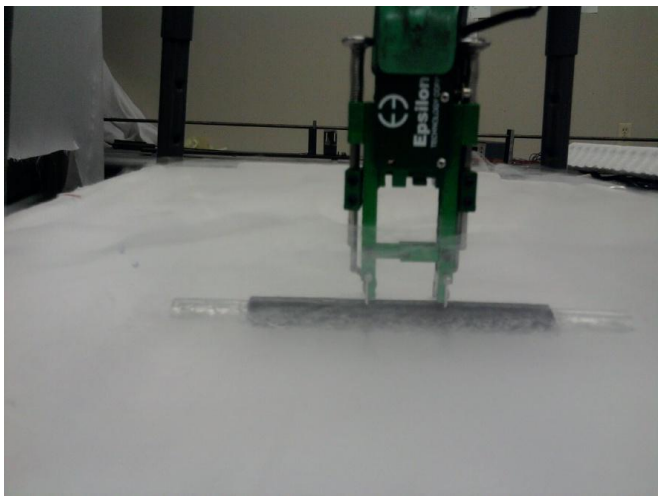

Figure 39. Cryogenic temperature test setup with liquid nitrogen bath.

Each joint was submersed into the liquid nitrogen bath while displacement measurements were being taken a total of five cycles. A cycle consists of rapidly cooling the joint to liquid nitrogen temperature and allowing the joint to return to room temperature. The effect of the composite layup used in the joint on the settled displacement value was to be explored. Therefore three different composite layups were tested. The same samples used in the room temperature testing of Chapter 8 were used here. The composite layups that were tested were a $[+\theta,-\theta,0,-\theta,+\theta]$. The θ values tested were 15°, 45°, and 60°.

9.2 CTE Estimates

Because the properties of the aluminum and fiber direction in the composite were found to be consistent in the room temperature stiffness testing, it was assumed that the CTE would possibly be as well. The direction perpendicular to the fiber direction in the composite is dominated by the matrix properties which are extremely sensitive to the manufacturing environment and are expected to change from sample to sample. Therefore, obtaining an estimate would prove to be useless. A pure aluminum sample and a unidirectional composite tube were cycled in the same way as the joint samples. The results are presented in Figure 40 and Figure 41 The aluminum sample does not exhibit the cracking and settling that is seen in the joints and composite samples. Aluminum is a homogenous material and therefore shrinks at the same rate making a smooth consistent curve independent of the cycle number. For the fourth cycle the sample was only allowed 45 minutes at room temperature. It is suspected that the sample was not allowed to reach room temperature again resulting in the reading leveling out before the other four cycles. This indicated that at least one hour would be needed in between cycles from the time the joints were removed from the nitrogen bath. For this reason the fourth cycle was excluded in the CTE estimate calculation. In the interest of time and ease only the first and fifth cycle were recorded in the UD composite tube testing.

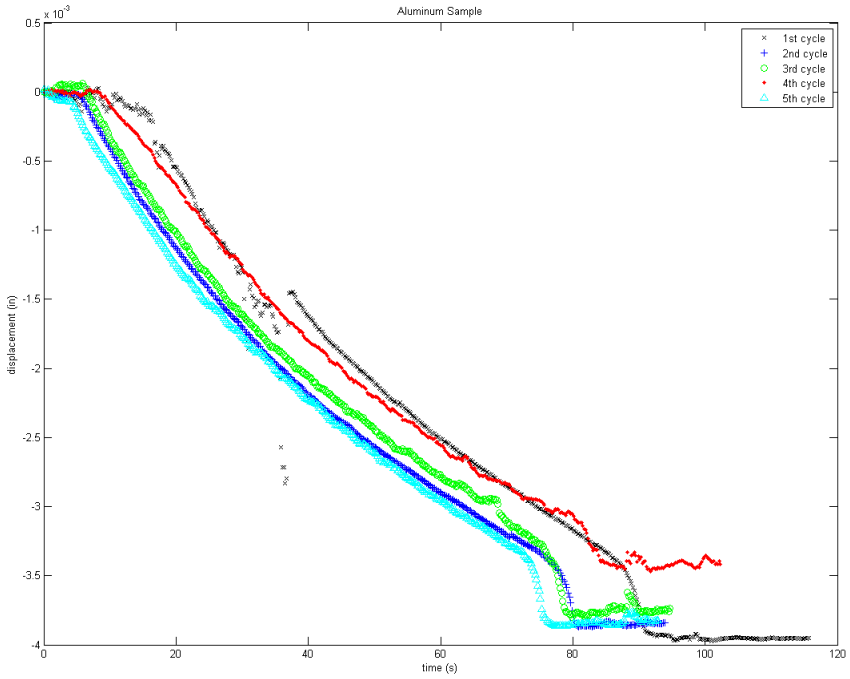

Figure 40. Aluminum sample displacement response when placed in liquid nitrogen bath.

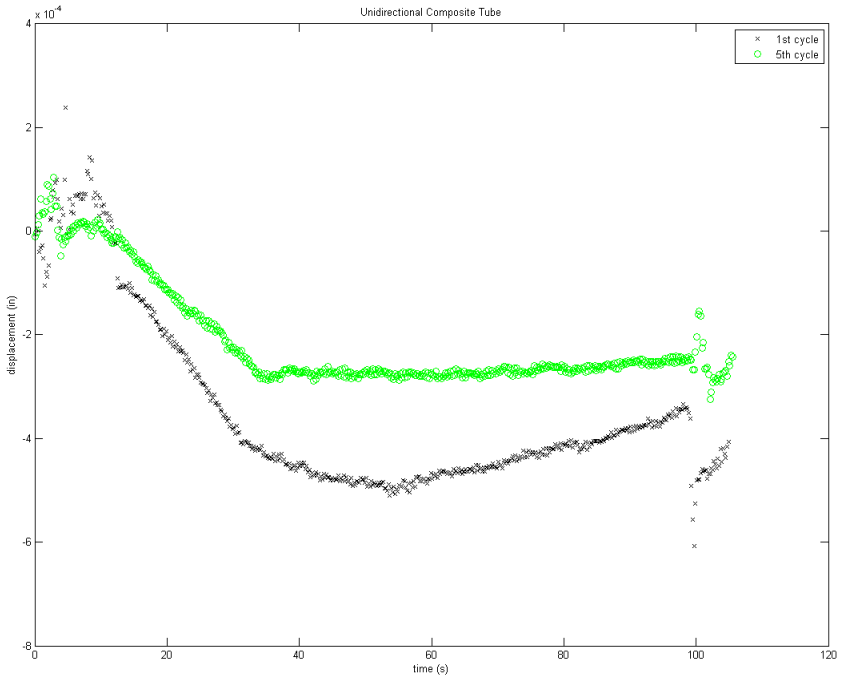

Figure 41. Unidirectional composite tube displacement response when placed in liquid nitrogen bath.

The coefficient of thermal expansion can easily be calculated with the obtained displacement data. The induced strain can be calculated by dividing the measured displacement by the gauge length of the extensometer. The change in temperature is known to be from room temperature down to boiling liquid nitrogen temperature, -217°C (-390°F). The measured displacement used was the mean of 50 samples taken when the displacement vs. time plot became constant. The results are shown in Table 5.

Table 5. CTE Estimates

		ΔT	displacement (in) at LN temperature	displacement (m) at LN temperature	induced strain	CTE (/°C)	CTE (/°F)
Aluminum	1st cycle	-217°C -390°F	-3.9555E-03	-1.0047E-04	-4.0188E-03	1.8058E-05	1.0047E-05
	2nd cycle	-217°C -390°F	-3.8540E-03	-9.7892E-05	-3.9157E-03		
	3rd cycle	-217°C -390°F	-3.7744E-03	-9.5869E-05	-3.8348E-03		
	5th cycle	-217°C -390°F	-3.8433E-03	-9.7620E-05	-3.9048E-03		
UD composite	5th cycle	-217°C -390°F	-2.7551E-04	-6.9980E-06	-2.7992E-04	1.2899E-06	7.1774E-07

Like the Young's modulus measurement for the aluminum, the measured CTE also matches well with published data. The accepted CTE between 20°C and -196°C (70°F and -320°F) is 18.5 E-6/°C, only a 2.5% difference.

9.3 Test Results

Like the test results in the room temperature tensile testing presented in Chapter 8, variations were found from sample to sample in the temperature cycling results as well. This was to be expected because the same samples were used in the temperature cycling tests. For the same reasons presented in Chapter 8, thermal properties are sensitive to the manufacturing process. Still with the slight variation from sample to sample when the estimated CTE's for the aluminum

and fiber direction of the composite were input into the model the basic expected trend predicted by the model is present within the test data. Counter to what was expected, the trend found was that the 15° and 60° samples showed about the same u-displacement while the 45° sample showed noticeably less. With the initial property estimates found in composites literature this was not the predicted trend, but with the CTE estimates found from measuring actual samples the model was able to accurately model the actual behavior. The joints also did not visibly fail on the macro scale although localized cracking was heard throughout the first and second cycle.

9.3.1 Joint Settling

First the results for an individual sample for each of the composite layup are presented to show that the samples are settling down at around the 5^{th} cycle. All of the samples behaved similarly. Therefore, presenting all of the results would contribute no further proof.
As is evident in Figure 42 the samples are converging on a constant settling displacement as the cycles continue. Like the room temperature tensile testing results the 60° sample shows a bit more variation due to the more pronounced role the matrix is playing. In this case the matrix is experiencing micro-crack density growth, making the settling down phenomena more visible than in the 15° sample that is dominated by the fiber properties.

9.3.2 Measured Results Compared With FEA

Next the results for the three independent samples of the same composite layup are presented. Along with the measured data is the finite element models prediction of the displacement when the joint reached liquid nitrogen temperature. The estimated material properties calculated in Section 2 and presented in Table 5. along with published data for the CTE's of the adhesive and the direction perpendicular to the fibers in the composite were used in the model.

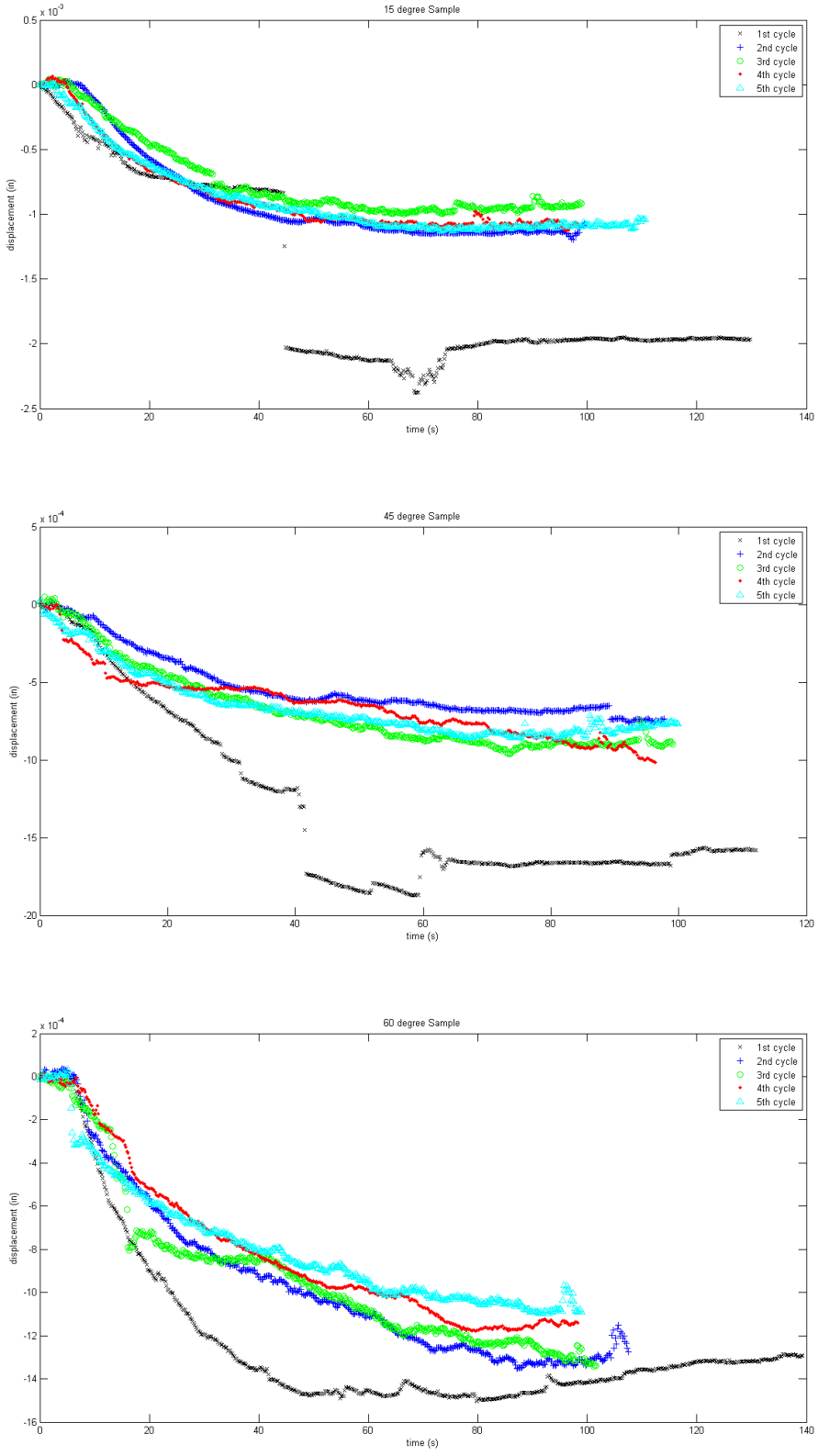

Figure 42. Sample cycling results showing joints settling at about the 5th cycle.

The joint samples were modeled taking advantage of symmetry both in the axisymmetic case as well as longitudinally. Therefore, at the left edge the u displacements were set to zero, the appropriate symmetry constraint. A uniform temperature change of -217°C (-390°F) was prescribed for the entire joint. Presented along with displacement response of the joint to the temperature change are the finite element results in the deformed state. Like commercial codes the displacements are greatly exaggerated to allow them to be seen.

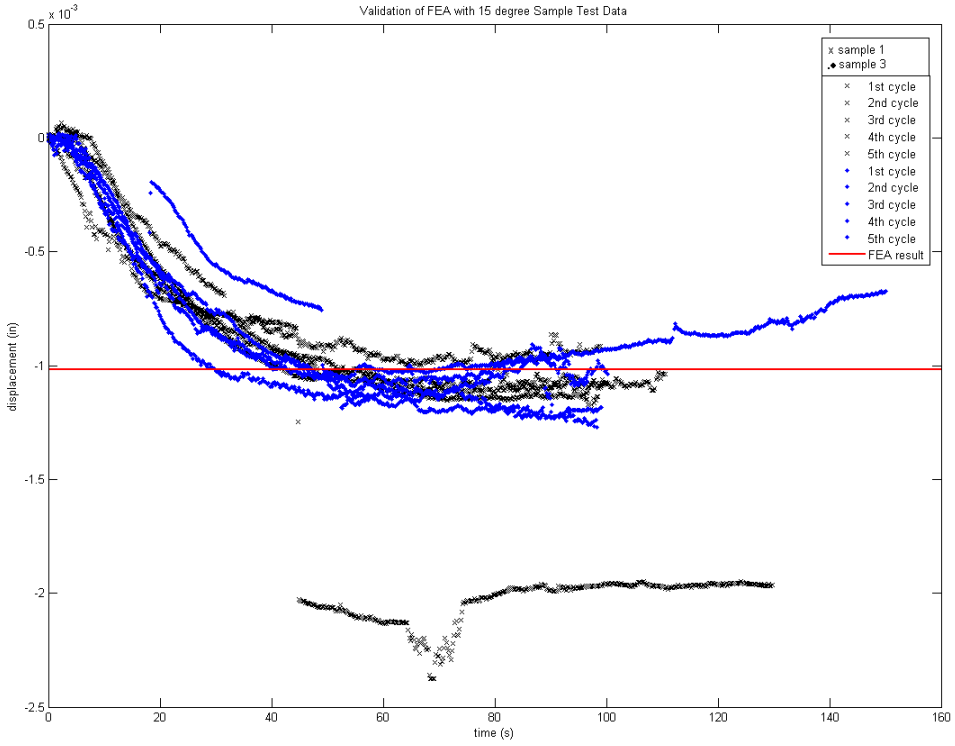

Figure 43. Measured displacement data of joints when submerged in liquid nitrogen bath. FEA result when joint reaches equilibrium at liquid nitrogen temperature. Data for Sample 2 was especially noisy and was thrown away.

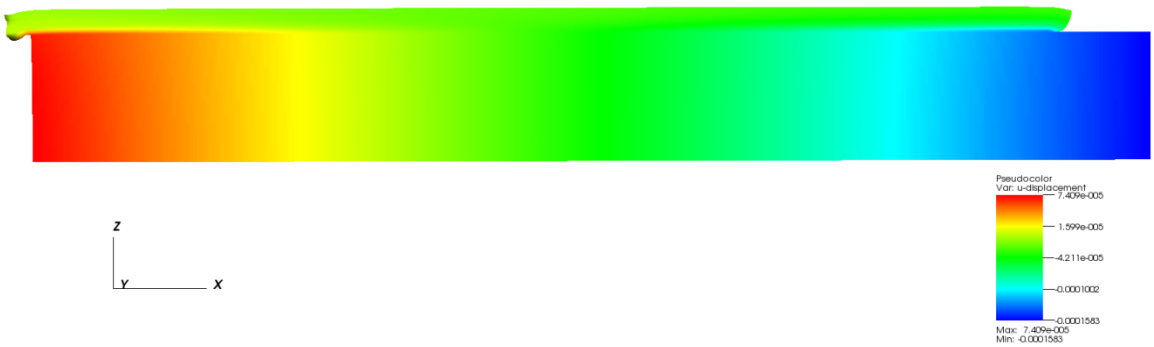

Figure 44. Deformed finite element u-displacements results for 15° composite layup with a -217°C (-390°F) temperature load.

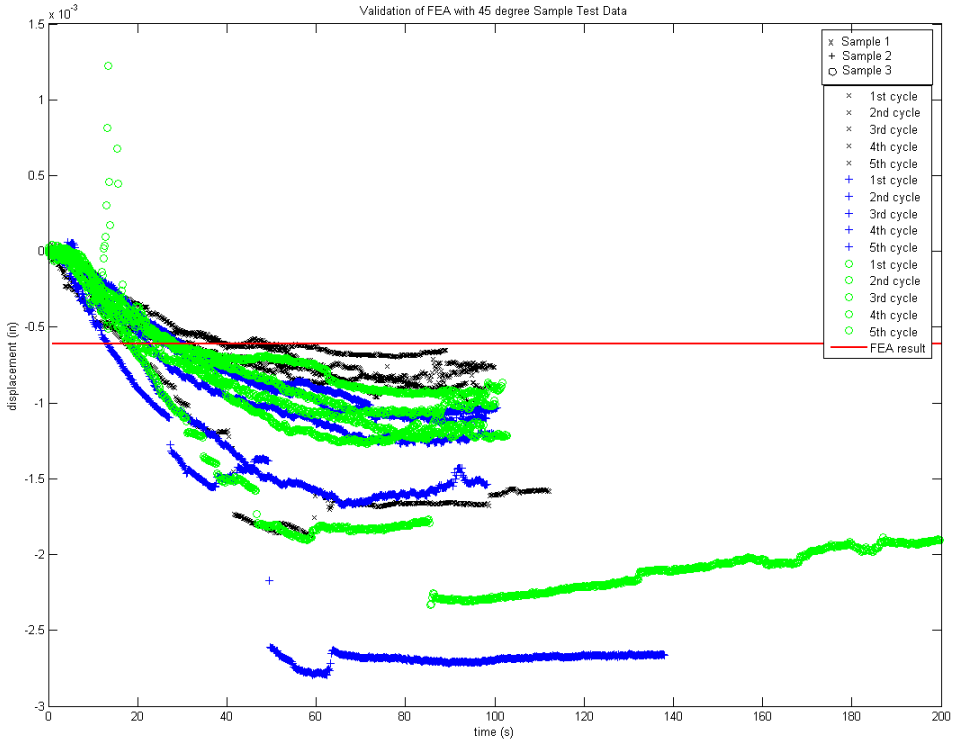

Figure 45. Measured displacement data of joints when submerged in liquid nitrogen bath. FEA result when joint reaches equilibrium at liquid nitrogen temperature.

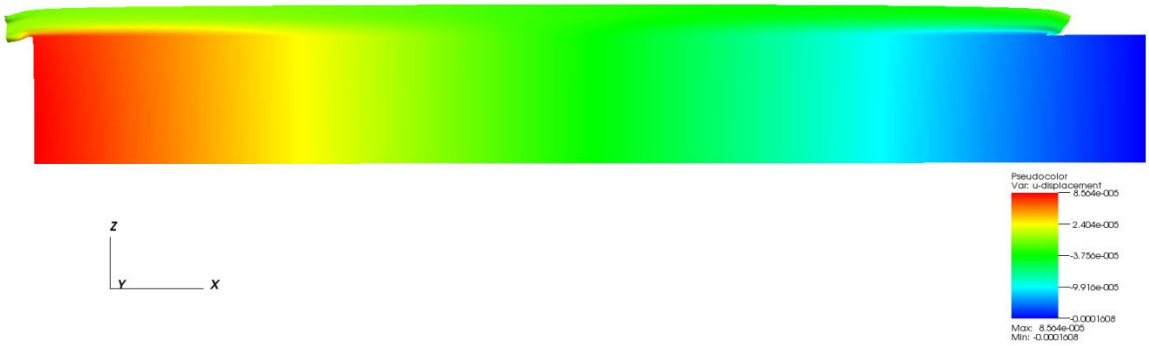

Figure 46. Deformed finite element u-displacements results for 45° composite layup with a -217°C (-390°F) temperature load.

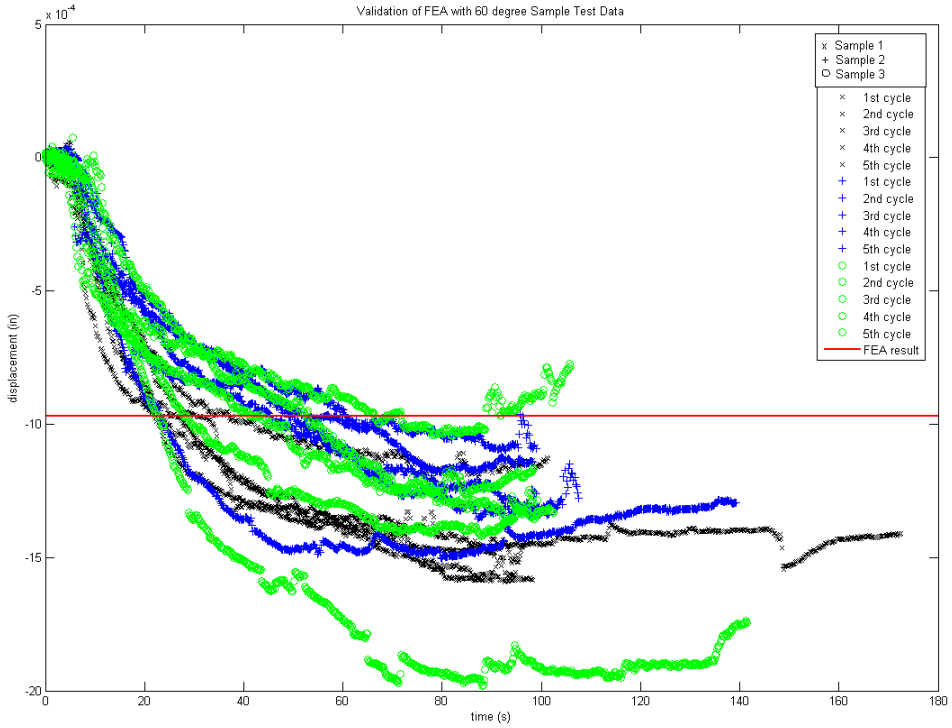

Figure 47. Measured displacement data of joints when submerged in liquid nitrogen bath. FEA result when joint reaches equilibrium at liquid nitrogen temperature.

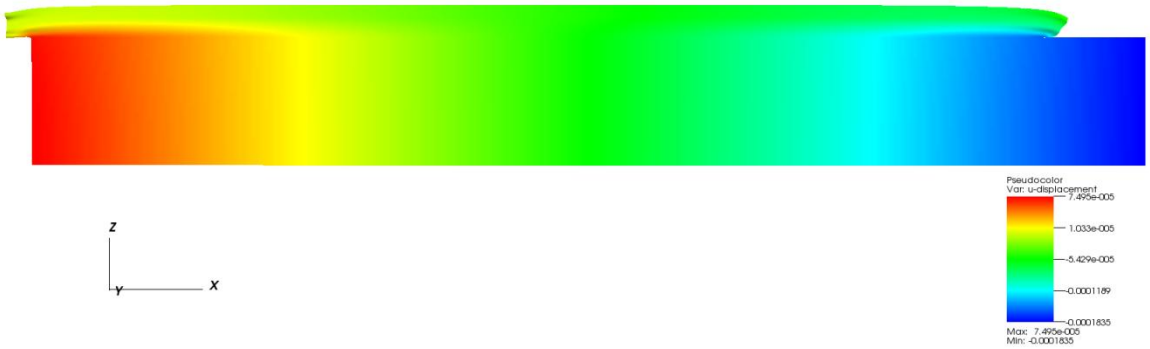

Figure 48. Deformed finite element u-displacements results for 60° composite layup with a -217°C (-390°F) temperature load.

In the above plots it is again evident that the difficulty in producing predictable results becomes more evident as the matrix becomes more influential as is seen in the data for the 45° and 60° layups. These layups are expected to need more cycles to see them level out completely to the FEA's prediction because matrix micro-cracking may not saturate until well past 10 cycles as was discovered in others work covered in the literature review of Chapter 2. Still in all of the plots it is evident that the samples displacement response is trending toward what the finite element model predicts even after only five cycles. The data recorded for the second 15° sample was thrown away because for unknown reasons the measurement was extremely noise. If a more automated process was available to manufacture the joints, again it is believed that less spread between samples could be obtained.

CHAPTER 10

JOINT STIFFNESS TESTING AT LIQUID NITROGEN TEMPERATURE

Liquid nitrogen tensile testing was done last to ensure that the joints structural integrity remained after the joints had undergone temperature cycling. Because the proper fixture was not available to run the tensile test with the sample submerged in liquid nitrogen, the temperature of the sample was measured every 10 seconds during the test to track the temperature of the joint during the testing period. Again, in depth uncertainty analysis was omitted due to the fact that the sample to sample variation made the other uncertainty contributions insignificant.

10.1 Experimental Setup

In order to ensure that the integrity of the joints remained after thermal cycling, force and displacement data was taken until joint failure. This data was acquired using the setup outlined and verified in Chapter 6 The joints presented in Chapter 7, that had now had room temperature force vs. displacement data taken as well as displacement response to thermal loading data taken, were placed into the tensile testing machine at liquid nitrogen temperature. The joints were taken directly from a liquid nitrogen bath and placed into the tensile machine. The joints remained in the liquid nitrogen bath for a minimum of 30 minutes to ensure uniform temperature. Dimensions of the joints constituent parts were taken before the joints were made to allow for the center of the joint to be located. Marks were then made 25 mm (0.984252 in.) apart which is the gauge length of the extensometer, straddling the center. The knife blades of the extensometer were then placed on the marks. The samples were then loaded at a constant rate of 2.54 mm (.1 in.) per minute a common rate used in composites testing. The samples were loaded until failure occurred. Displacement and Load data was taken simultaneously allowing for a force vs. displacement plot to be created. The joint in the tensile testing machine with extensometer placed on the cold sample can be seen in Figure 49.

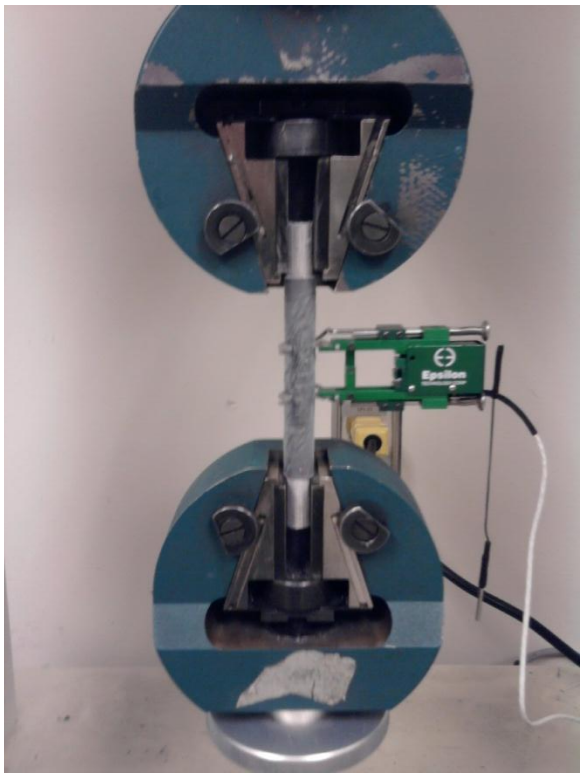

Figure 49. Transient temperature test setup.

This test setup was used to ensure that the joints structural integrity remained after the temperature cycling as well as ensuring the model could predict joint behavior at cryogenic temperatures. The same three composite layups used in the previous tests were tested. The composite layups that were tested were a [+θ,-θ,0,-θ,+θ]. The θ values tested were 15°, 45°, and 60°.

10.2 Test Results

As was seen in Chapters 8 and 9 there were slight variations from sample to sample due to manufacturing error. Again with the slight variations from sample to sample the test still showed that the joints maintained structural integrity after the thermal cycles as well as providing evidence of the finite element models capability to predict joint behavior even at cryogenic temperatures.

10.2.1 Joint Strength

In the test results it is evident that the joints structural integrity remained after the temperature cycling. The average strength of all of the samples was 2550 N (4620 lbf). The standard deviation of the mean strength was 2313 N (520 lbf). A bar plot of the strength results can be seen in Figure 50. A summary of the failure mode and total test time can be found in Table 6.

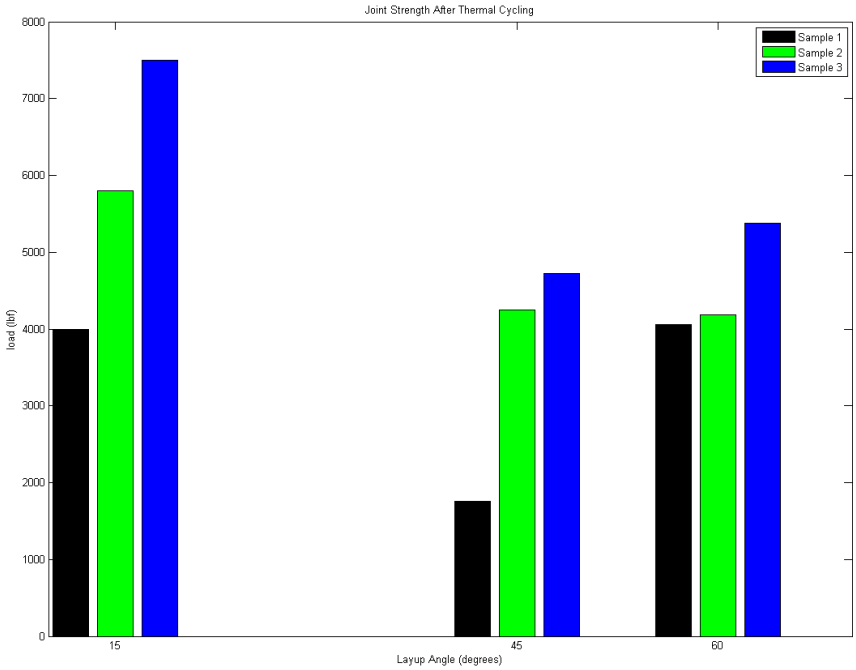

Figure 50. The load at which each of the joint samples failed after five thermal cycles.

Of the nine joints, 45° Sample 2 was the only joint that the thermal cycling lowered the joints strength below the elastic range tested in the room temperature tensile testing presented in Chapter 8. Several different failure modes were seen in the test. Three of the joints failed between composite layers in a brittle type failure mode, linear curve until fracture. One of the joints failed within the adhesive layer in a brittle type failure mode. Two of the joints failed in a mixed adhesive composite brittle type failure mode. Two of the joints bonds were so strong that the

aluminum ends being gripped by the tensile machine grips began to yield. One of the joints broke in half at the center; this was due to the joint being slightly bent causing stresses to build at the center. The following figures document the joint failures.

Table 6. Sample Failure Modes and Total Test Times

	Mode of Failure	Total Test Time (s)
15° Sample 1	Brittle type adhesive failure	125.7
15° Sample 2	Aluminum Yielding	405.7
15° Sample 3	Aluminum Yielding	373.5
45° Sample 1	Brittle type interlaminar composite failure	179.7
45° Sample 2	Brittle type interlaminar composite failure	140.3
45° Sample 3	Brittle type mixed Interlaminar composite\adhesive failure	203.9
60° Sample 1	Broke in center	223.3
60° Sample 2	Brittle type mixed Interlaminar composite\adhesive failure	174.1
60° Sample 3	Brittle type interlaminar composite failure	176.9

The joints' failing in several different modes is evidence that the joint design has no obvious weak points. The mode of failure is driven by imperfections in the manufacturing process rather than a flaw in the joint design process. The joint strength results also are deemed to be sufficient to show that the joints are able to withstand the initial thermal shock experienced in space applications.

Figure 51. 15° Sample 1 adhesive layer brittle type failure.

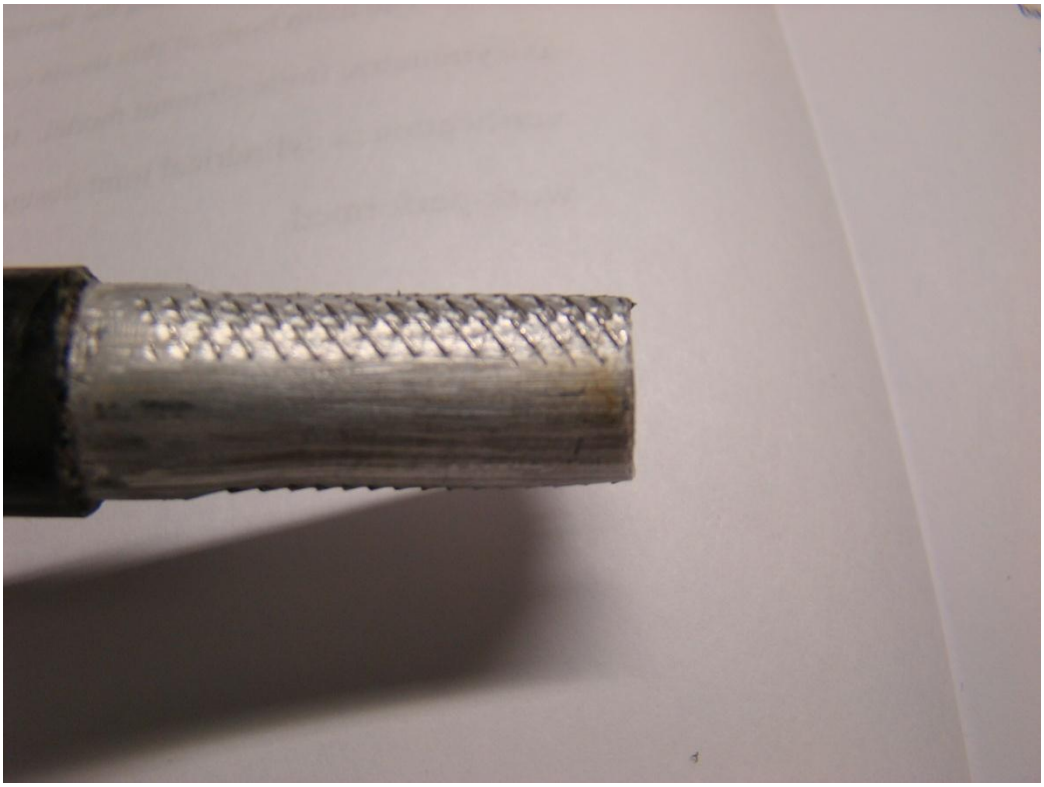

Figure 52. 15° Sample 2 aluminum began to yield before joint failure.

Figure 53. 15° Sample 3 aluminum began to yield before joint failure.

Figure 54. 45° Sample 1 interlaminar composite brittle type failure.

Figure 55. 45° Sample 2 interlaminar composite brittle type failure.

Figure 56. 45° Sample 3 mixed interlaminar composite/adhesive brittle type failure.

Figure 57. 60° Sample 1 broke in the center due to not being kept perfectly straight during cure.

Figure 58. 60° Sample 2 mixed interlaminar composite/Adhesive brittle type failure.

Figure 59. 60° Sample 3 interlaminar composite brittle type failure.

10.2.2 Transient Temperature Measured Results Compared with FEA

Next the results for the three independent samples of the same composite layup are presented. Upon testing of the cooled joints it was found that by the end of the testing period the joints had almost warmed back to room temperature due to the rapid inflow of heat from the room temperature grips. But, the force vs. displacement data for the transient temperature tests still looked linear. This indicates that the material properties aren't changing significant amounts over the temperature range when compared to the inherent manufacturing defects and varying matrix property. In order to be complete a temperature response curve of the sample over the testing period was measured. A type K thermocouple was attached to the center of the joint and using an Omega HH506R thermometer, pictured in Figure 60, temperature readings were taken every 10 seconds of the test. The temperatures were recorded while the joint was gripped and loaded in the tensile testing machine, to ensure the same conditions are met as in the actual test. The total time

of each test is recorded in Table 6. A picture of the thermocouples placement on the joint is shown in Figure 61. The typical temperature curve is shown in Figure 62.

Figure 60. Omega thermometer used to measure temperature at 10 sec intervals during test.

Figure 61. Placement of the thermocouple on the joint sample (placement is right at the center of the composite sleeve).

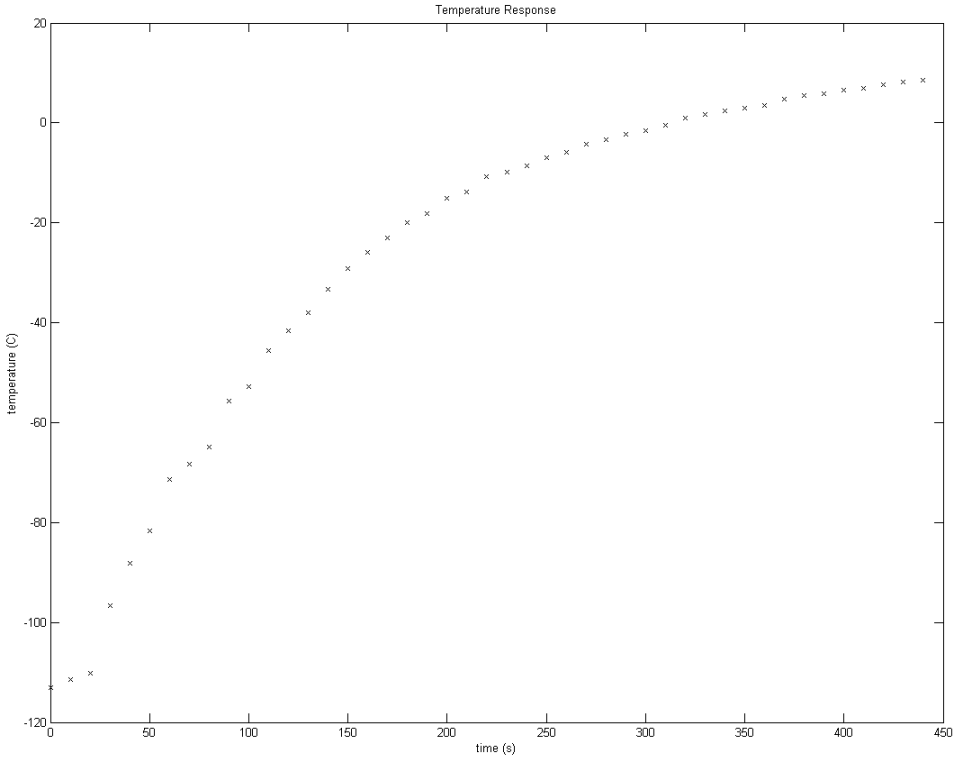

Figure 62. Temperature response of center of joint to test configuration.

Below the measured data is presented with the finite element models prediction of the joints force vs. displacement plot. Notice that the trend of the measured data is mostly linear even though the joint is changing temperature. If the joint materials properties were not sensitive to temperature, as this linearity suggests, the joint stiffness should not have changed much from the room temperature tensile testing results. Therefore the same material properties and therefore the same models were used to predict the transient temperature joint behavior.

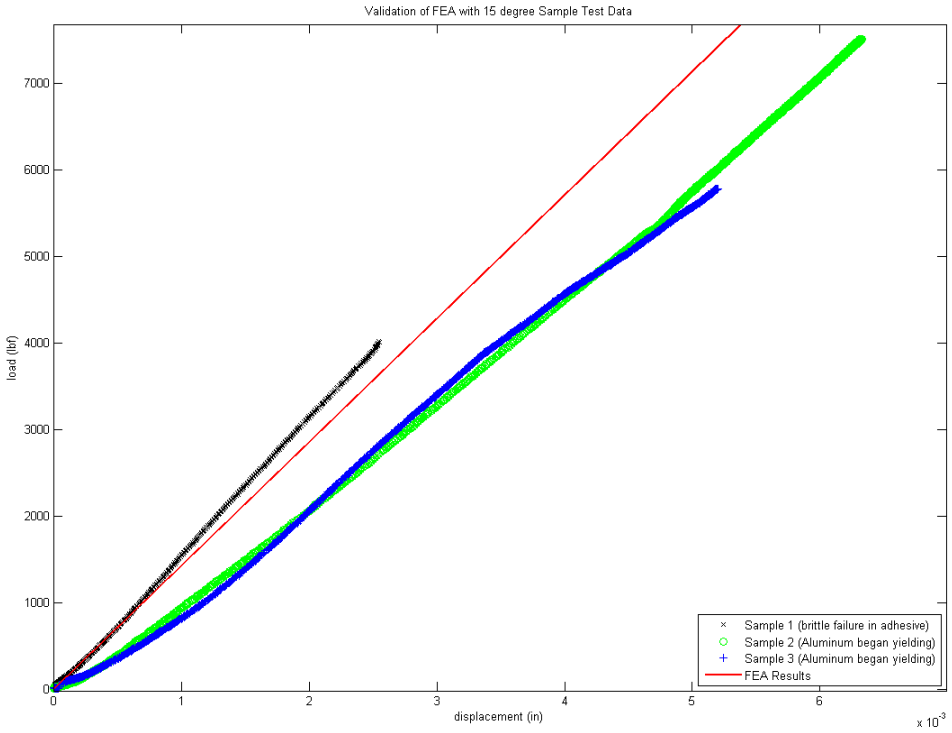

Figure 63. Transient temperature force vs. displacement plots for the 15° samples along with FEA results.

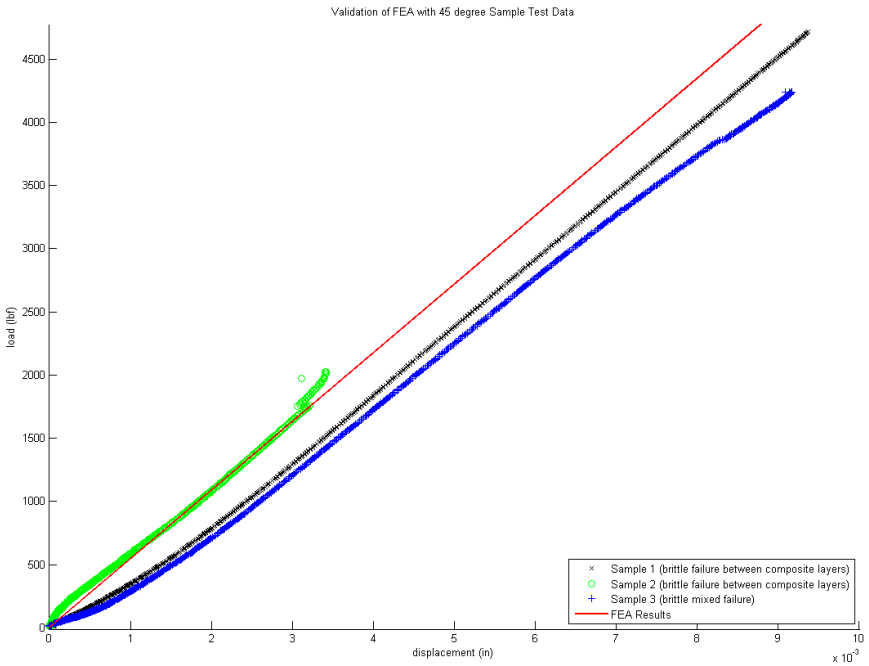

Figure 64. Transient temperature force vs. displacement plots for the 45° samples along with FEA results.

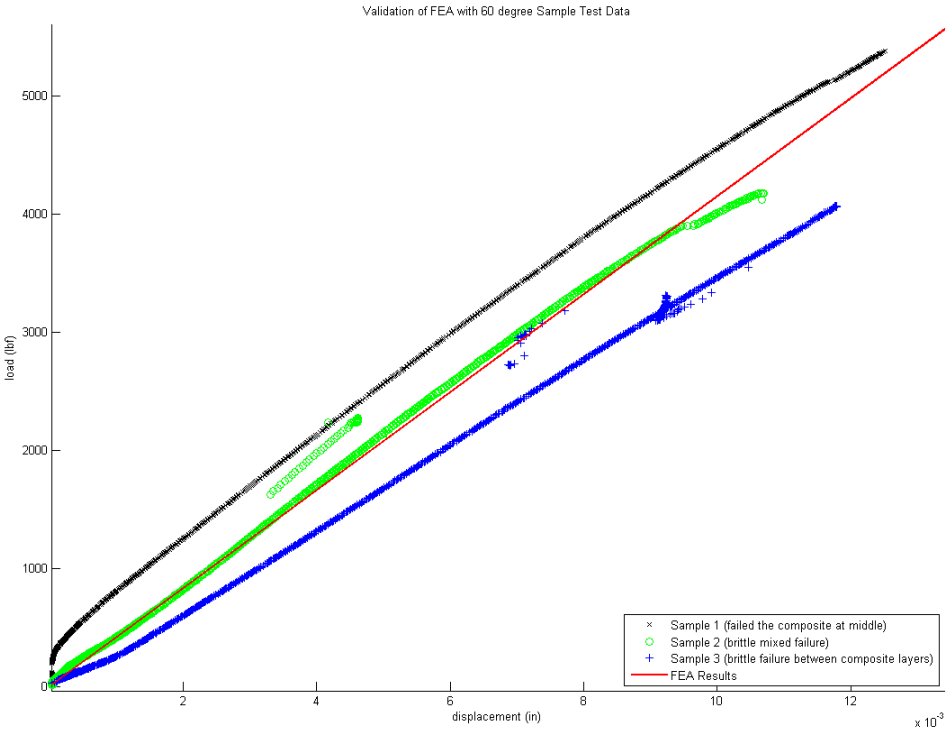

Figure 65. Transient temperature force vs. displacement plots for the 60° samples along with FEA results.

As is evident in the above plots the FEA is able to predict the trends seen at transient temperatures for tensile loading. This also is a good indication that temperature of the joints has little impact on the joints mechanical properties and makes the design significantly easier. If a more automated process was available to manufacture the joints, less spread could presumably be obtained.

CHAPTER 11

CONCLUSIONS

Several conclusions about cylindrical adhesive joint behavior can be drawn from the completed work. Some of the findings are typical while others were more significant and unsuspected. The big picture final conclusion is that axisymmetric finite element modeling when done correctly ensuring proper mesh refinement and low element aspect ratios can accurately predict cylindrical adhesive joint behavior. In the following sections, findings are presented that when considered together support this claim.

11.1 Conclusions Drawn from Room Temperature Tensile Testing

The results of the room temperature tensile testing allowed an avenue for the test setup to be rigorously verified through bending checks and aluminum modulus testing to ensure simple cases could accurately be measured. With the gained confidence it was then possible to show graphically that the model could very easily predict trends seen in the mechanical behavior of the joint samples.

Given the confidence that the measured values of the joints displacement was accurate through repeated tests yielding the same result made it blatantly obvious that the different samples were indeed slightly different. Although special care was taken in the manufacturing of the joints to ensure the samples were identical, it was found small differences can result in significant stiffness change. One variable in the manufacturing process is the fiber alignment for the angled plies. A study was performed to investigate how much a 5° change in fiber alignment effects sample stiffness. The results of the study are best presented in graphical form and are shown in Figure 66.

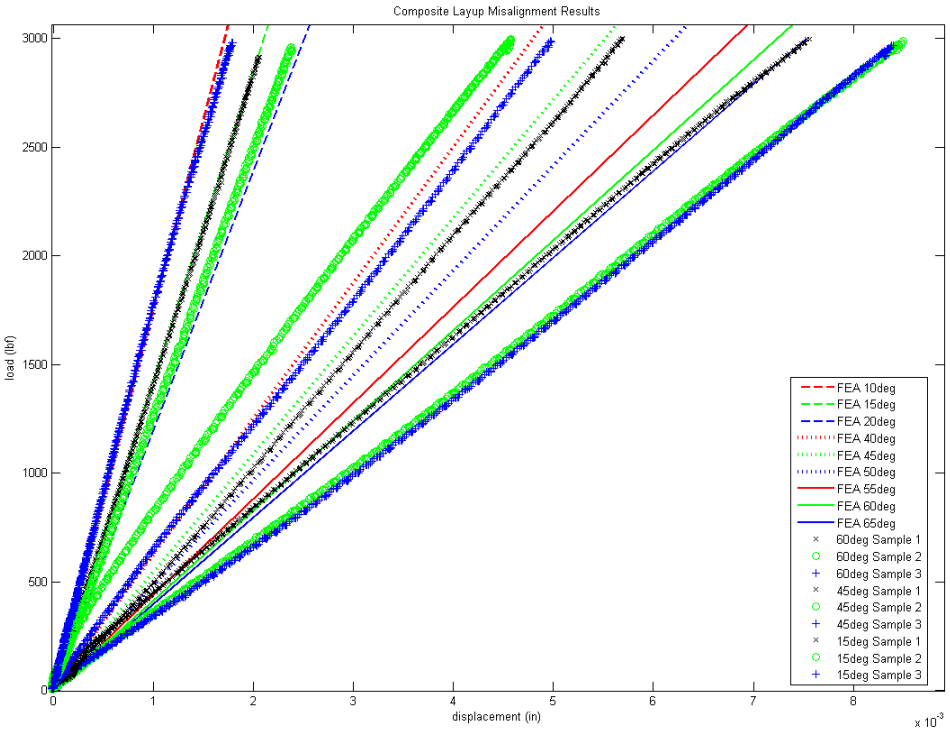

Figure 66. Misalignment study results.

The results suggest that at low fiber angles that misalignment may indeed be a major source of error between samples, due to the finite element results accuracy in bounding the measured results. While at higher fiber angles differences in the matrix drive the spread in joint stiffness. This is not hard to believe. As the fiber angle increases the role of the matrix properties dominates rather than the fiber properties. These changes in the matrix properties can most likely be attributed to pockets of resin rich and resin deprived regions within the joint due to imperfect shrink tape application. These two factors are thought to be the largest contributors to the spread seen between samples. These errors could be reduced significantly to produce highly consistent and predictable joints by applying a more automated manufacturing process to ensure fiber alignment and a uniform consistent application of pressure on the composite during the cure cycle.

11.2 Conclusions Drawn from Cryogenic Temperature Cycling

Two distinct conclusions can be drawn when reviewing the results of the cyclic temperature testing. Ample evidence that joints behave much like composite plates when subjected to repeated temperature cycling is seen in the individual joint results. Especially within the first two cycles it is evident that the joints begin to "settle down". The term "settle down" in this context means that after the first several cycles the joints displacement when placed from a room temperature environment to a cryogenic environment become consistent and smooth. This conclusion allows for these joints to be thermally cycled initially and then used in environments where temperature fluctuates, because the joints behavior can be predicted and ultimately designed for.

The second conclusion is that given the proper thermal properties the finite element model does a good job at predicting the trends seen between the joints with differing composite layups subject to a temperature change. After the measured CTE's for the fiber direction of the composite and the aluminum were input into the model it was able to predict the same trend seen in the measured data. At the point where the displacement data was taken it was found that the 15° and 60° samples had around the same displacement while the 45° samples moved significantly less. This trend was exactly predicted by the model, verifying that the axisymmetric finite element model has the ability to not only predict displacement caused by mechanical loading but also thermal loading. It is also evident in the test results that the 15° sample settled down to the FEA predicted displacement within the 5 cycles while the other two configurations seem to still be trending that way. This is contributed to the fact that the 45° and 60° samples are more subject to effects of micro-crack formation that may not have totally saturated after the 5 cycles. It is thought that as more cycles are experienced by the samples that along with the 15° samples the 45° and 60° layups displacement would be quantitatively predicted by the model.

11.3 Conclusions Drawn from Transient Temperature Tensile Testing

The cryogenic tensile testing was critical in verifying that the joint design was viable for commercial use. It also brought to light details that will make the design of such joints much easier in the future. In the cryogenic tensile testing the joints were tested until failure. It was found that the joints structural integrity remained after the thermal cycles. The mean failure load of the nine samples was 2550 N (4620 lbf). The standard deviation of the mean strength was 2313 N (520 lbf). Also many different failure modes were seen. This is a good indication that imperfections in the manufacture of the joint are driving the joint failure mode rather than weaknesses in the design. It was even seen in two of the samples that the aluminum rods being joined together began to yield before the joint failed indicating that through careful manufacture joint strength can exceed the strength of the members being joined.

One of the more significant finds of the cryogenic tensile testing was not an original goal of the experiment but has great implications. It was noticed that although the joints were initially at liquid nitrogen temperature at the beginning of the test, by the end, the joints had cooled significantly. This was due to the large temperature difference between the joint and the grips. The large mass of the grips held ample heat to quickly warm the sample. In response to this observation a temperature response curve of the center of the joint was taken and showed exactly what was expected, a transient temperature during the test. Knowing this it was expected that the force vs. displacement plots of the joints would become non linear due to the changing material property. This was not the case. The results of the transient tensile tests seemed to have changed very little when compared to the results of the room temperature tensile testing. Due to this the same material properties used in the room temperature FEA were used for the transient temperature FEA and the prediction matched the measured data. This implies that the change in material properties has an insignificant effect on the joints mechanical properties. This makes the design of joints to be used at various temperatures much simpler.

11.4 Recommendations for Future Work

The testing here has provided enough evidence that the finite element model can serve as a valuable tool for cylindrical adhesive joint design, providing a way to not only predict trends but also in obtaining quantitative results. The next step that can be taken with this research is the verification of the v and w displacements. Although these displacements are not important when designing mainly for dimensional stability in the x-direction they become important when stresses are to be verified, for use in failure prediction. Other options could be explored in the manufacturing of the joints to ensure that with a more automated process less spread between samples is indeed achieved.

In conclusion, it is hoped that the information found within will prove useful in the design and development of cylindrical adhesive joints via the finite element method.

REFERENCES

[1] Lyon, P., 2010, "Axisymmetric Finite Element Modeling for the Design and Analysis of Cylindrical Adhesive Joints Based on Dimensional Stability," M.S. thesis, Utah State University, Logan.

[2] Lambert, M., 2011, "Investigation of the Design and Static Behavior of Cylindrical Tubular Composite Adhesive Joints Utilizing the Finite Element Method and Stress-Based Failure Theories," M.S. thesis, Utah State University, Logan.

[3] Hancox N.L., 1998, "Thermal Effects on Polymer Matrix Composites: part 1. Thermal Cycling," Materials and Design, **19**, pp. 85-91.

[4] Kim, MG., Kang, SG., Kim, CG., Kong, CW. , 2007, "Tensile response of graphite/epoxy composites at low temperatures," Composite Structures, **79**, pp. 84-89.

[5] Cohen, D., Hyer, M.W., 1984, "The effects of thermal cycling on matrix cracking and stiffness changes in composite tubes," 16th National SAMPE Conference, pp. 577-588.

[6] Tompkins, S.S., Williams, S.L., 1984, "Effects of thermal cycling on mechanical properties of graphite polyimide," J. Spacecraft and Rockets, **21**, pp. 274-280.

[7] Herakovich, C.T., Hyer, M.W., 1986, "Damage-induced property changes in composites subjected to cyclic thermal loading," Eng. Fracture Mechanics, **25**, pp. 779-791.

[8] Jones, R., Lukez, R., Peterson, B., Batty, J.C., Redd, F.J., 1989, "Extended Thermal Cycle Testing of Graphite/Epoxy Composite Struts for Space Station Applications," SAMPE Quarterly, **21,** pp. 34-38.

[9] Kim, R.Y., Crasto, A.S., Schoeppner, G.A., 2000, "Dimensional stability of composites in a space thermal environment," Composite Sci. and Tech., **60**, pp. 2601-2608.

[10] Ogihara, S., Kobayashi, A., Ishiguro, T., Otani, N., 2002, "Experimental Characterization of Matrix Cracking Behavior in Thermally Cycled CFRP Laminates," Intl. J. Damage Mechanics, **11**, pp. 287-305.

[11] Kim, R.Y., and Donaldson, S.L., 2006, "Experimental and analytical studies on the damage initiation in composite laminates at cryogenic temperatures," Composite Structures, **76**, pp. 62-66.

[12] Kumagai, S., Shindo, Y., Horiguchi, K., Takeda, T., 2003, "Mechanical Characterization of CFRP Woven Laminates Between Room Temperature and 4K," JSME Intl. J., **46**, pp. 359-364.

[13] Takeda T., Takano, S., Shindo, Y., Narita, F., 2005, "Deformation and Progressive Failure Behavior of Woven-Fabric-Reinforced Glass/Epoxy Composite Laminates Under Tensile Loading at Cryogenic Temperatures," Composites Sci. and Tech., **65**, pp. 1691-1702.

[14] Shindo Y., Takano, S., Narita, F., Horiguchi, K., 2006, "Tensile and Damage Behavior of Plain Weave Glass/Epoxy Composites at Cryogenic Temperatures," Fusion Eng. and Design, **91,** pp. 2497-2483.

[15] Timmerman, J.F., Tillman, M.S., Hayes, B.S., Seferis, J.C. , 2002, "Matrix and Fiber Influences on the Cryogenic Microcracking of Carbon Fiber/Epoxy Composites," Composites: Part A, **33,** pp. 323-329.

[16] Timmerman, J.F., Hayes, B.S., Seferis, J.C., 2003, "Cryogenic Microcracking of Carbon Fiber/Epoxy Composites: Influences of Fiber-Matrix Adhesion," J.Composite Materials, **37,** pp. 1939-1950.

[17] Lee, K.H., Lee, D.G., 2008, "Smart Cure Cycles for the Adhesive Joint of Composite Structures at Cryogenic Temperatures," Composite Structures, **86,** pp. 37-44.

[18] Bartoszyk, A., Johnston, J., Kaprielian, C., Kuhn, J., Kunt, C., Rodini, B., and Young, D., 1990, "Design/Analysis of the JWST ISIM Bonded Joints for Survivability at Cryogenic Temperatures," NASA Document ID 20050214411, NASA Technical Reports Server.

[19] Cofie, E., Matzinger, L., Kuhn, J., Fan, T., 2004, "JWST ISIM Distortion Analysis Challenge," NASA Document ID 20040082141, NASA Technical Reports Server.

[20] Nemes, O., Lachuad, F., and Mojtabi, A., 2007, "Contribution to the Study of Cylindrical Adhesive Joining," Intl. J. Adhesion and Adhesives, **26,** pp. 474-480.

[21] Shi, Y.P., and Cheng, S., 1993, "Analysis of Adhesive-Bonded Cylindrical Lap Joints Subjected to Axial Load," J. Engineering Mechanics, **119,** pp. 584-602.

[22] Volkersen, O., 1938, "Rivet Strength Distribution in Tensile Stressed Rivet Joints with Constant Cross Section," Luftfehrforschung, **15**, pp. 41-47.

[23] Goland, M., Reissner, E., 1944, "The Stresses in Cemented Joints," J ApplMech Trans ASME, **66**, pp. A17-A27.

[24] Hart-Smith, L.J., 1973, "Adhesive Bonded Single Lap Joints," NASA Report Number: NAS1-CR-112236, NASA Technical Reports Server.

[25] Hart-Smith, L.J., 1974, "Analysis and Design of Advanced Composite Bonded Joints," NASA Report Number: NASA-CR-2218, NASA Technical Reports Server.

[26] Hart-Smith, L.J., 1973, "Adhesive bonded double lap joints", NASA Contract Number: NAS1-11234, NASA Technical Reports Server.

[27] Hart-Smith, L.J., 1973, "Non-Classical Adhesive-Bonded Joints in Practical Aerospace Construction," NASA Report No. CR-112238, NASA Technical Reports Server.

[28] Crocombe, A.D., Bigwood, D.A., 1989, "Elastic Analysis and Engineering Design Formulae for Bonded Joints," Intl. J. Adhesion and Adhesives, **9**, pp. 229-242.

[29] Renton, J.W., Vinson, J.R., 1975, "The Efficient Design of Adhesive Bonded Joints," J. Adhesion, **7**, pp. 175-193.

[30] Renton, J.W., 1974, "The Analysis and Design of Composite Material Bonded Joints under Static and Fatigue Loadings," PhD dissertation, University of Delaware, Newark.

[31] Cook, R., Malkus, D., Plesha, M., and Witt, R., 2002, *Concepts and Applications of Finite Element Analysis*, John Wiley & Sons Inc., Hoboken, NJ, pp 206-214.

[32] Smith, I., Griffiths, D., 1998, *Programming the Finite Element Method*, John Wiley & Sons Inc., Hoboken, NJ, pp. 90-91.

[33] Smith, I., Griffiths, D., 1998, *Programming the Finite Element Method*, John Wiley & Sons Inc., Hoboken, NJ, pp. 175, Chap. 5.

[34] Smith, I., Griffiths, D., 1998, *Programming the Finite Element Method*, John Wiley & Sons Inc., Hoboken, NJ, pp. 496, 502, 508, Appendix 5.

[35] Hyer, M.W., 1997, *Stress Analysis of Fiber-Reinforced Composite Materials*, DEStech Publications Inc., Lancaster, PA, pp. 58.

APPENDIX

FINAL MESH VISUALIZATION

Below is the mesh with the aspect ratio of the elements plotted. Care was taken to ensure during the mesh refinement stage that the aspect ratios were kept reasonable.

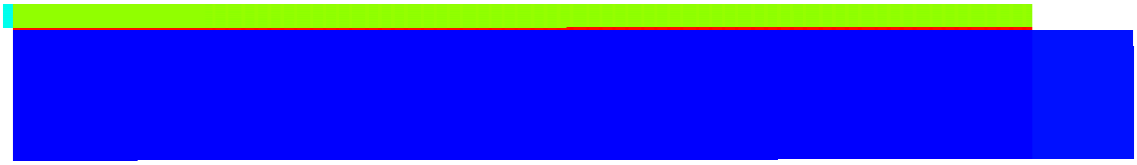

Figure 67. Element aspect ratios

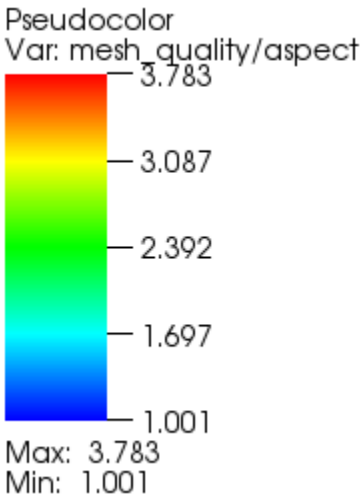

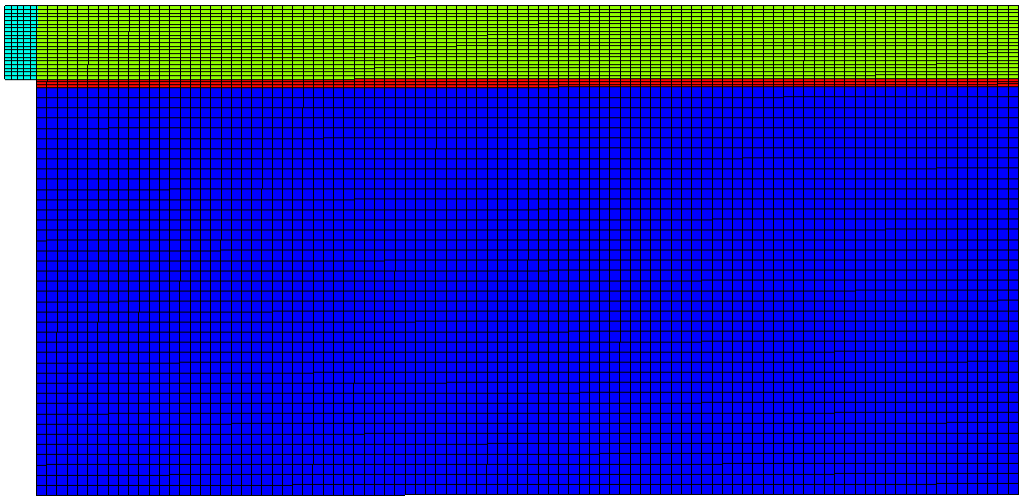

Figure 68. Element aspect ratios zoomed in to show mesh